THE EFFECT OF ANTIMONY ON SEGREGATION DURING DENDRITIC SOLIDIFICATION IN A CAST MODIFIED 4720 ALLOY

Melvin W. Coffey
B.S., Oregon State University, 1972

A thesis submitted to the faculty
of the Oregon Graduate Center
in partial fulfillment of the
requirements for the degree
Master of Science
in
Materials Science and Engineering

December 1985

The thesis "The Effect of Antimony on Segregation During Dendritic Solidification in a Cast Modified 4720 Alloy" by Melvin W. Coffey has been examined and approved by the following Examination Committee:

Jack H. Devletian
Associate Professor
Thesis Research Advisor

William E. Wood
Professor

Larry E. Murr
Professor

Jon Orloff
Associate Professor

ACKNOWLEDGEMENTS

The author wishes to express his gratitude to the following individuals, corporations and institutions who made this work possible. To Leroy Finch who encouraged me to pursue an advanced degree. To Larry Venne and Stubs Davis who made this work possible. To both Tektronix, Inc. and the Bureau of Mines for providing analytical assistance. To the faculty and students of OGC who provided direction and constructive criticism. And to Eileen Schuba for playing the role of a sounding board without sounding bored.

TABLE OF CONTENTS

LIST OF TABLES vi

LIST OF FIGURES vii

I. INTRODUCTION 1

1.0 BACKGROUND 1

1.1 FRACTURE MODE VARIABLES 2

1.2 INTERACTIVE CO-SEGREGATION 3

1.3 THE BEHAVIOR OF Sb IN ULTRA-HIGH PURITY Fe-Ni 3

1.4 INVESTIGATION OF OBJECTIVES 4

1.5 ALLOY SELECTION 5

II. EXPERIMENTAL PROCEDURE 6

2.0 ANTIMONY MONITORING 6

2.1 ALLOY PREPARATION 6

2.2 METALLOGRAPHY OF AS-CAST SAMPLES 8

2.3 HEAT TREATMENT 12

2.4 MECHANICAL TESTING 13

2.5 METALLOGRAPHY OF AS-CAST SAMPLES 14

2.6 FRACTOGRAPHY 15

III. RESULTS 17

3.0 ANTIMONY MONITORING 17

3.1 BULK OR NOMINAL COMPOSITIONAL ANALYSIS 17

3.2 METALLOGRAPHY OF AS-CAST SAMPLES 17

3.3 MICROHARDNESS 20

3.4 MICROSEGREGATION 21

3.5 MECHANICAL TESTING RESULTS OF HEAT TREATED SAMPLES .. 24

3.6 METALLOGRAPHY OF HEAT TREATED SAMPLES 26

3.7 FRACTOGRAPHY 28

IV. DISCUSSION 32

4.0 ANTIMONY MONITORING 32

4.1 AS-CAST METALLOGRAPHY 32

4.2 AS-CAST MICROHARDNESS 34

4.3 AS-CAST MICROSEGREGATIONAL ANALYSIS 35

4.4 HEAT TREATED "A" CONDITION: MECHANICAL TESTING 44

4.5 HEAT TREATED "A" CONDITION: HARDNESS TESTING 46

4.6 HEAT TREATED "A" CONDITION: METALLOGRAPHY 47

4.7 HEAT TREATED "A" CONDITION: FRACTURE/ MICROSTRUCTURE ANALYSIS 48

4.8 THE BASIC MODEL FOR SEGREGATION 50

4.9 THE ROLE OF THE SEGREGATED AS-CAST CONDITION ON THE HEAT-TREATED STRUCTURE 57

4.10 DISCUSSION OF HEAT-TREATED "B" CONDITION 59

4.11 PRE-ANALYSIS ERROR EVALUATION 62

V. CONCLUSIONS 71

VI. FURTHER WORK 73

VII. REFERENCES 74

VIII. TABLES 77

IX. FIGURES 89

X. APPENDIX I - RAW DATA AND SAMPLE CALCULATIONS 170

XI. APPENDIX II - MECHANISMS CONTROLLING CARBIDE SIZE 182

XII VITAE 186

LIST OF TABLES

TABLE I:	Target Composition for Modified 4720 Alloy	78
TABLE II:	Actual Compositions of Samples by Spectrographic Analysis	79
TABLE III:	Actual Weight % Sb by Graphite Furnace Atomic Absorption Analysis	80
TABLE IV:	Summary of Heat Treatments	81
TABLE V:	Low Alloy Sb Monitoring	82
TABLE VI:	Measured ASTM Grain Size, As-Cast Condition	83
TABLE VII:	Calculated Freezing Rate from Measured Secondary Dendrite Arm Spacing, As-Cast Condition	84
TABLE VIII:	WDX Analysis of Group I Samples for C and Sb Content in Selected Regions, As-Cast Condition ...	84
TABLE IX:	C and Sb Concentrations Found by Microprobe Analysis	84
TABLE X:	Brinell Hardness of Samples from Heat Treatment "B" .	86
TABLE XI:	Compositions of Intergranular Fracture Sites Via EDX Analysis	87
TABLE XII:	M and C Changes vs Carbide Size as a Function of Increasing Sb Content in the As-Cast Condition	88

LIST OF FIGURES

Fig. 1	Test bar configuration and macro etch sample removal	90
Fig. 2	Metallographic sample removal.....	91
Fig. 3	Sectioning test material for subsequent heat treatment and machining	92
Fig. 4	Sb concentration of AOD and non-AOD processed low alloy heats as a function of time	93
Fig. 5	As-cast macro etched sample	94
Fig. 6	As-cast macro etched sample	94
Fig. 7	As-cast macro etched sample	95
Fig. 8	As-cast macro etched sample	95
Fig. 9.	As-cast macro etched sample	96
Fig. 10	As-cast macro etched sample	96
Fig. 11	As-cast macro etched sample	97
Fig. 12	Example of as-cast microstructure	97
Fig. 13	Increasing pro-eutectoid ferrite at prior austenite grain boundaries with increasing Sb content	98
Fig. 14	Increasing pro-eutectoid ferrite at prior austenite grain boundaries with increasing Sb content	98
Fig. 15	Example of random ferrite in group IV samples .	100
Fig. 16	Example of random ferrite in group IV samples .	100
Fig. 17	Differences in ferrite staining behavior with the Vilellas reagent	101
Fig. 18	Comparison of sample etching behavior of the same region with Villelas and Steads reagent	102

Fig. 19	Comparison of sample etching behavior of the same region with Villelas and Steads reagent	102
Fig. 20	Relationship between dendrite solidification pattern and ferrite locations	103
Fig. 21	Example of stained ferrite	104
Fig. 22	Example of unstained ferrite	104
Fig. 23	Increasing ferrite/bainite interface etching characteristics with increasing Sb content	154
Fig. 24	Microhardness variations of selected micro-structural regions vs Sb content	106
Fig. 25-27	Alloy element line scans via EDX	107-108
Fig. 28-31	Cu line scan analysis of selected regions	108-110
Fig. 32	The segregation index of various elements vs Sb content	111
Fig. 33	Compositional variations of USF regions vs Sb content	112
Fig. 34	Compositional variations of SF regions vs Sb content	113
Fig. 35	WDX analysis of C in selected regions	114
Fig. 36	WDX analysis of Sb in selected regions	115
Fig. 37	CVN impact energy transition curves	116
Fig. 38	CVN impact energy values vs Z	117
Fig. 39	Heat treated "A" condition brinell hardness values vs Sb content	118
Fig. 40	Effects of various heat treatments of CVN impact properties vs Sb content	119
Fig. 41-46	Macro etched samples in the heat treated "A" condition	120-122
Fig. 47	Examples of microstructures after heat treatment "A", all groups	123

Fig. 48-49	Comparison of the microstructure and dendrite structure of group I samples in the heat treated "A" condition	124
Fig. 50-51	Comparison of the microstructure and dendrite structure of group IV samples in the heat treated "A" condition	125
Fig. 52-56	Grain boundary visibility behavior of group I and Group IV samples	126-128
Fig. 57	Alloy element line scan analysis across grain boundaries in the heat treated "A" condition ..	128
Fig. 58	Microstructure of heat treated "C" samples	129
Fig. 59	Microstructure of heat treated "C" samples	130
Fig. 60-67	Fracture behavior of group I samples vs test temperature	131-134
Fig. 68-75	Fracture behavior of group II samples vs test temperature	135-138
Fig. 76-83	Fracture behavior of group III samples vs test temperature	139-143
Fig. 84-91	Fracture behavior of group IV samples vs test temperature	144-147
Fig. 92	Increasing "Step Fracture" mode with increasing Sb content	148
Fig. 93-94	"Step Fracture" and shear lip fracture behavior of group III and IV samples	149
Fig. 95	Fracture mode vs solidification pattern	150
Fig. 96-97	Fracture vs microstructure in group I	151-152
Fig. 98-101	Fracture vs microstructure in group II	153-155
Fig. 102-106	Fracture vs microstructure in group III	156-159
Fig. 107-121	Fracture vs microstructure in group IV	160-168
Fig. 122	Terinary phase diagram of Fe-C-M+I	168
Fig. 123	Isopleth of Fe-M+I phase diagram	169

ABSTRACT

THE EFFECT OF ANTIMONY ON SEGREGATION DURING DENDRITIC SOLIDIFICATION IN A CAST MODIFIED 4720 ALLOY

Melvin W. Coffey, M.S.
Oregon Graduate Center, 1983

Supervising Professor: Jack H. Devletian

Antimony's influence on segregation during solidification, mechanical properties, fracture mode, and microstructure were investigated in this study. A single heat of a modified 4720 alloy was innoculated with varying concentrations of Sb. In the as-cast condition, metallographic analysis was performed to show microstructural variations as a function of Sb content. Microstructural differences were related to changes in microhardness, and the microsegregation of Sb, C, Cr, Mo, Ni, and Si. Equipment used to characterize microsegregation in this study include: energy dispersive X-ray analysis, wavelength dispersive X-ray analysis, and electron microprobe analysis.

Several heat treating cycles were given to selected samples in order to show the effects of Sb additions on resulting CVN transition temperature values, diffusion characteristics, microstructure and fractography. Changes in CVN transition temperature were related to fracture/microstructure variations.

The results indicate that Sb additions retard the peritectic solidification reaction. This leads to an increased segregation ratio of alloying elements, causing specific regions of the as-cast microstructure to change in alloy element concentration. Standard normalizing, quenching and tempering heat treatments were ineffective in reducing the degree of microsegregation obtained during solidification. Carbide size varied significantly depending upon its location in the dendrite structure. Fracture behavior of CVN samples was a function of carbide size. Carbide size increased in the general heat treated microstructure with increasing Sb content, changing the fracture mode from ductile dimple to a cleavage fracture mode. Intergranular fracture resulted after heat treatment in those locations which previously contained proeutechtoid ferrite in the as-cast condition. Intergranular fracture was found to be a function of both carbide size and Sb segregation. The carbide size decreased in grains exhibiting intergranular fracture. Increased concentrations of alloy and impurity elements in these regions increased the segregation ratio and hence the interactive co-segregation of Sb to grain boundaries leading to embrittlement and intergranular fracture. As a result, the addition of Sb tended to increase the CVN transition temperature after heat treatment by increasing the propensity for both cleavage and intergranular fracture. Hence Sb content should be restricted to 0.005 wt % in this alloy system.

I. INTRODUCTION

1.0 BACKGROUND

As the demands on the performance of materials has increased, so has the need for understanding the roles of impurity segregation and grain boundary behavior. Recent advances in analytical instrumentation have greatly broadened our understanding of impurity induced interfacial co-segregation of elements.[1-17]

In metallic systems, the segregation of P, S, Sn, Sb, and As to grain boundaries resulting in intergranular fracture behavior is now well established.[4-17] Such fracture behavior is frequently referred to as reversible temper embrittlement in low alloy steels, and typically decreases the impact properties while shifting the transition temperature to higher values. Most of the work investigating the roles of P, S, or Sn has been performed on wrought or forged materials.[6-14] Some work with wrought materials includes the role of Sb on intergranular fracture.[13,14] Most of the cast materials studies have investigated the behaviors of S and P [15,16,17] which are assumed to be much more ubiquitous than Sb. Consequently, little work has been performed to establish the effects of Sb in a cast material. No studies have been carried out on Sb induced embrittlement in a commercial casting using standard foundry practices. The standard procedure of many foundaries is to use scrap or recycled materials for melting stock to manufacture production castings. Thus the possibility exists for trace element

contamination to induce interfacial co-segregation of elements which can lead to premature failure.

1.1 FRACTURE MODE VARIABLES

Fracture mode is dependent upon the following variables;[38]

1) bulk or nominal composition
2) segregation (microcompositional) behavior
3) test temperature
4) loading method
   a) rate of load
   b) state of stress
5) heat treatment
6) the presence of second phases, precipates, and inclusions

In general, there are three main modes of fracture in steels;[38]

1) ductile dimple (micro-void coalescence)
2) cleavage
3) intergranular

The first two fracture modes are fairly well understood.[38] The mechanisms controlling intergranular fracture have been nebulous. Of particular interest to this study was the relationship between Sb, segregation behavior, and the occurrence of intergranular fracture in a cast low alloy system.

1.2 INTERACTIVE CO-SEGREGATION

Reversible temper embrittlement appears to be attributed to the following relationships:

1) Interactive co-segregation of alloying (m, defined as alloy elements intentionally added) and impurity (I) elements to prior austenite grain boundaries causing decohesion and intergranular fracture.[8]

2) An inverse relationship between solute solubility and segregation tendencies.[8]

3) Major M elements have pronounced effects on the solubilities of I elements.[8]

4) Reversible temper embrittlement can be attributed to the segregation of I elements in ferrite.[8]

5) Attractive interactions such as Ni-Sb at grain boundaries enhance the segregation of M and I elements.[33,41,45]

6) The scavanging of M and I elements by other alloying elements hinders segregation due to attractive interactions.[33] An example would be Mo scavanging C to form molybdenum carbides.

7) Carbon plays an important but little understood role in intragranular fracture.[33]

1.3 THE BEHAVIOR OF Sb IN ULTRA-HIGH PURITY Fe-Ni

A recent study on the behavior of Sb in an ultra-high purity Fe-Ni alloy system indicated[41] that Ni and Sb enhance each other's

segregation to α-iron grain boundaries, due to strongly attractive interactions. The regular solution model for interactive co-segregation using a McLean type equation (see section 4.8) relating the segregation free energies to impurity element concentration and grain boundary coverage, gives the best fit to currently available Auger data. Other studies[13] indicate that Sb is five times more effective than S in inducing intergranular fracture at cathodic potentials in stress corrosion testing, and that S and Sb do not compete for grain boundary sites.

1.4 INVESTIGATION OBJECTIVES

This study was designed to achieve the following objectives:

1) To determine if Sb exists in low alloy steel castings produced with purchased or recycled scrap. If Sb does exist, in what concentration levels?
2) Does the argon-oxygen-decarburization (AOD) process used by many foundries to remove impurity elements from steels, remove Sb from the melt?
3) At what concentration levels can Sb be tolerated with respect to CVN impact energy?
4) To what extent does Sb influence segregation during dendritic solidification?
5) What is the influence of Sb on the microstructure, dendrite structure, fracture behavior, and mechanical properties?

1.5 ALLOY SELECTION

This investigation used a cast modified 4720 low alloy steel with purchased scrap for melting stock and typical foundry melting, molding and pouring procedures. This alloy was chosen because it is used in moderate section size castings (less than 4" thick) such as bucket, shovel, or chain parts. These castings have moderate to high casting liability and replacement costs. Field failure studies indicated that this particular alloy is prone to intergranular fracture in the normalized, quenched, and 1125 F (607 C) tempered condition.

II. EXPERIMENTAL PROCEDURE

2.0 ANTIMONY MONITORING

Program objectives #1 and #2 were obtained in the antimony monitoring phase of the overall study. Cast test bars made with production castings for subsequent quality control (QC) mechanical testing, were selected at random over a period of time from a variety of alloy types. The selection was made to include AOD (argon-oxygen-decarburization) and non-AOD processed material. Drillings were taken from the test bars, all from the same location. The drillings were analyzed on an emission spectrograph, but the Sb concentrations were too low for accurate analysis. Therefore analysis was performed with a Perkin Elmer model #603 atomic absorption system (AA) in the graphite furnace mode. Full background corrections were applied and National Bureau of Standards (NBS) standards of similar composition were used to calibrate the instrument before the unknown samples were tested. The values obtained from Sb standardization during calibration of the AA system were: actual Sb value, 0.013 Wt %; experimental Sb value, 0.012 Wt %. It was felt that the results were acceptably accurate.

2.1 ALLOY PREPARATION

In order to achieve program objectives #3, #4, #5, test material with a constant nominal composition was prepared with varying concentrations of Sb content. Any change in the presence of second phases,

precipitates, and inclusions were assumed to be due to the influence of the Sb additions.

Test material was made from approximately 73% purchased scrap, 25% returns, and 2% alloy additions. The heat was melted in an open air arc furnace. Alloy additions were made after preliminary spectrographic chemical analysis to adjust the final composition. See Table #I for the 4720 target composition. After transfer from the furnace to a holding ladle, the melt was poured into a 200 pound capacity shank ladle where the Sb additions were made for the following groups of test bars:

Group I	No Sb additions made
Group II	0.005 Wt % Sb additions
Group III	0.010 Wt % Sb additions
Group IV	0.015 Wt % Sb additions

Four test bars were poured per group into zircon sand molds with identification stickers. The test bars were allowed to cool to room temperature, then shaken out. The final heat composition was determined by an ARL 34000 emission spectrograph, calibrated to standards of similar composition as the test material. See Table #II for actual composition.

Since Sb has limited solid solubility with iron, it was suspected that Sb concentrations might change from test bar to test bar. Therefore, the Sb content was determined for each test bar per group by AA analysis in the graphite furnace mode, with full background corrections

applied. The system was standardized to NBS samples of similar composition and Sb content. Test bars were then chosen from each group of test material for subsequent heat treatment and testing based on similarity of Sb content per test bar. See Table #III.

2.2 METALLOGRAPHY OF AS-CAST SAMPLES

The parameters that were monitored to evaluate the effects of Sb on segregation during solidification were:

1) Macro/microstructure
2) As-cast grain size
3) Cooling rate
4) Microhardness of selected regions
5) Composition of selected regions in the microstructure.

Macro etched sections of the as-cast test specimens were prepared by cutting vertical 1" slabs from one test bar group with a water cooled abrasive saw. See Figure #1. The slabs were then hand ground with successive grits of 80, 120, 240, 400, 600 silicon carbide paper, then polished by hand with successive grits of 50um, 10um, 3um, 1um diamond paste. The final polish was done by hand with 0.05um gamma alumina. The polished slabs were then etched with Vilella's reagent to reveal the macrostructure. The Vilellas' reagent consisted of:

5 ml hydrochloric acid

1 ml picric acid

100 ml methyl alcohol

Regions of interest were photographed with a Polaroid MP4 camera using 35 and 18 mm lenses. All optical and subsequent SEM photographs were taken with Polaroid type 55 4x5 P/N film.

The slabs were then repolished and etched with Steads reagent to reveal the dendrite structure. The Steads reagent consisted of:

1 gm cupric chloride

4 gm magnesium chloride

1 ml hydrochloric acid

20 ml distilled water

100 ml methyl alcohol

The etched slab was then given a very light hand polish of 0.05 gamma alumina, and the results photographed. The slabs were again repolished and etched with Aqua Regia to compare with the results from the Vilellas' and Steads reagents.

Microstructural analyses were performed on the as-cast test specimens by cutting the bottom 1" of the slab used in the macro metallographic examination with a wet 8" Buehler metallurgical saw. See Figure #2. The samples were mounted in copper phenolic powder and ground. Intermediate polishing was performed with diamond paste and the final polish with 0.05um gamma alumina.

The samples were etched with Vilellas' reagent to reveal the microstructure. Regions of interest were marked with a Leitz microhardness tester, 300gm load for 30 seconds. The same relative location on the bottom of the test bar was examined in each case for each group.

See Figure #2. This sample preparation procedure was used repeatedly throughout the experimental procedure and will be referred to as "sample preparation procedure #1."

The samples were then examined on a Bausch and Lomb research metallograph. The grain size was measured using the ASTM E 112-81, Lineal Intercept (Heyn) procedure. The regions of interest marked with the microhardness tester were then examined on an AMR 1200-B scanning electron microscope (SEM) at 25kv. The samples were then repolished with 0.05um gamma alumina to remove the effects of the etchant. The regions of interest were then analyzed in the SEM with a Kevex 5100 fully quantitative Energy Dispersive X-ray Spectrometer (EDX) system for micro-compositional and line scan analysis. The following procedures and parameters were used:

1) The system was calibrated to NBS samples of similar composition.

2) Specimen current readings from a Keithly picoamperemeter were used for standard reference. Typical range: $500\text{-}800\text{x}10^{-7}$ amps.

3) All escape peaks were removed. (If incident radiation is energetic enough to cause x-ray fluorescence in the counter, the fluorescent radiation may escape from the counter without causing any ionization, carrying with it some energy normally absorbed. In this study, an Fe fluoresced Si escape peak was generated and overlapped the Mo L_{α} peak

used for analysis. The Si escape peak was removed to analyze Mo).

4) The acquisition time was held constant at 200 seconds.

5) All K ratios were normalized to 100% and corrected for atomic number, absorption, and fluorescence (ZAF processed).

The samples were then etched with Steads reagent and given a light hand polish with 0.05um gamma alumina. Examination of the samples in this condition was performed on a Bausch and Lomb metallograph in the same regions of interest marked with the microhardness tester. Cooling rate calculations were based on measured values of the secondary dendrite arm spacings according to Flemings:[18]

$$d=b(GR)^{-n} \qquad \text{(equation 1)}$$

where d is the dendrite arm spacing

b and n are constants

G is the thermal gradient

R is the growth rate of the solid-liquid interface

Secondary dendrite arm spacings are directly dependent upon cooling rate. EDX line scan analysis (deposited preferentially by the Steads reagent) was performed in the SEM across selected regions of interest marked with the microhardness tester. Other regions of interest such as dendrite arms, interdendritic regions and other microstructural features were marked with the microhardness tester, and the samples were repolished with 0.05um gamma alumina. Microhardness surveys

were performed on all regions of interest identified in the previous microhardness step, using a 50gm load for 30 seconds. These same regions were then analyzed for composition with the EDX system in the SEM using the same procedures and parameters described previously. They were also examined for composition with either a Cambridge 250 Steroscan or a Jeol SEM equipped with WDX systems. Both systems were calibrated to standards of known compositions.

A second set of samples from groups I and IV were prepared for compositional analysis using sample preparation procedure #1 and examined with an electron microprobe after repolishing with 0.05um gamma alumina. The system was calibrated to two sets of standards of known composition.

2.3 HEAT TREATMENT

A summary of the heat treatments used in this investigation are given in Table IV.

Heat treatment "A" was given to two 3/4" thick slabs taken from the bottom of the test bars and and one sectioned lengthwise to 5/8" wide as shown in Figure #3. These pieces were then austenitized at 1800 F for 1-1/2 hours and air cooled, then machined to 5/8" x 5/8" x 8" coupons. The coupons were then heat treated at 1700 F and water quenched, tempered for 1-1/2 hours at 1125 F and water quenched. Heat treatment "B" was performed on 5/8" x 5/8" x 8" coupons. Heat treatment "C" was given to 1/2" x 1/2" x 1/4" wafers taken from CVN samples after heat treatment "A".

After heat treatment the samples were analyzed to monitor the following parameters as a function of Sb content:

1) CVN impact transition curve changes
2) Hardness
3) Macro/microstructure
4) Fracture behavior
5) Intergranular fracture site composition
6) Fracture appearance vs solidification pattern
7) Fracture appearance vs microstructure

2.4 MECHANICAL TESTING

Standard CVN impact samples were made from all samples heat treated by methods "A", "BX", and "BY" in accordance to ASTM E23-72. All notches in the impacts were oriented upward toward the riser end of the test bar. See Figure #3. CVN impact transition curves were performed on all samples in the heat treated "A" condition. Impact tests were performed in accordance to ASTM E23-72. Test temperatures were: -140F, -100F, -60F, -40F, -20F, 20F, 60F, room, 100F, 140F, 180F, 212F. The -140F to 60F test temperatures were achieved using methyl alcohol in a FTS Systems, model E impact cooler. All test temperatures above room temperature were achieved in heated water. All test temperatures were monitored with a Analogic Thermocouple Potentiometer Instrument Calibrator; Digical 2, Model AN6520-8A. Impact testing was performed on a Satec model S1-103 Impact tester. All fractured samples were immediately placed in alcohol, allowed to come to room temperature, forced air

dried and coated with a clear acrylic spray. CVN samples from heat treatments "BX" and "BY" were tested at -40F.

Brinel hardness tests were performed on CVN impact halves from all groups from both heat treatments "A" and "B" in accordance to ASTM E-10-78 under a 3000kg load with a 10mm ball.

2.5 METALLOGRAPHY OF SAMPLES AFTER HEAT TREATMENT

After heat treatment, macrometallographic samples were prepared by cutting vertical 1" thick slabs from the as-cast test bars from groups I and IV, and heat treated in accordance to heat treatment schedule "A".

Metallographic specimens were taken from CVN impact samples from the "A" heat treated condition from all groups used for CVN impact testing from the -140F, -40F, room, and 212F test temperatures. The CVN impact halves were cut again in half on a 8" water cooled metallurgical saw. The fracture half was kept for fractographic analysis and the second half was used for microstructural analysis using sample preparation procedure #1. Regions of interest from both type "A" and "C" heat treated samples were marked with a microhardness tester using a 300gm load for 30 seconds. Regions of interest from both types of samples were examined metallographically and with the SEM in accordance to steps taken in section 2.2. No metallographic or SEM analysis was performed on samples from heat treatment "BX" or "BY".

2.6 FRACTOGRAPHY

The fracture samples preserved in step 2.4 were used for fractographic analysis, after ultrasonically cleaning them in methyl ethyl ketone (MEK). Samples from each group were examined to characterize the fracture mode as a function of test temperature and Sb content. The intergranular fracture sites were analyzed for the distribution of composition in the SEM using the EDX system.

Comparison of the fracture appearance with solidification structure was performed on fracture samples from group I, tested at -40F, sectioned normal to the CVN notch. The fracture was coated with a Buehler Electropolisher using Watts nickel plating solution consisting of:

nickel sulfate	300 gm/l
nickel chloride	45 gm/l
boric acid	35 gm/l
hydrogen peroxide	5 drops/gallon
conditions:	graphite anode
	50C test temp.
	current density; 0.05 amps/cm^2
	voltage; 6-12 DC

The samples were mounted in copper phenolic powder and polished and etched with Steads reagent. The samples were examined metallographically.

The technique of relating fracture appearance to microstructure was developed by Chesnutt and Spurling.[47] Fracture samples from each group that were tested at -40F were examined. The fracture surfaces were ultrasonically cleaned in MEK, then a portion of the fracture

surface was coated with microstop. The samples were electropolished with a solution of:

glacial acetic acid	540 cc
chromium trioxide	100 gm
distilled water	28 cc

conditions:	volts	15 DC
	amps	0.16 to 0.20/cm^2

Next the samples were etched to reveal the microstructural features by using Vilellas' reagent for 25 seconds in an ultrasonic bath. The microstop was then removed by ultrasonically cleaning in separate baths of acetone and MEK. After sample preparation, the samples were examined on an SEM. The relationship between carbide size and fracture mode as a function of Sb content was analyzed. Carbide size was measured from photos taken in various regions. Etching behavior as a function of fracture mode and Sb content was also evaluated.

III. RESULTS

3.0 ANTIMONY MONITORING

Antimony was present in all test samples. The range was 0.00056 wt % to 0.0058 wt % Sb with a mean of 0.00233 wt % and a standard deviation of $\pm$ 0.0012 wt %. AOD heats contained a slightly higher Sb content than non-AOD heats as shown in Table #V. During the test interval, the Sb content for both AOD and non-AOD processed heats increased one standard deviation aboe the mean value. See Fig. #4.

3.1 BULK OR NOMINAL COMPOSITIONAL ANALYSIS

The target composition is shown in Table #I and the final heat composition in Table #II. The final Sb compositions obtained per group, and the test bars chosen per group are in Table #III.

3.2 METALLOGRAPHY OF AS-CAST SAMPLES

Examination of the macrostructure with the Vilellas' reagent revealed the chill, columnar, and equiaxed zones. No observable difference was noted between groups. See Figs. #5,6. The Steads reagent revealed a dendritic solidification pattern. These are cellular dendrites because the length of the constitutionally supercooled liquid ahead of the solid/liquid interface is much less than the diameter of one grain. Primary and secondary dendrite arms are visible at this magnification. The dendritic arm growth was normal to the chill surface (mold surface), and there was an apparent random orientation of grains

in the equiaxed zone at the center of the test bar. Dendrite arm spacing was smaller at the chill surface than in the equiaxed zone. Intersecting dendrite arm groups with the same local orientation, contacting other dendrite arm groups with the same local orientation but at different angles with respect to the first group, would define a grain boundary. The grain boundaries etched differently than the matrix in all groups. No change was seen in macro solidification behavior between groups. See Figs. #7,8,9. The acqua regia etchant produced microstructures that were similar to the results obtained using Vilellas' reagent in that the chill, columnar and equiaxed zones were revealed. See Figs. #10,11.

Examination of the microstructure with the Vilella's reagent revealed that the as-cast microstructure in all groups was bainite with pro-eutectoid ferrite at the prior austenite grain boundaries. See Fig. #12. As the Sb concentration increased, the amount of pro-eutectoid ferrite increased at the austenite grain boundaries. See Figs. #13,14. In group IV samples, the pro-eutectoid ferrite also appeared randomly within the cored regions of the dendrite arms. See Figs. #15, 16.

The ferrite occurring in different regions etched at different rates, regardless of group number. See Fig. #17. As the Sb concentration increased, the bainitic matrix would etch at different rates in specific regions. See Fig. #18. Results of grain size measurements are shown in Table #VI. No change was observed in the as-cast grain size as Sb concentration increased.

The Steads reagent revealed primary, secondary, and tertiary dendrite arms at this magnification. The freezing rate of all groups was calculated from secondary dendrite arm spacings in accordance with equation #1. See Table #III for raw data. For group I samples it was calculated at 61 F/min. No change in the freezing rate was noted as Sb concentration increased. See Table #VII. Regions of interest identified in the Steads reagent etched condition were compared to the identically same regions etched with Vilellas' reagent and the following were observed:

1) Pro-eutectoid ferrite occurred at the initial prior austenite grain boundaries when a primary or secondary dendrite arm came in contact with the grain boundaries. See Fig. #20.

2) The specific region in which bainite etched differently with the Vilellas' reagent at high Sb concentrations depended upon whether or not the bainitic matrix was inside or outside a dendritic arm region, i.e., at the first or last region to solidify. The bainitic region outside the dendrite arm region (last place to solidify) etched at a reduced rate as Sb content increased. See Figs. #18,19.

3) Inclusions such as MnS, occurred in the interdendritic regions.

4) The pro-eutectoid ferrite that etched at slightly different rates with the Vilellas' reagent, reacted differently when using the Steads reagent. In one case the pro-eutectoid ferrite would be plated with copper, and in the second case it would not. This etching effect of the ferrite is defined as stained ferrite (SF) and unstained ferrite (USF). This phenomena also occurred with the randomly occurring ferrite noted inside the dendrite arms within the prior austenite grain boundaries in group IV samples. However both types of ferrite (i.e., SF and USF) are referred to as random ferrite (RF). See Figs. #15, 16,21,22.

5) The activity of the Steads reagent at the bainite-ferrite interface increased with increasing Sb content. See Fig. #23.

3.3 MICROHARDNESS

The results of the microhardness tests performed on various regions of interest as a function of Sb content are shown in Fig. #24. In general, the last regions to solidify (defined as the interdendritic arm regions, IDA) were harder than the first regions to solidify (defined as the dendritic arm regions, DA) in all groups regardless of group number. The general bainitic matrix (DA plus IDA) was harder than any ferritic region. The USF regions were harder than the SF regions

regardless of group number. As Sb content increased, the IDA regions continuously increased in hardness, while the DA regions appeared to increase in hardness slightly, then remained constant. Simultaneously the USF regions increased in hardness while the SF regions remained constant.

3.4 MICROSEGREGATION

Examples of SEM line scan analyses with the EDX system in the Vilellas' etched condition are shown in Figs. #25,26. No deviation was found in the concentration of intentionally added elements such as Cr, Si, Ni across bainitic-ferritic interfaces, due to poor signal to noise ratios. Intentionally added elements such as Si, Cr, Ni, Mo are defined as alloying elements, excluding Fe. In the unetched condition the signal to noise ratio improved. But, no change in alloy composition was detected across bainitic-ferritic interfaces regardless of group number. See Fig. #27. In the etched condition, carbides were noted in the general bainitic regions but not in the ferritic regions. See Fig. #26.

SEM line scan analysis of Cu in the Steads etched condition indicated differences in the Cu deposition rate in various regions. A rough sinusoidal curve was obtained as Cu concentration was monitored as a function of distance across the DA and IDA regions. See Fig. #28. Cu line scans across pro-eutectoid ferrite grains indicated that the SF had high concentrations of deposited Cu while the USF regions had low

concentrations. See Figs. #29,30. Across bainite-ferrite interfaces the Cu concentration was higher on the bainitic side of the interface. Cu concentration on the bainitic side of the interface increased as Sb content increased. See Fig. 31. Carbides were not noted in the ferritic regions in this condition.

From EDX analysis in the DA and IDA regions the segregation ratio for Si, Cr, Ni, and Mo were calculated. The segregation ratio (δ) is equal to the difference in elemental concentration between the IDA and DA regions divided by the bulk or nominal concentration for that particular element. In general the alloy composition was always higher in the IDA region than in the DA region, i.e., the segregation ratio for each alloying element was always positive. In group I, the segregation ratio values for Cr, Ni, and Si were low. For Mo it was intermediate. As Sb content increased, the segregation ratio for Cr, Ni and Si increased. For Mo it increased only slightly. Sb was not found in any region of any group using EDX analysis. See Fig. #32.

As Sb content increased, the concentration of Si, Cr, Ni and Mo remained constant in the SF regions. In the USF regions Mo and Si concentration increased while Cr and Ni decreased. The composition of the RF regions appearing in the IDA regions of group IV samples was similar to the composition of the USF regions found at the grain boundaries of group IV samples. See Figs. #33,34.

WDX analysis of group I samples indicated that the C content was lower in ferritic regions (SF and USF) than in the DA regions. The IDA regions were not analyzed for C content. The C content was roughly the

same between the SF and the USF regions. The SF had a higher Sb concentration than did the USF regions, while the DA regions had roughly the same Sb content as the SF regions. See Table #VIII. In group IV samples, the C content differences between the DA and IDA regions, and between the SF and USF regions were roughly the same. Both the SF and USF regions had higher C concentrations than the general bainitic microstructure (i.e., than either the DA or IDA regions). The RF regions had the highest C content of all regions analyzed. See Fig. #35. Sb was found in the USF regions only. See Fig. #36.

The electron microprobe is an instrument dedicated to compositional analysis on a microscopic scale via a WDX spectrometer. It uses a highly evacuated column and high beam current densities. An SEM equipped with a WDX spectrometer has a smaller focal spot to improve spatial resolution in the electron image, and therefore lower beam current densities. Hence, elemental X-ray output from a sample analyzed with a microprobe is higher than an SEM equipped with a WDX spectrometer. Therefore, it is more sensitive to lower elemental concentrations.

EMA analysis of group I samples indicated the USF regions were lower in C concentration than the SF regions. With the WDX analysis performed in an SEM they were roughly equal. The C concentration was the lowest where the Sb concentration was the highest. The SF regions had roughly the same C concentration as the bainitic microstructure. The C concentration in the DA regions was higher than the IDA regions. The reverse was true for Sb content.

In group IV samples, the SF regions had a C concentration roughly equal to the C concentration found in the SF regions analyzed in group I. The C concentration in the USF regions were much higher than the concentrations of C found in USF regions analyzed in group I. The RF regions in group IV had roughly the same C concentration as the USF regions found at the grain boundaries in group IV. This confirmed the WDX analysis performed in the SEM. The Sb concentration was the highest in the ferritic locations where the C content was the lowest. The C concentration was roughly the same between the DA and the IDA regions, while the Sb concentration was the highest in the IDA region. See Table #IX for general results.

3.5 MECHANICAL TESTING RESULTS OF HEAT TREATED SAMPLES

CVN transition curve testing was performed only on samples in the standard heat treated "A" condition. See Fig. #37. The results indicated a continuous drop in upper shelf energy values as Sb content increased. There was an increase in transition temperature values between group I to group II and III. Group IV values were nearly the same as the results from group I in the transition zone. At the lower shelf energy values, group II had lower impact energy values than group I. Both groups III and IV had slightly higher values than group I. Using the curve fitting technique described by Oldfield[22] for CVN data, the test temperature is transformed into a dimensionless number, Z, where:

$$Z = \tanh \frac{T-T_o}{C} \qquad \text{(equation 2)}$$

T = test temperature

T_o = transition temperature midpoint

C = difference in test temperarature between the upper and lower shelf

The results indicated a drop in upper shelf energy values as Sb content increased. Group II CVN energy values were consistently lower than group I energy values. Group III CVN energy values were less than group I energy values until Z = 0.10. This corresponds to a test temperature of 10.96F (-11.68C). Group IV energy values were less than group I values until Z = 0.70 or equal to a test temperature of -114.25F (-81.25C). See Fig. #38. Brinell hardness results are shown in Fig. #39 and indicated that the average hardness and hardness range increased slightly as Sb content increased.

The results obtained from heat treatments "B" (modified heat treatment) on samples from groups I and IV are shown in Fig. #40. The results indicated that long term tempering (BY) of material from groups I and IV increased CVN impact energy values above the results obtained for either group in the heat treated "A" condition. Long term austenitizing (BX) on material from groups I and IV increased the CVN impact energy values above the results obtained for either group in the heat treated "A" condition. Long term austenitizing of material from

groups I and IV gave higher CVN impact energy results than long term tempering of test material from each group respectively.

Brinell hardness results from samples in the heat treated "B" condition are shown in Table #X. The results indicated that long term austenitizing (BX) of samples from groups I and IV decreased hardness values in comparison to the heat treated "A" condition for either group. Hardness values for groups I and IV were the same in the "BX" condition. Long term tempering (BY) decreased hardness values dramatically for both groups I and IV in comparison to the heat treated "A" condition results. Hardness values for both groups I and IV in the "BY" condition were the same. "BY" values for both groups were less than "BX" values.

No CVN or hardness testing was performed on any sample in the heat treated "C" condition (modified heat treatment) due to a lack of test material.

3.6 METALLOGRAPHY OF HEAT TREATED SAMPLES

Macro etching samples in the standard heat treated "A" condition indicated that while the microstructure was altered relative to the as-cast microstructure, the effects of initial solidification structure remained unchanged as shown in Figs. #41 through 46. It was noted that macro etching with aqua regia produced excellent results of the solidification pattern, similar to the Steads reagent. This was not true in the as-cast condition where aqua regia compared favorably with the results of Vilellas' reagent, revealing the microstructure. Macro

etching of samples in the heat treated "B" condition was not performed because the samples were too small to reveal the entire solidification pattern. Macro etching of samples in the heat treated "C" condition was not performed due to a lack of test material.

The microstructure of all groups in the heat treated "A" condition (standard heat treatment) consisted of tempered martensite. See Fig. #47. As Sb content increased, certain regions in the microstructure appeared to be bainite, hence heat treatment "C" was given to samples from groups I and IV to test this hypothesis. Results from heat treatment "C" to be discussed later.

In group I samples, the etching rate of Vilellas' reagent was uniform across the metallographic sample. As Sb content increased, certain regions of the microstructure etched at different rates using Vilellas' reagent. By directly comparing those regions to the same regions etched with the Steads reagent (revealing the solidification pattern), it was noted that those regions of the microstructure that etched lightly with the Vilellas' reagent corresponded to the IDA regions of the sample. The darkly etched regions corresponded to the DA regions. This behavior was confirmed on the SEM. See Figs. #48-51. Because of the high tempering temperature used in heat treatment "A", grain boundaries were difficult to locate and identify at low Sb contents. As Sb content increased, the grain boundaries became more observable and occurred in the IDA regions of the samples. See Figs. 52-55. SEM line scan analysis across the observable grain boundaries at high Sb concentrations failed to indicate any change in matrix element

concentration. SEM spot analyses on the observable grain boundaries of high Sb samples failed to indicate the presence of Sb in those locations. See Figs. #56,57.

No metallographic evaluation was performed on samples in the heat treated "B" condition (modified heat treatment). Heat treatment "B" was given to samples to compare CVN changes with heat treatment "A".

The results of heat treatment "C" (modified heat treatment) are shown in Figs. #58,59. The results indicated that there was no change in the microstructure between groups I and IV when rapidly quenched. Each sample from groups I and IV was martensitic and bainite was not found. There was no change in carbide morphology.

3.7 FRACTOGRAPHY

Fracture appearance analysis was performed in the SEM. Intergranular fracture site analyses were performed in the SEM using EDX equipment. SEM fracture analyses were performed on samples from all groups at specific test temperatures taken from CVN transition curve specimens in the heat treated "A" condition. See Figs. #60-91. The results indicated that the fracture mode was a function of the test temperature and Sb content. As the test temperature decreased at a fixed Sb concentration, the fracture mode changed from ductile dimple to quasi-cleavage to cleavage. As the Sb content increased at a fixed test temperature, the fracture mode changed from mixed ductile dimple/quasi-cleavage to cleavage/intergranular fracture modes. In general, intergranular fracturing increased with increasing Sb content. EDX analyses

of all intergranular fracture sites failed to reveal Sb. The alloying element content appeared to be higher at the intergranular fracture sites at high Sb concentrations. See Table #XI.

At low magnifications in the SEM, samples from both groups I and II (heat treated "A" condition) had a relatively planar fracture morphology even though the fracture mode became more brittle (i.e., the amount of cleavage fracture was increasing) as the test temperature decreased. See Fig. #92. The overall fracture morphology of samples from group III were much rougher than samples from groups I and II at the same test temperature. Specifically, the fracture morphology took on a "step fracture" appearance at about 20F (-6.66C) which became more pronounced as the test temperature decreased. Also, most intergranular fracture sites in these samples appeared on top of the "step fracture." See Figs. #93,94. The width of the top of the "step fracture" was roughly equal to the width of the secondary dendrite arm spacings. The overall fracture morphology of samples from group IV also exhibited the same "step fracture" morphology observed in samples from group III. As the test temperature decreased the "step fracture" morphology transformed into large steps approximately equal to the size of several dendrite arms together or the initial prior austenite grain size measured in the as-cast metallographic samples. See Figure #92.

Attempts to relate fracture morphology with solidification pattern are shown in Fig. #95. The results failed to show a relationship due to sample preparation problems, hence the technique was discontinued.

Relating fracture appearance to the microstructure of a given region proved to be a valuable technique. The results from group I are shown in Figs. #96,97. There was no observable change in the general microstructure, carbide size or etching rate between regions exhibiting ductile dimple to cleavage fracture transitions at a fixed test temperature in group I samples. The largest observable carbides were typically 0.5-2.0 um long. The results from group II samples were roughly the same as those found in group I samples at the same test temperature. However it was noted that the average carbide size appeared to increase slightly. See Figs. #98-101. The results from group III revealed a change in the etching rate between cleavage and intergranular fracture site regions based on topography and morphology. See Figs. #102-106. There was also a change in the carbide size between cleavage and intergranular fracture site regions. The intergranular fracture sites had smaller carbides than the cleavage fracture regions. The largest observable carbide size in the cleavage fracture regions was measured to be 1.0-3.0 um long.

The results from group IV are shown in Figs. #107-121. A distinct change occurred in the etching rate between cleavage and intergranular fracture regions. The intergranular fracture sites were more lightly etched than the cleavage regions. There was also a distinct change in carbide size between the cleavage and intergranular regions. The largest observable carbides in the cleavage zones were measured to be 1.0-5.0 um long while in the intergranular fracture sites they were measured to be 0.05-1.0 um long.

In general, carbide size increased in the samples as Sb content increased. Carbide size was smaller in the intergranular fracture site regions than in the cleavage fracture regions. Intergranular fracture occurred in the regions where pro-eutectoid ferrite precipitated in the as-cast condition.

IV. DISCUSSION

4.0 Sb MONITORING

Analyzing separately cast test bars manufactured with castings produced with purchased or recycled scrap steel indicated that Sb was present in all samples. The mean concentration value of Sb was below limits established by subsequent CVN transition curve data indicating Sb was causing deleterious effects on mechanical properties. Statistical analyses indicated that there was less than a 15% chance of Sb causing deleterious effects on mechanical properties in low alloy steel castings produced by recycling scrap. The results also indicated that the AOD process used by many commercial foundries to remove S and P, does not remove Sb from the melt.

4.1 AS-CAST METALLOGRAPHY

Discussing the influence of Sb on mechanical properties in the heat treated condition expedites the understanding of the effects of Sb on the steel in the as-cast condition. The effect of Sb on CVN transition curves in wrought materials is to decrease upper and lower shelf energies.[5,12] There is a corrsponding increase in transition temperature data. In this investigation there was a continuous drop in the CVN upper shelf energy values as Sb content increased. CVN baseline value is defined as the curve established without Sb added. Lower shelf values initially decreased, then increased slightly above baseline

values. There was an initial increase in transition temperature results, which then returned to baseline values. This transition curve behavior is shown in latter discussions to be a function of fracture behavior, which in turn is a function of carbide size, matrix element segregation behavior, interactive co-segregation phenomenon, and elemental diffusion phenomenon. These parameters are directly influenced by the condition of the material in the as-cast condition.

From the results Sb appears to have no effect on the freezing rate or initial prior austenite grain size in the as-cast condition. Bainite occurred in all groups of test material regardless of Sb content in the as-cast condition. A bainitic plus ferritic microstructure should be produced when comparing the calculated freezing rate to CCT curves for this particular alloy. Pro-eutectoid ferrite occurred at the prior austenite grain boundaries in all samples from all groups. The occurrence of pro-eutectoid ferrite formation increased with increasing Sb content, and occurred randomly within the DA regions in group IV samples. This may be directly attributed to the fact that Sb is a ferrite stabilizer[23] and that lower alloy content is associated with dendrite cores. The differences in etching characteristics noted between DA and IDA regions in group IV samples are best explained by the changes in the segregation ratio as Sb content increased. A detailed discussion will be reserved until the segregation ratio behavior is discussed. The etching characteristics noted between SF and USF regions is best explained by compositional or orientational differences, and will be discussed further.

4.2 AS-CAST MICROHARDNESS

The hardness values of the SF regions with increasing Sb content were constant implying that there was no change in alloy element concentration with increasing Sb content. This was confirmed during micro segregation and microstructural analysis. The increasing hardness of the USF regions with increasing Sb content implies that there is a net increase in alloy element concentration. This was confirmed during microsegregational analysis.

The increasing IDA region hardness values with increasing Sb content implies that there is: 1) A net increase in alloy element concentration and carbide forming elements in these regions. This was confirmed with segregation ratio changes in this region via EDX analysis; 2) A change in the C content in this region, which was observed to decrease via microprobe analysis. A decreasing C content in this region will increase the coarsening rate constant (K*) for diffusion controlled particle coarsening. This effect will cause carbide size to increase and therefore increase hardness values in these regions as observed. More detail will be given later during the discussion of segregation ratio changes, C behavior, and K* behavior. The DA region hardness values increased slightly, then remained constant. This can be attributed to a decrease in C content and matrix element concentration in this region. More detail will be given in the discussion of the segregation ratio and C behavior.

4.3 AS-CAST MICROSEGREGATIONAL ANALYSIS

The preceding metallographic and microhardness sections indicate changes in parameters that are influenced by alloy element (carbide formers) concentration, segregation ratio, and carbon content. These latter variables were investigated in this study and the results imply changes in the activation energy controlling carbide size. The link between the variables investigated and carbide size is the coarsening rate constant (K*). See equation #3. A detailed discussion of the mechanisms controlling carbide size are addressed in Appendix #2. In general, decreasing the carbon content in ferrite will increase K* and hence carbide size, all other variables being constant. Decreasing the diffusion coefficient will decrease K* and hence carbide size. Changes in carbide size will alter hardness values. Carbide size measurements were not made in this phase of the study. TEM analysis would need to be performed.

The segregation index (δ) is described by Flemings[18] as a parameter to describe the degree of microsegregation in a cast material after heat treatment where dendritic solidification occurs.

$$\delta_i = \frac{C_M - C_m}{C_M^o - C_m^o} \qquad \text{(equation 4)}$$

where: C_M = maximum solute concentration of element i (in the IDA regions)

C_m = minimum solute concentration of element i (in the DA regions)

C_{Mo} = maximum initial solute concentration of element i

C_m = minimum initial solute concentration of element i

δ_i = index of residual microsegregation of element i

The segregation ratio for as-cast structures used in this study was developed by J. Philibert et al.[26]

$$\delta_i = \frac{C_{IDA_i} - C_{DA}}{C_{B_i}} \qquad \text{(equation 5)}$$

where: C_{IDA_i} = concentration of element i in the IDA region

C_{DA_i} = concentration of element i in the DA region

C_{B_i} = bulk or nominal concentration of element i

They noted that: 1) The segregation ratio of various elements increased with impurity concentration; 2) The segregation ratio of C is influenced by the presence of other alloying elements. The segregation ratio may be related to the diffusion behavior of elements by:

$$\delta_i = e^{-\pi^2 \left(D_{S_i} t / l_o^2 \right)} \qquad \text{(equation 6)}$$

where: D_{S_i} = the diffusion coefficient of the solute element in the solid at the temperature of homogenization of element i

t = time

l_o = 1/2 the dendrite arm spacing

In the SF regions, no change was observed in alloy element and C content as Sb content increased. This implies no change in hardness. Microhardness data confirmed the microsegregation data. The C value obtained in this region was higher than the maximum equilibrium value of C in solid solution in ferrite (0.025 Wt %). This anomaly will be covered in later discussions. Carbides where not seen in these regions. EDX and WDX analysis confirmed that the difference between the SF and USF regions is composition. As noted previously, compositional and orientational differences might be the reason for the difference in etching characteristics noted. The C content increased in the USF regions as Sb content increased. Hardness changes can be explained by the increased hardenability of this region due to increased alloy content and by local A_e3 changes. As Sb content increased, the USF regions increased in Sb, Mo, and Si content and decreased in Ni and Cr content. An increasing local Si content will increase the local A_e3 transformation temperature, therefore increasing the volume free energy change controlling the nucleation of ferrite and the concentration gradient.[27] A decreasing Ni content will have the same local effect

as an increasing Si content.[28] An increasing local A_e3 transformation temperature implies: 1) The propensity for ferrite formation will increase as Sb content increases.[29] This was observed and is the second reason why pro-eutectoid ferrite increased at the prior austenite grain boundaries alluded to previously; 2) There will be a decrease in the solubility of C in ferrite.[30] Since the C content in this region increased, but the solubility of C in ferrite decreased with increasing Sb content, it is hypothesized that the observed changes in the C content in this local region might be due to an increased propensity for carbide formation though no carbides were observed. This hypothesis can be supported by noting:

1) As C content increased, K* and hence carbide size will decrease.
2) Decreased diffusion of C atoms by the presence of Sb will decrease K*, decreasing carbide size.
3) An increasing Si content will tend to retard growth and size.
4) Mo decreases the activity of C,[46] therefore C diffusion from this region will be retarded.
5) There is a net increase in carbide forming elements in the USF region, particularly Mo. Therefore the number of potential carbides increases. This would tend to decrease hardness values, which was observed, not by increasing carbide size, but by an increasing number of small carbides.

It is therefore proposed that the high C contents found in the USF region is not due to C in solid solution in the ferrite, but due to an increasing number of very small carbides in the ferritic matrix as Sb content increased. TEM analysis of these regions would need to be performed to confirm this hypothesis. It should be noted however, that other studies indicated that a increasing A_e3 transformation temperature increases the susceptibility of low alloy steels to temper embrittlement.[27,32] Carbide precipitation is altered by increasing impurity concentrations.[32,35,37] Increasing impurity concentrations increase hardness values.[36] The random ferrite (RF) found in the DA regions of group IV samples had the same composition and carbon values as the USF regions just discussed. Therefore carbide behavior is assumed to be the same. Hardness values were similar.

High concentrations of carbides in ferrite is typically referred to as anything else except ferrite, bainite for example. Therefore questions arise regarding: 1) Is the ferrite, ferrite at high Sb concentrations? 2) Why does it remain ferrite? The data gives the following indications that the ferrite found is pro-eutectoid ferrite:

1) The sum total of all elements (not including trace elements) present in the ferrite is much lower than the sum total of all elements present in the bainitic matrix.
2) The hardness of the ferritic regions is always less than the bianitic matrix even at high Sb concentrations.

3) The etching characteristics of the ferritic regions was not the same as the bainitic matrix etching behavior. The appearance of the ferrite at low Sb concentrations, where it was distinctly and inequivocally pro-eutectoid ferrite, didn't change as Sb content increased.

4) Viewing the ferritic regions in the Steads etched condition in the SEM indicated banding of the deposited Cu. This was interpreted to mean that banding of the M elements had occurred in the ferrite. This was not seen to the same degree in the bainitic regions.

The reason the pro-eutectoid ferrite remained ferrite at high Sb concentrations even with carbides allegedly present, is due to the high concentrations of Mo and Sb occurring there. These elements are strong ferrite stabilizers, hence the ferrite remained ferrite. The segregation ratio for all elements increased in the bainitic matrix regions as Sb content increased. This means that alloy element composition is increasing in the IDA regions. It also implies that the segregation free energy (ΔG) is also increasing. The distinct difference in composition between the DA and IDA regions is the reason why the etching characteristics were different between the two regions at high Sb concentrations. As mentioned previously, the hardness of the IDA regions increased with increasing Sb content. This behavior can now be explained by alloy element and C behavior. As alloy element (carbide formers) concentration increased in this region, the likelihood of

carbide formation and hardenability also increased. Since the C content decreased, K* increased and carbide size increased. Therefore hardness in the IDA regions increased as Sb content increased as the data indicated. The DA regions increased in hardness initially as Sb content increased, then appeared to either remain constant or increase only slightly. This behavior can be explained by noting that: 1) As Sb content increased, the C content in this region decreased. Thus K* and carbide size increased, increasing hardness values. 2) As Sb content increased, alloy element (carbide formers) concentration decreased, hence the propensity for carbide formation decreased which tends to lower potential hardness values. The net result of these two opposing effects is to initially increase hardness values as carbide size increases, then hold the hardness values nearly constant as the propensity for carbide formation decreases.

The segregation ratio behavior implies that elemental behavior is influenced by the solid solubility of each alloy element with respect to Sb. Most alloy elements (M) have limited solid solubility with Sb, except for Ni.[23] This means that matrix-impurity (M-I) interactions are strongly repulsive, M_{Ni}-I_{Sb} are attractive. This implication has been confirmed by Guttman[33] who also notes that impurity (I) elements tend to alter the solid solubility of M elements in Fe. Therefore it is the solidification behavior via M-I interactions which affect the segregation ratio which in turn affects K*, carbide size and hence hardness values in the as-cast condition.

Solidification behavior of this alloy system may be understood by analyzing the phase diagrams of the primary elements. The primary elements present in this alloy system are: Fe, C, Cr, Ni, Mo, Mn, Si. Looking at the phase diagrams of various combinations of elements will define the overall solidification behavior of the multicomponent system. Of interest are: Fe-C, Fe-Mo-C, Fe-Ni-C, and Fe-Cr-C. These phase diagrams all include a peritectic reaction with Fe-Ni-C being a pure peritectic reaction without involving any other phases.[23] These peritectic reactions will dominate the freezing behavior of the remaining alloy elements. Hence the overall freezing behavior of this alloy system will involve the peritectic reaction: $L + \alpha \rightleftarrows \beta$. The dominate parameter of the peritectic reaction is diffusion of substitutional elements. The original bulk or nominal composition of alloy elements suggests that the overall reaction may occur as a hypoperitectic reaction. This leads to the natural segregation of elements during solidification. This is evident from the data since the segregation index for alloy elements is greater than zero even at low Sb concentrations. See Fig. #32.

The effect of Sb on the solidification process can be understood by analyzing the behavior of a Fe-C phase diagram and the Fe-Ni phase diagram. The Fe-C peritectic occurs at 1495 C over a range of 0.09 to 0.53 Wt % C. The Fe-Ni peritectic occurs at 1517 C over a range of 4.0 to 5.4 Wt % Ni for example. See Fig. #122. Three binary peritectic phase diagrams joined together form a ternary phase diagram, creating a three phase field below the peritectic lines of each binary peritectic.

This is due to the tie lines joining each peritectic line of the individual binary peritectics. The resulting isopleth drawn from Fe to point "X" may look similar to Fig. #123.

The initial bulk composition is at C_o At T_1 the first solid to form is approximately of composition C_1 (depending on the location of the tie line) and the final liquid to solidify in the IDA region (C_2) is much richer in alloying and impurity content.

The Fe-C solidification process involves a well known peritectic reaction.[18] Diffusion of C is rapid and the segregation ratio is very low. Increasing the alloy element concentration retards the peritectic reaction, decreases elemental diffusion, and hence increases the segregation ratio. In this study alloy element concentration was held constant, impurity element (Sb) content was increased. The result was an increased segregation ratio. Hence Sb retards the peritectic reaction.

A summary of the alloy element changes vs carbide size as a function of increasing Sb content in the as-cast condition are shown in Table #XII. In summary it can be stated that the effect of an increasing Sb content on dendritic solidification is to retard the peritectic reaction. This in turn increases the segregation ratio, causing specific regions of the solidified product to change in composition. Differences in composition affect the carbide coarsening rate (K*) and hence carbide size. Differences in carbide size influence hardness values in various regions.

4.4 HEAT TREATED "A" CONDITION: MECHANICAL TESTING

CVN impact results coupled with fractographic analysis of the CVN impact samples indicated that both CVN transition temperature and Z data (from equation #2) can be explained by analyzing fracture behavior as a function of Sb content and test temperature. The clearest interpretation can be made from the Z vs impact energy curve. In comparison to the curve generated by group I samples, group II samples had lower impact energy values regardless of test temperature. This is due to an increased propensity for cleavage fracture behavior over the ductile dimple fracture behavior found in group I samples. This translates to decreased upper and lower shelf energy values and increased transition temperature values as Sb content increased. In comparing group III results to group I, the continuing decrease in upper shelf energy values is again due to the increased propensity for cleavage fracture. However, intergranular fracture also began to appear. Thus the overall drop in the upper shelf energy values and the increased transition temperature values can be attributed to both fracture modes contributing to the decrease in CVN impact energy. The cleavage fracture mode was predominate. The apparent increase in lower shelf energy values obtained in group III samples is due to the occurrence of the "step fracture" mode described in the results. This fracture behavior occurred at about the same test temperature as the apparent increase in CVN energy values. The "step fracture" mode implies major differences in composition (and hence carbide behavior and hardness) occurring between the DA and IDA regions. In other words, the increased segregation index of various

elements found in the as-cast condition of group III samples was insufficiently altered by the heat treatment due to lack of diffusion of alloy elements. The difference in composition between the DA and IDA regions alters carbide behavior and hardness, which in turn affects the crack behavior. The crack tends to go over or around regions where composition and hardness are higher, hence the "step fracture" mode is formed between DA and IDA regions. This fracture behavior requires more energy for the passage of the crack when compared to the planar fracture mode found in group I and II samples, hence the slight increase in CVN energy results above baseline data. The drop in upper shelf energy values of group IV samples can be attributed to the greater propensity for intergranular fracture over group III samples. The lower shelf energy values are below that obtained for group III samples, but still slightly above the results obtained for group I samples. This is due to the transformation of the "step fracture" mode to a planar fracture mode with large shear steps. The planar fracture mode is due to the high degree of equivalent brittleness between the DA and IDA regions because of increased carbide size in both regions. In areas where the degree of composition, carbide size and hardness are the greatest, define the regions where the shear step is encountered. The energy for passage of the crack through the various microstructural regions is increased slightly by the encounter of the "step fracture" regions, but is relatively constant while continuing throughout the sample until the next shear step is encountered. The result is a slight increase in the lower

shelf energy values when compared to values from group I, but a decrease in energy values when compared to data from group IV.

In general, it can be stated that increased Sb content in the test samples lowered the CVN upper shelf impact energy values. It would have resulted in a decreased lower shelf energy value and an obvious shift in transition temperature values if the fracture behavior were not complicated by the implied compositional and hardness variations between the DA and IDA regions. The general shifts in toughness values are due to the increased propensity for cleavage and intergranular fracture modes as Sb content increased. The fracture behavior suggests that differences in alloy element composition occurring in the as-cast condition are unaltered during heat treatment at high Sb concentrations, i.e., the diffusion coefficient of alloy elements decreased with increasing segregation index, hence regions of alloy element concentration remain in the heat treated condition. Therefore K* is altered and hence carbide size is changing. Differences in carbide size alter fracture behavior and hardness. The changes in shelf energy values and transition temperature values with increasing impurity (Sb) content is what many authors refer to as reversible temper embrittlement.

4.5 HEAT TREATED "A" CONDITION: HARDNESS TESTING

Brinell hardness values and the range of the values increased as Sb content increased. The hardness data obtained in this heat treated condition supports the microhardness data obtained in the as-cast condition. It suggests that carbide size increased as Sb content

increased. A detailed discussion of carbide size changes is reserved until the fracture vs microstructure section where carbide size was measured in various regions. The increased range of the hardness values suggests that the compositional differences occurring between the DA and IDA regions increased as Sb content increased. Thus the results imply that with increased Sb content, alloy element diffusion decreased with increased element segregation index during heat treatment, which in turn increased K* and hence carbide size. Carbide size changes influence fracture behavior and hardness values and hence CVN transition curve data. The overall increase in hardness data was not large, however the fact that brinell hardness testing was able to detect a change with such small amounts of Sb added is significant. Increasing hardness values with increasing impurity concentration was also obtained by Senicourt and Krahe in a low alloy system tested with 800 ppm of Sb.[36] See Appendix #1, Table #AVIII for raw data.

4.6 HEAT TREATED "A" CONDITION: METALLOGRAPHY

Macroetching samples consecutively with Vilellas' and Steads reagents indicated that while the microstructure was altered by heat treatment, the effects of initial solidification remained constant. This implies that heat treatment was ineffective in altering the differences in composition found in the as-cast condition due to the fact that the diffusion coefficient is very low for solid state diffusion over long distances.

The tempered martensitic microstructure was the expected microstructure to be obtained from the given composition and heat treatment. The etching characteristics noted between the DA and IDA regions at high Sb concentrations can be explained by the increased segregation index and decreased diffusion coefficient of alloy elements during heat treatment. The higher concentrations of alloy elements in the IDA regions at high Sb contents tend to make those regions less susceptible to acid attack from the etchant as a function of time. Since the etching time was held constant, the regions where alloy element concentration was higher would appear lighter than the regions where attack occurred normally. Hence the relationship between the light and dark areas obtained with the Vilellas' reagent and the DA/IDA regions obtained with the Steads reagent. The relationship between etching characteristics implies that the increased segregation ratio with increased Sb content was relatively unchanged after heat treatment as the fracture behavior implied. Hence K* and hardness values would tend to increase as Sb content increased. This implication was confirmed with the hardness results. Therefore to confirm the various parameter behaviors noted, carbide size behavior as a function of fracture behavior must be addressed.

4.7 HEAT TREATED "A" CONDITION: FRACTURE/MICROSTRUCTURE ANALYSIS

Carbide size in various fracture regions were measured directly from SEM micrographs. The results indicated that the carbide size increased in the general microstructure from approximately 0.5-2.0um in

group I samples to 1.0-5 in group IV samples. This increase in carbide size with increasing Sb content confirms the increase in hardness values obtained, and the change in fracture mode from group I (ductile dimple) to group IV (cleavage). The relationship between carbide size and fracture behavior to be discussed later. In group IV samples a distinct change in the etching rate was observed between the cleavage fracture sites in the matrix and the intergranular fracture sites in juxteposition. This implies a difference in composition or crystallographic orientation between the two regions, and hence a difference in K* and thus carbide size. This was confirmed by comparing carbide size differences between the two regions. The carbide size in the intergranular fracture sites was approximately 0.05-1.0um compared to 1.0-5.0um found in the matrix. The measured carbides were the largest and most observable in a given region. Smaller carbides were present in all areas observed, but were too small to accurately measure. Carbide size differences between the cleavage and intergranular fracture regions confirms the implied differences in K* and hence composition between the two regions. It also implies a difference in toughness between the two regions and a clue to intergranular fracture site behavior. Smith developed a model for growth controlled cleavage fracture incorporating carbide size into his equations.[38] His equations predict that increasing carbide size gives rise to decreasing fracture stresses. McMahon and Cohen demonstrated that large carbides promote cleavage fracture modes while fine carbides allowed a material to behave in a more ductile, hence tougher manner.[39] The role of segregated C

affecting carbide size and its subsequent effects on intergranular fracture has been suggested by other authors, but not confirmed.[33] An increase in carbide size with increasing Sb content was observed in the general matrix of low alloy steels studied by D. Senicourt and P. R. Krahe.[36] Carbide precipitation at intergranular fracture sites has been observed by other authors as Sb content increased.[32,35,37]

EDX analysis of intergranular fracture sites indicated an increase in alloy element concentration above nominal values found in the matrix. This would support carbide size and etching behavior noted between the two regions. Combined Auger and Secondary Ion Mass Spectrometry (SIMS) analysis across grain boundaries and on cleavage regions would be preferable if a sample preparation procedure could be established. One possibility would be to fracture the sample under high vacuum and remotely etch the surface. The sample could be placed in a Auger+SIMS system with a sample transfer vessel.

4.8 THE BASIC MODEL FOR SEGREGATION

Thus far, the discussion of results from the heat treated "A" condition has identified the following parameters controlling mechanical properties and microstructure: 1) As Sb content increased, the segregation ratio increased, hence various regions retained the original microsegregation after heat treatment; 2) As Sb content increased, carbide size (and hence K*) increased in the general martensitic matrix; 3) As Sb content increased, carbide size (and hence K*) decreased in the intergranular fracture site regions. The segregation index and K* are

dominated by the diffusional behavior of alloy elements, hence the diffusion coefficients of alloy elements are the primary parameters. However K* is strongly influenced by C content in a given region and the segregation index does not take into account the segregation behavior at interfaces. Therefore in order to adequately describe how the identified parameters affect material behavior, two other key parameters must be addressed: 1) interactive co-segregation of M-I elements at grain boundaries and 2) the behavior of C in the general martensitic matrix and at the intergranular fracture site regions.

Interactive co-segregation at grain boundaries plays an important role in temper embrittlement and intergranular fracture behavior. In this study, EDX analysis failed to find Sb present on intergranular fracture site surfaces or across intergranular fracture grain boundaries due to the small amount needed to cause failure. Combined Auger+SIMS analysis would be the preferred analytical technique. Current auger data has been integrated successfully into a McLean type equation that describes inter-element behavior.[11,33,40] A qualitative evaluation of the equation with respect to data obtained in this study will give a clue to grain boundary behavior.

If both alloy elements (M) and impurity elements (I) segregate independently without site competition at a grain boundary ($\emptyset$), the equilibrium value of their interfacial concentration (X_i,i=I/M) is a function of their concentration (X_i^{ϕ}) in solid solution (α) by the McLean type equation:[33,40]

$$\frac{Y_i^{\phi}}{1 - Y_i^{\phi}} = \frac{X_i^{\phi} \; X_{i\,sat}^{\phi}}{1 - \left(X_i^{\phi} \; X_i^{\phi}\right)_{sat}} = \frac{X_i^{\alpha}}{1 - X_i^{\alpha}} \exp\left(\frac{\Delta G_i}{RT}\right)$$

(equation 7)

Where: ΔG_i is the segregation free energy of element i. The segregation free energy is the effect of preferential chemical interactions between two different solutes[49] and may be traced to phase diagram behavior.[33]

Y_i^{ϕ} is the partial coverage in the interfacial sublattice available for i atoms. (The assumption is that the boundary is made up of two types of sites, or sublattices; one being completely filled by the atoms of the base element and one of the solutes, the other sublattice being only partially filled by the atoms of the second solute.[49]

$X_i^{\phi}sat$ is the maximum value of X at absolute saturation.

When site competition exists between M and I atoms with respect to the solvent (Fe), the segregation free energy (ΔG_i) become functions of the intergranular concentrations of the respective M and I elements. Assuming pairwise interactions, the previous function becomes:

$$\Delta G_i = \Delta G_i^o + \frac{B_{mi}^{\Phi}}{C^{\Phi}} Y_m^{\Phi} - \frac{B_{mi}^{\alpha}}{C^{\alpha}} X_m^{\alpha}$$

$$\Delta G_i = \Delta G_m^o + \frac{B_{mi}^{\Phi}}{a^{\Phi}} Y_I^{\Phi} - \frac{B_{mi}^{\alpha}}{a^{\alpha}} X_m^{\alpha}$$

(equation 8)

where C^{Φ} and a^{Φ} are the fractions of sites available at the interface for M and I atoms, ($a^{\Phi} + c^{\Phi} = 1$)

B_{mi}^{Φ} and B_{mi} are the preferential M-I interaction energies at the interface and matrix respectively.

ΔG_i^o and ΔG_m^o are the segregation free energies and equal to the rspective binary Fe-i alloys and are constant.

Rearranging the second equation gives:

$$\frac{a^{\Phi}}{B_{mI}^{\Phi}}\left[\Delta G_m + \frac{B_{mI}^{\alpha}}{a^{\alpha}} X_I^{\alpha} - \Delta G_m\right] = Y_i^{\Phi}$$

(equation 9)

a^{Φ}, a^{α}, and G are all constant.

Y_i^{Φ} can be positive or negative depending upon the material system, segregating elements and conditions, and will determine material behavior. For example, boron additions to platinum alloys has been shown to segregate to grain boundaries, increase grain boundary cohesion and the propensity for cleavage fracture, hence increasing ductility.[50] P segregation to grain boundaries of Monel 400 has been shown to decrease intergranular fracture by mercury and hydrogen embrittlement.[51] In this study, increased Sb concentrations decreased grain boundary cohesion and increased intergranular fracture. As the segregation index of alloy elements increased with increasing Sb content, ΔG_m increased also. This occurs in the matrix and at regions near grain boundaries, particularly near grain where Sb content is high. Since the diffusion coefficient of alloy elements decreased in the regions that were initially pro-eutectoid ferrite in the as-cast condition, M and I element concentrations are higher in those regions after heat treatment. Therefore X_I^{α} will be higher at higher Sb concentrations. As alloy equation #9 indicates, increasing ΔG_m and X_I^{α} will increase Y_I^{Φ}. In other words, as the segregation free energy of the (M) elements increased with increasing Sb content (I) in a given region, the coverage of Sb (I) atoms at the grain boundaries increased. This leads to grain boundary decohesion and intergranular fracture by increased grain boundary misorientation, dislocation density or ledge strengths.[52] It is the increase in impurity concentration at low alloy grain boundaries that leads to decohesion of the boundary causing

intergranular fracture that many authors refer to as reversible temper embrittlement.[41,42,43,44,45].

Interfacial impurity coverage can be related to the diffusion coefficient of element i and time by the following relationship:

$$Y_i^{\Phi} = 2\left(\frac{X_i^{\alpha}}{d}\right)\left(\frac{D_i t}{\pi}\right)^{1/2}$$

(equation 10)

where: X_i^{α} is the concentration of element I in solid solution

d is the interface thickness

D_i is the diffusion coefficient of element i

t is time

As mentioned previously, the carbide coarsening rate (K*) is directly proportional to diffusional behavior and inversely proportional to C content. Carbide size measurements in the heat treated condition indicated that as Sb content increased (and hence diffusional behavior decreased), the carbide size in general tempered martinsitic matrix increased while carbide size in the intergranular fracture regions decreased. Diffusional behavior alone can account for the decrease in

carbide size in the intergranular fracture regions, but not in the general matrix regions. If one takes into account the C content in the general bainitic matrix and pro-eutectoid ferrite sites before heat treatment, carbide size can be predicted in the various regions after heat treatment. For example: 1) In the pro-eutectoid ferrite regions, C content was noted to increase with increasing Sb content. This would decrease K* in the intergranular fracture regions. Reduced diffusion activity with the retarded peritectic reaction would further decrease K* and hence carbide size in the intergranular fracture regions would be expected to be very small as was found in the heat treated condition of this study. 2) In the general bainitic matrix, C content decreased while diffusional activity decreased. A decreasing C content would increase carbide size while decreasing diffusional activity would decrease carbide size. Since carbide size in this region increased, one could concluded that the C content in a given as-cast region dominates K* and hence carbide size. Therefore the diffusion coefficient of C plays a secondary role in determining K* and carbide size. In other words, as Sb content increased and the diffusional behavior of alloy elements decreased with the retarded peritectic reaction in the as-cast condition, C mobility decreased during heat treatment. Jatczak et al[53] noted that C segregation and carbide formation was a function of segregated alloy element content in banded structures. J. Philibert et al[26] noted that as the segregation index of an alloy increased, the activity coefficient of C decreases in carbide formation. In a recent

article by Qu and McMahon, Jr.[54] it was noted that alloy carbide formation was not dominated by diffusional behavior during long term tempering. The same article demonstrates that alloy carbide formation and behavior plays an important role on temper embrittlement of alloy steels.

4.9 THE ROLE OF THE SEGREGATED AS-CAST CONDITION ON THE HEAT-TREATED STRUCTURE

The effects of heat treatment can be related to the results obtained and theory in the following manner: At low Sb concentrations during austentization, the ferrite and carbides dissipate upon heating above the A_{e3} transformation temperature to form austenite. Limited diffusion of alloying elements and rapid diffusion of C takes place and new austenite grain boundaries form. Upon cooling ferrite and carbides are reformed resulting in bainite. During quenching, the process is repeated, however rapid cooling produces martensite. During tempering, C is removed from solution by precipitation of iron carbides. These carbides coalesce into larger particles. Diffusion allows an exchange of atoms between the iron carbides and alloy rich ferrite to form alloy carbides.

The preceding discussion is altered at high Sb concentrations. Because the peritectic reaction is retarded, the segregation ratio of alloy elements including C increases in the as-cast condition. Since the diffusion coefficient of alloy elements is low for solid state diffusion, standard heat treatment is ineffective in reducing the segregation index. Therefore local regions of high alloy element

concentrations still exist after heat treatment. The lower C content in the matrix at high Sb contents will increase K*, hence carbide size in the matrix increased as Sb content increased in the fully heat treated condition. This leads to increased cleavage fracture in the matrix as Sb content increased. In the initial ferritic regions where the local A_{e3} transformation temperature has increased in the as-cast condition and the C content is locally higher, K* decreases, hence carbide size is retarded. Therefore in the heat treated condition, the intergranular fracture sites have more numerous smaller carbides as the data indicated. This leads to increased toughness locally. Since alloy element content and even dislocation density is different between the prior proeutectoid ferrite sites and the matrix, etching characteristics vary between the two regions as the data indicates. Alloy element concentration has increased in some of the prior proeutectoid ferrite sites. As the A_{e3} transformation temperature is exceeded during austentizing and quenching cycles, strongly negative interactions between the local Sb and alloy elements forces the Sb to relocate at the nearest low energy sites, i.e., at the new austenite grain boundaries forming during those cycles. Hence Y_i^{Φ} (impurity concentration at the grain boundary) increases, decreasing grain boundary cohesion. Therefore a crack will tend to avoid the high toughness regions associated with smaller carbide size and take the path of least resistance, i.e, the grain boundary. Hence the propensity for intergranular fracture increases. CVN impact energy values decrease due to the increased propensity for cleavage and

intergranular fracture, hence CVN transition temperature values increase.

In summary of the effects of SB on the heat treated "A" condition in this alloy system is to: 1) Cause the material to retain differences in alloy content in various regions due to the retarded peritectic reaction and diffusion coefficients. 2) Increase the carbide size in the tempered martensitic matrix while decreasing the carbide size in the regions where proeutectoid ferrite occurred in the as-cast condition, i.e., the intergranular fracture sites. 3) Increase Sb concentrations at the new grain boundary sites where the prior proeutectoid ferrite occurred in the as-cast condition. 4) Increase the propensity for intergranular fracture in the regions where proeutectoid ferrite occurred in the as-cast condition because: A) Grain boundary decohesion occurs at a higher rate and B) A crack will tend to avoid the high toughness regions associated with the smaller carbide size and take the path of least resistance, i.e., the grain boundary. 5) Increase the propensity for cleavage and intergranular fracture and thus decrease CVN impact energy and increase the CVN transition temperature values.

4.10 DISCUSSION OF HEAT-TREATED "B" CONDITION

From the preceding summary, the parameters to be evaluated by heat treatment "B" are: 1) Alloy element concentration in various regions. 2) Carbide formation behavior. 3) Grain boundary composition. Each parameter is influenced by diffusional behavior.

Diffusional behavior during heat treatment is a function of time and temperature. Time at both austentizing and tempering temperatures were varied with heat treatment "B".

The results of heat treatment "B" indicated that at low Sb concentrations, increased time at both austentizing and tempering temperatures had only a small effect on CVN impact energy values and hardness while at high Sb concentrations, CVN impact values increased and hardness values decreased. The effect of increased time on the segregation index can be evaluated by the previously given equation:

$$\delta_i = e^{-\pi^2 \left(\frac{D_s\, t}{l_o^2}\right)}$$

From this equation D_sCr decreases from 1555.0 um^2/hr to 936 um^2/hr as δ_{Cr} increased from 0.10 to 0.25. As time is increased to 15 hr, D_sCr decreases to 93.6 um^2/hr. The effect on the segregation index in both cases becomes:

@ 1.5 hr

$$\delta_{i_{cr}} \pi = e^{-2\,\frac{(936\ m^2/hr)(1.5\ hr)}{100\mu m^2}} \rightarrow 0.25$$

@ 15 hr

$$\delta_{i_{cr}} \pi = e^{-2\,\frac{(93.6\ m^2/hr)(15\ hr)}{100\mu m^2}} \rightarrow 0.25$$

From this example it can be seen that increased time at temperature has little effect of the segregation index of Cr as Sb content is increased. The same will be true with other elements except C. Hence differences in composition will remain in various regions and the ensuing reactions previously discussed could possibly take place. Therefore diffusional behavior plays a primary role in segregation behavior during solidification but only a secondary role during heat treatment.

The relationship between the interfacial impurity coverage (Y_i^{Φ}) and time is:[33]

$$Y_i^{\Phi} = 2\left(\frac{X_i^{\alpha}}{d}\right)\left(\frac{D_i\ t}{\pi}\right)^{1/2}$$

(equation 10)

From the preceding example, D_i decreased with increasing time, X_i^{α} will remain nearly constant. Therefore from the equation it can be seen that Y_i^{Φ} and hence grain boundary decohesion will decrease with increasing time at temperature. Thus the propensity for intergranular fracture will decrease, tending to raise impact energy values as found in heat treatment "B" Hence Y_i^{Φ} plays an important role in determining mechanical properties in the heat treated condition.

The effect of time on K* can be evaluated by equation #3. Increased time at temperature will allow C to diffuse in a more normal manner even as Sb content is increased. Hence the concentration of C in

ferrite (martensite consists of carbides in ferrite) will increase with increasing time. Therefore K* will decrease, decreasing carbide size and hence hardness values as found. Decreased carbide size will increase toughness values via increased ductile dimple fracture behavior, and hence increase CVN impact energy values as found from heat treatment "B". Therefore carbide size plays an important role in segregation behavior and mechanical properties of this alloy.

In summary, it can be stated that the parameters identified controlling segregation behavior in the as-cast condition and mechanical properties in the heat treated "A" condition, appear to be confirmed by the results of heat treatment "B". It is therefore concluded that carbide size and impurity concentration at grain boundaries control mechanical properties via segregation behavior. Carbide size and impurity concentration at grain boundaries were observed to be the dominate parameters in temper embrittlement behavior due to effects of service exposure in three CrMoV steam turbine rotors studied by Qu and McMahon Jr.[54]

4.11 PRE-ANALYSIS ERROR EVALUATION

The experimental procedure was designed to evaluate: 1) The presence of Sb in scrap steel and to determine if Sb could be removed from the melt by conventional processing if it were present. 2) The effect of Sb on dendritic solidification in the as-cast condition. 3) The effect of Sb on mechanical properties in the heat treated condition.

The tests outlined in the experimental procedure for monitoring Sb in scrap steel were a simple evaluation with statistical analysis. Compositional accuracy was the main criteria. The problems encountered regarding accuracy and the solutions to those problems were covered in the experimental procedure. See Appendix #1, Table #A1 for raw data used for analysis.

The tests outlined in the experimental procedure to evaluate the effects of Sb on dendritic solidification, were designed to quantitatively and qualitatively evaluate the parameters affecting solidifcation in the as-cast condition. The changes in parameters could compared to known reactions concerning solidification theory, carbide formation/coarsening and segregation behavior so that a hypothesis could be postulated concerning the effects of Sb on solidification. Some error is inherent in this analytical approach. Anticipating and reducing errors was attempted before analysis was initiated. Discussion of anticipated errors associated with each parameter analysis will be dealt with separately.

Of particular importance to the metallographic analysis of the solidification pattern was the use of the Steads reagent. Initially developed for detecting P rich regions (Steadite) in cast irons, the process involves a chemical reaction in which Cu is first deposited on P depleted regions. Metals Progress[48] described the reagent as a method to show the segregation of P and other elements in solid solution in low alloy steels. Initial use indicated it would reveal the dendritic solidification pattern of a cast material. This was confirmed using EDX

Cu line scan analysis with the SEM. Possible differences in the ferrite staining behavior (SF and USF) from the steads reagent are: 1) Compositional differences between SF and USF. 2) Crystallographic orientational differences between the two regions and, 3) A galvanic action of the plating process on the two regions causing changes in the Cu deposition rate. Possibility #3 would be a function of possibilities #1 and #2. #1 was examined via quantitative EDX analysis and confirmed. See Appendix #1, Table #AII for raw data. No testing was performed on #2, STEM or auger analysis would need to be performed. However, other authors have indicated that crystallographic orientation influences composition.[10]

Cooling rate calulations (equation #1) were based on the work of Flemings[18] where secondary dendrite arm spacings were plotted against average cooling rates. Raw data used to generate Table #VII may be seen in Appendix #1, Table #AIII. To verify this calculation, a second method of calculating cooling rate was employed. The amount of superheat in the melt and the freezing temperature based on composition were known in this investigation. The amount of time from pouring the test bars to freezing was measured and the cooling rate was calculated. The two calculated values fell within 0.2 F/min of each other.

It was therefore felt that the method of calculating the cooling rate based on secondary dendrite arm spacings was sufficiently accurate once the experimental constants in Flemings equation (equation #1) were determined. Hence changes in the solidification process via cooling rate could be evaluated as a function of Sb content.

Microhardness values also held some degree of error. The two dimensional representation of a region of interest appearing on a flat metallographic sample may not be representative of the actual three dimensional volume of the region. To overcome this possibility, as many microhardness readings as possible were obtained concerning a specific region of interest. It was assumed that the average values would be representative of the true hardness of that region regardless of volume effects. The hardness of a region in a cast material is a function of the distance from the initial chill (mold) surface, becoming softer toward the interior (last region to solidify). The experimental procedure defined the exact distance from the chill surface in which microhardness analysis could be performed. See Fig. #2. This distance was held constant from specimen to specimen to reduce error. However, not all specific regions of interest occurred within the defined distance, necessitating some specimen movement to find the region of interest. This introduced some error into the microhardness values and resulted in an increased range of results.

Carbide size and the number of carbides will alter the hardness values obtained in specific regions.[19,20] Carbide size is a function of the activation energy of coarsening equal to the diffusion of solute atoms in the microstructural matrix.[21] The number of carbides is a function of nucleation kinetics. Thus carbide size is dependent upon composition and diffusional behavior of a region. The composition of specific regions changed as Sb content increased, altering carbide behavior and therefore hardness values. By taking as many microhardness

readings as possible, the mean value should be representative of the hardness behavior of that region, the range would indicate the error introduced by distance effects. By plotting the mean hardness values of a specific region of interest vs Sb content, the effect of Sb on the hardness values could be determined. General hardness trends would indicate compositional behavior in that region as a function of Sb content. The mechanisms controlling microstructural changes could be deduced when the hardness data was compared to compositional data. Therefore the error introduced by the inability to maintain a constant position on the sample during analysis could be ignored if the general trend of the mean values of the hardness data could be supported by the general trends of the mean values of the compositional data. See Appendix #1, Table #AIV for raw data, and equation #3.

EDX microsegregational analysis also held some degree of error. For example, as an electron beam from a SEM strikes a specific region of interest, the excited volume might include areas outside the region of interest. Thus the X-ray intensity output of the various elements present might not be representative of the true composition. To reduce this possibility, the EDX analysis was performed at 20,000X, reducing the excited volume. The center of several sites per region were averaged with the results of other regions. Thus the mean compositional values should be representative of the true composition of a region. The composition and segregation ratio of a specific region of interest will change as a function of distance from the initial mold (chill) surface toward the center of the casting.[18] To overcome this problem,

the distance from the mold surface was held constant. This insured that the compositional analysis of a specific region of interest would be constant with respect to the dendritic solidification process. If compositional changes could be detected, it would be due to the effect on Sb on the solidification process, not due to distance effects. See Appendix #1, Table #A V for raw data. By plotting compositional mean value trends in various regions vs Sb content, the effect of Sb on the solidification process could be evaluated when the data was compared to hardness data.

Quantitative EDX analysis of regions in the Vilellas' etched condition gave inconsistent results. This was due to preferential removal of some elements by the etchant. Hence this technique was discontinued. EDX line scan analysis for matrix elements in the unetched condition was unable to confirm changes in composition across defined distances. This was assumed to be due to: 1) The concentration of matrix elements was too low for adequate detector response and 2) The concentration changes were too small to be within the ratemeter amplifier response limits as a function of time. Therefore EDX spot analysis was used and the time of analysis per location was increased to 200 seconds. With this technique, the counting statistics improved enough to give consistent quantitative results on standards. EDX analysis gives no clue to what form the element is in. For example, the value for Cr could be from the amount of Cr in solid solution in the matrix or from Cr as Cr carbides or both.

The same errors affecting EDX analysis also affect WDX analysis. Therefore similar analytical techniques were used in both analyses. However, other precautions had to be taken for the analysis of C. Hydrocarbon contamination from the SEM evacuation system were of primary concern. The systems were calibrated to C standards. Analysis time on C standards and regions of interest were held constant. A turbomolecular evacuation system was favored over a diffusionally pumped system. C and Sb concentration are within the limits of WDX resolution. Results can be interpreted as trends, not quantitative fact. However, it was from WDX analysis that the C content was noted to be higher in the ferritic regions than the bainitic matrix. Therefore the analysis of C and Sb was repeated for group I and IV samples using microprobe analysis to confirm the results.

The various possibilities for error present with EDX and WDX analysis on a SEM are also conceivable during microprobe analysis. The countermeasures taken to avoid error in the previous analysis were repeated here also. In addition, the following measures were also taken: 1) Two separate sets of standards of known C and Sb content were analyzed before and after the unknown analysis. 2) Five separate analyses per site per region were made for each element. This improved count statistics and helped eliminate obvious errors. 3) A linear relationship was established concerning background and hydrocarbon contamination errors during analysis. Thus such effects could be eliminated from the unknown analysis.

The tests outlined in the experimental procedure to evaluate the effects of Sb on mechanical properties, were designed to evaluate the parameters affecting fracture behavior in the heat treated condition. Bulk composition, test temperature, loading method, and heat treatment were held constant while segregation behavior was varied via Sb content. Segregation behavior will affect fracture behavior which will in turn define mechanical properties. The changes in monitored parameters could be compared to known reactions concerning carbide formation, grain boundary segregation and elemental diffusion, so that a second hypothesis could be postulated concerning the effects of Sb on mechanical properties. If the parameters identified in the first hypothesis regarding the effects of Sb on solidification were the same parameters identified in the second hypothesis regarding the effects of Sb on fracture behavior, then both hypotheses could be tested by altering one variable affecting the common parameters. The variable chosen was heat treatment (heat treatment "B"). If the results could be substantiated by comparing the identified parameter behavior to known theory, then a conclusion could be drawn regarding the effects of Sb on both solidification and mechanical properties. Anticipating and reducing errors was attempted before analysis was initiated. CVN impact testing was identified as the most probable source of errors.

To ensure accurate CVN impact energy results, the CVN impact testing machine was calibrated to Watertown Arsenal QC standard impacts. Both calibrated thermometer and external analogic thermocouple potentiometer were used when the impact cooler's range was exceeded.

One possible source of scatter and error in CVN data could be due to notch orientation of the samples. Notch orientation was held constant during machining for all samples from all groups. See Fig. #III. However, subsequent macro etching of a vertical slice from test bars indicated that the dendritic arm growth direction was perpendicular to the initial chill (mold) surface. Therefore notch orientation changed with respect to the dendrite arm growth direction. Since it was assumed that increasing Sb content would influence segregation behavior and therefore dendrite arm behavior, CVN impact data was assumed to contain some inherent error. This error would be a function of test temperature, making impact energy transition curves prone to error. Therefore the CVN curve fitting techniques of Oldfield[22] were applied to the data. This technique eliminates the temperature variable and transforms the data of impact energy vs test temperature into a linear curve of impact energy vs Z. Hence obvious errors and data scatter caused by notch orientation effects could be eliminated and the general trends analyzed. See Appendix #I, Table #A VI for raw data, and equation #2.

V. CONCLUSIONS

A single heat of cast modified 4720 steel alloy was produced with varying concentrations of Sb. Test samples were evaluated in the as-cast and heat treated condition for microstructure, microsegregation, hardness, fracture behavior, and transition temperature as a function of Sb content. The following was concluded.

1) Sb was found to be present in all low alloy steel castings produced with recycled scrap steel, but the chance of receiving scrap with Sb concentrations deleterious to mechanical properties is only 15%. The AOD process does not remove Sb from the melt. Sb concentrations should not exceed 0.005 wt % or brittle fracture will initiate in CVN specimens.

2) The deleterious effects of Sb on mechanical properties appears to be shaped during solidification by the retardation of the peritectic reaction. An increasing Sb content increases the segregation ratio of alloying elements in the as-cast condition, causing specific regions of the as-cast microstructure to change in alloy element concentrations. Standard normalizing, quenching and tempering heat treatments are ineffective in reducing the microsegregation obtained during solidification.

3) Differences in alloy and impurity element concentrations in specific regions of the as-cast microstructure alter the coarsening rate constant controlling carbide size during tempering. As Sb

content increases, the carbide size increases in the general heat treated microstructure, increasing hardness values and the propensity for cleavage fracture. Where alloy concentrations are high, Sb concentration at the grain boundaries increases leading to intergranular fracture and a decrease in carbide size.

4) It is the increasing propensity of both cleavage and intergranular fracture modes as Sb content increases, that leads to decreased CVN energy values and a corresponding increase in transition temperature.

VI. FURTHER WORK

From this particular study, there appears to be a need to investigate the following areas of research.

1) Possible phase changes in proeutectoid ferrite occurring at prior austenite grain boundaries as Sb content increases. This could be performed with differential thermal analysis.
2) Alleged carbide precipitation behavior in proeutectoid ferrite as Sb content increases. This could be performed with an analytical STEM.
3) Crystallographic orientation vs composition in proeutectoid ferrite in the as-cast condition. This could be performed via an analytical STEM or possibly Auger with LEED.
4) Thermocouple analysis of cooling rate changes vs Sb content to measure temperature gradient to growth rate (G/R) ratios.
5) Carbide behavior in the dendrite arm and interdendritic arm region vs Sb content. This could be performed via STEM analysis.
6) The composition of intergranular fracture sites as Sb content increases. This could be performed with Auger+SIMS analysis.
7) Carbide behavior in intergranular fracture site regions. This could be performed with Auger+SIMS analyses if a sample preparation procedure could be developed.

VII. REFERENCES

1) T. G. Nieh and W.D. Nix: Metall. Trans. A 1981, vol. 12A, p893.

2) A. Joshi, C.R. Shastry and M. Levy: Metall. Trans. A 1981, vol. 12A, p1081.

3) Chantal Loier and Jean-Yues Boos: Metall. Trans. A 1981, vol. 12A, p1223.

4) I.C.I. Okafor, O.N. Carlson, and D.M. Martin: Metall. Trans. A 1982, vol. 13A, p1713.

5) S.A. Herres and A.R. Elsea: Metals Transactions 1949, vol. 185, p366.

6) Wolfgang Losch: Acta Metall. 1979, vol. 27, p567.

7) T. Ando and G. Krauss: Metall. Trans. A 1981, vol. 12A, p1283.

8) J.Q. Clayton and J.F. Knott: Metal Science 1982, vol. 16, p145.

9) R.G. Thompson, C.L. White, J.J. Wert and D.S. Easton: Metall. Trans. A 1981, vol. 12A, p1339.

10) Yong-Xin Zhou, Shin-Cheng Fu and C.J. McMahon, Jr.: Metall. Trans. A 1981, p959.

11) M. Schmerling, D. Finello and H.L. Marcus: Acta Metall. 1980, vol. 14, p1135.

12) S. Takayama, T. Ogura, Shin-Cheng Fu and C.J. McMahon, Jr: Metall. Trans. A 1980, vol. 11A, p1513.

13) R.H. Jones, S.M. Bruemmer, M.T. Thomas and D.R. Baer: Metall. Trans. A 1982, vol. 13A, p241.

14) A. Joshi: Scripta Metall. 1975, vol. 9, p151.

15) E.G. Fuchs and A. Roosz: Metal Science 1975, vol. 9, p111.

16) T. Ogura, C.J. McMahon Jr., H.C. Feng and V. Vitek: Acta Metall. 1978, vol. 16, p1317.

17) E.S. Breznyak, G. Das, M.T. Groves and J.F. Wallace: Research Report #71 1968, project #61.

18) M.C. Flemings: McGraw-Hill 1974.

19) A.R. Bailey and Betchworth: Metall. Services 1967.

20) Honeycombe and Pickering: Metall. Trans. A 1972, vol. 3, p1099.

21) P. Deb and M.C. Chaturvedi: Journal of Metallography 1982, vol. 15, #4, p341.

22) W. Oldfield: Journal of Testing and Evaluation 1979, p326.

23) ASM: 1973, Vol. 8.

24) C.Y. Li, J.M. Blakely, and A.H. Feingold: Acta Metall. 1966, 14:1397.

25) G.A. Bruggman: Metall. Trans. 1975, vol. 6A, #4, p755.

26) J. Phillbert, E. Weinryb, and M. Ancy: Acta Metall. 1965, p203.

27) Honeycombe and Pickering: Metall. Trans. A 1972, vol. 3, p1099.

28) Ibid., p1106.

29) Ibid., p1106.

30) Ibid., p1108.

31) Ibid., p1108.

32) D.A. Woodford and R.W. Stepien: Metall. Trans. A 1980, vol. 11A, p1951.

33) M. Guttmann, Dumoalin, and M. Wayman: Metall. Trans. A 1982, vol. 13A, p1693.

34) F.N. Rhines: 1956, McGraw Hill.

35) M.K. Miller, P.A. Beaven, and G.P.W. Smith: Metall. Trans. A 1981, vol. 12A, p1197.

36) D. Semicourt and P.R. Krahe: The Influence of Sb on the High Temperature Tempering of Low Carbon Martensites Containing Mn, p808.

37) A. Wirth and B. Clark: Metals Technology 1981, p161.

38) J.F. Knott: Halsted Press, 1973.

39) C.J. McMahon Jr. and M. Cohen: Acta Metall. 1965, vol. 13.

40) E.D. Hondros and M.P. Seah: International Metals Reviews 1977, pg285.

41) P. Gas, M. Guttman and J. Bernardini: Acta Metall. 1982, vol. 30, p1309.

42) G. Mayer and C.A. Clark: The Metallurgist and Materials Technologist, 1974 pg491.

43) C.J. McMahon Jr. and V. Vitek: Acta Metall. 1979 , vol. 27, pg507.

44) C.J. McMahon, Jr.: Materials Science and Engineering, 1976, p233.

45) M. Guttman: Metals Science, 1976, p337.

46) S. Maslenkov: Dendritic Segregation of Mo in Steels and Ni-Base Alloys.

47) J.C. Chenutt and R.A. Spurling: Metall. Trans. A 1977, vol. 8A, p216.

48) Metal Progress: Sect. 8, Testing and Inspection, June 1981.

49) D.F. Stein and L.A. Heldt: ASM: Interfacial Segregation 1977, p266.

50) C.L. White, J.R. Keiser and D.N. Braski: Metall. Trans. 1981, vol. 12A, p1485.

51) A.W. Funkenbush, L.A. Heldt and D.F. Stein: Metall. Trans. A 1983, vol. 13A, 1983, p611.

52) L.E. Murr: Addison-Wesley Publishing Co., 1975, p309-340.

53) C.F. Jatczak, D.J. Giiradi and E.S. Rowland: Abstract from the 37th Annual Convention of ASM, 1955, pg.279.

SECTION VIII

TABLES

TABLE #I
TARGET COMPOSITION FOR MODIFIED 4720 ALLOY

Element	Target Composition (wt %)
C	0.20
Mn	1.00
Si	0.50
Cr	1.00
Ni	0.90
Mo	0.35

TABLE #II

ACTUAL CHEMICAL COMPOSITIONS OF SAMPLES BY SPECTROGRAPHIC ANALYSIS
(Values in wt %)

C	0.213
Mn	0.800
Si	0.492
Cr	0.956
Ni	0.923
Mo	0.333
Cu	0.183
S	0.015
P	0.022
Al	0.040
Ti	?<0.001
Zr	0.011
Co	0.015
Cb	?<0.001
V	0.008
W	0.011
B	0.0004
Pb	?<0.001
Sn	0.009

TABLE #III

ACTUAL WEIGHT % Sb

BY GRAPHITE FURNACE ATOMIC ABSORPTION ANALYSIS

1)	Group I		
	Test Bar	A	0.0020
		B	0.0028 *
		C	0.0030 *
		D	0.0037 *
2)	Group II		
	Test Bar	A	0.0050
		B	0.0059 *
		C	0.0065 *
		D	0.0062 *
3)	Group III		
	Test Bar	A	0.0120 *
		B	0.0120 *
		C	0.0130 *
		D	0.0130
4)	Group IV		
	Test Bar	A	0.016 *
		B	0.018
		C	0.016 *
		D	0.016 *
5)	Group V	Discarded	
		Values from 0.010 to 0.0088	

* = test bars chosen for subsequent heat treatment and testing.

TABLE #IV

SUMMARY OF HEAT TREATMENTS

	Group Number			
Heat Treatment	I	II	III	IV
A 1 1/2 hr 1800F AC 1 1/2 hr 1700F WQ 1 1/2 hr 1125F WQ	X	X	X	X
BX 15 hr 1800 F AC 1 1/2 hr 1700F WQ 1 1/2 hr 1125F WQ	X			X
BY 1 1/2 hr 1800F AC 1 1/2 hr 1700F WQ 15 hr 1125F WQ	X			X
C 1 1/2 hr 1800F AC 1 1/2 hr 1700F WQ 1 1/2 hr 1125F WQ 1 hr 1700F WQ	X			X

TABLE #V

LOW ALLOY Sb MONITORING

AA Analysis of Low Alloy Samples for Sb Content

Heat Number	Process	Wt % Sb
1	AOD	0.0022
2	AOD	0.0016
3	NON-AOD	0.0022
4	NON-AOD	0.00056
5	AOD	0.0016
6	AOD	0.0016
7	NON-AOD	0.0015
8	NON-AOD	0.0014
9	NON-AOD	0.0014
10	NON-AOD	0.0034
11	AOD	0.001
12	AOD	0.0025
13	AOD	0.0023
14	NON-AOD	0.0018
15	NON-AOD	0.0019
16	NON-AOD	0.0023
17	AOD	0.0017
18	AOD	0.0021
19	AOD	0.0031
20	AOD	0.0058
21	AOD	0.0037
22	NON-AOD	0.0046
23	NON-AOD	0.0034

Range: 0.00056-0.0058 Wt %

Mean: 0.00233 Wt %

Std Dev: $\pm$ 0.00120

AOD 0.00363 $\pm$ 0.00409

Non-AOD 0.00222 $\pm$ 0.00115

TABLE #VI

MEASURED ASTM GRAIN SIZE
AS CAST CONDITION

Group Number	Calculated Grain Size
I	M 7.0
II	M 8.0
III	M 8.0
IV	M 7.5

TABLE #VII

CALCULATED FREEZING RATE FROM
MEASURED SECONDARY DENDRITE ARM SPACING
AS-CAST CONDITION

Group Number	*Freezing Rate (of/Min)
I	61
II	61
III	61
IV	61

*This represents an arm spacing of 200 μm.

TABLE #VIII

WDX ANALYSIS OF GROUP I SAMPLES
for C AND Sb CONTENT
IN SELECTED REGIONS
AS-CAST CONDITION

Region of Interest	C Content in Wt %	Sb Content in Wt %
Stained Ferrite (SF)	0.290	0.0061
Un-Stained Ferrite (USF)	0.280	0.0045
Dendrite Arm (DA)	0.360	0.0061

TABLE IX

C AND Sb CONCENTRATIONS FOUND BY MICROPROBE ANALYSIS
(all values in wt %)
As-Cast Condition

A. Group I

Region	C	Sb
Stained ferrite (SF)	0.287 ± 0.046	0
Unstained ferrite (USF)	0.074 ± 0.007	$0.0013 \pm 3.6 \times 10^{-6}$
Dendrite Arm Region (DA)	0.333 ± 0.0442	$0.0048 \pm 8.8 \times 10^{-5}$
Interdendritic Arm Region (IDA)	0.226 ± 0.012	$0.0083 \pm 1.6 \times 10^{-4}$

B. Group IV

Region	C	Sb
Stained ferrite (SF)	0.368 ± 0.0982	$0.0018 \pm 1.83 \times 10^{-5}$
Unstained ferrite (USF)	0.230 ± 0.046	$0.0195 \pm 1.08 \times 10^{-3}$
Random ferrite (RF)	0.262 ± 0.044	$0.0211 \pm 1.18 \times 10^{-3}$
Dendrite Arm Region (DA)	0.174 ± 0.035	$0.0063 \pm 1.67 \times 10^{-4}$
Interdendritic Arm Region (IDA)	0.183 ± 0.021	$0.0264 \pm 3.26 \times 10^{-3}$

TABLE #X

BRINELL HARDNESS OF SAMPLES FROM
HEAT TREATMENT "B"

Group I		Group IV	
X	Y	X	Y
255	229	262	235
255	229	269	235
262	248	269	235
262	241	269	241
255	235	248	235
255	241	248	235
255	235	255	241
255	235	262	241
262	235	248	
262	235	248	
255	241		
262			
Mean 257.9	236.7	257.8	237.25
S.D. 3.60	5.62	9.44	3.10

TABLE #XI

COMPOSITIONS OF INTERGRANULAR FRACTURE SITES VIA EDX ANALYSIS

Group Number	Element	Values in Wt %								Mean	Std Deviation
I	Si	2.90	----	----	1.62	2.95				2.49	± 0.753
	Cr	0.98	0.92	0.89	1.07	1.21				1.014	± 0.129
	Ni	0.95	0.84	0.85	----	0.85				0.872	± 0.051
	Mo	1.42	1.37	1.30	0.84	0.35				1.056	± 0.457
Group Number	Element	Values in Wt %								Mean	Std Deviation
II	Si	0.64	1.10	0.82	2.12	1.13	2.68	1.93	1.65	1.50	+ 0.705
	Cr	1.45	1.45	1.40	1.10	1.21	1.28	0.91	1.30	1.262	0.186
	Ni	0.93	0.93	1.21	1.06	1.08	1.16	0.92	1.08	1.046	+ 0.110
	Mo	0.27	0.38	0.39	1.14	0.33	1.28	0.62	0.80	0.651	+ 0.386
Group Number	Element	Values in Wt %								Mean	Std Deviation
III	Si	1.24	1.87	0.89	1.88	2.58	2.45	2.53	1.52	1.87	+ 0.627
	Cr	1.36	1.13	1.51	1.13	1.00	1.09	1.39	1.11	1.215	+ 0.179
	Ni	0.86	1.09	----	0.97	0.86	1.01	1.13	0.88	0.972	+ 0.111
	Mo	0.70	0.92	----	0.78	1.23	1.16	1.40	0.48	0.952	+ 0.326
Group Number	Element	Values in Wt %								Mean	Std. Number
IV	Si	1.85	1.01	1.60	1.35	2.38				1.63	+ 0.518
	Cr	1.35	1.55	1.29	0.94	1.27				1.28	+ 0.220
	Ni	1.14	0.88	1.10	0.74	1.10				0.99	+ 0.177
	Mo	1.39	2.08	0.59	0.40	----				1.115	+ 0.773

TABLE #X11

M AND C CHANGES VS CARBIDE SIZE AS A FUNCTION OF INCREASING Sb CONTENT IN THE AS-CAST CONDITION

Region	M & C Changes	K* Changes	Carbide Size Changes	Remarks
S.F.	Constant	Constant	Constant	1) Hardness constant 2) Ferrite softer than bainitic matrix, therefore softer than D.A. + I.D.A. regions.
U.S.F.	C M *			1) Increased hardenability 2) Possible hardness increase due to an increasing number of small carbides, due to an increasing A_{e3} trans. temp.
R.F.	---	---		The composition and hardness of the R.F. was the the same as the U.S.F. regions at high Sb content. Therefore, the same conditions are assumed to exist.
I.D.A.	C M			The hardness increased due to increased carbide size and an increasing propensity for carbide formation due to increased matrix element contents, hence hardenability.
D.A.	C			1) Initial hardness increase due to increase in carbide size. 2) Subsequent hardness values due to the interplay of C and M. 3) Softer than I.D.A. regions because of less M elements, thus less carbide forming potential.

* Sb, Mo, Ni increased - Ni, Cr decreased.

SECTION IX

FIGURES

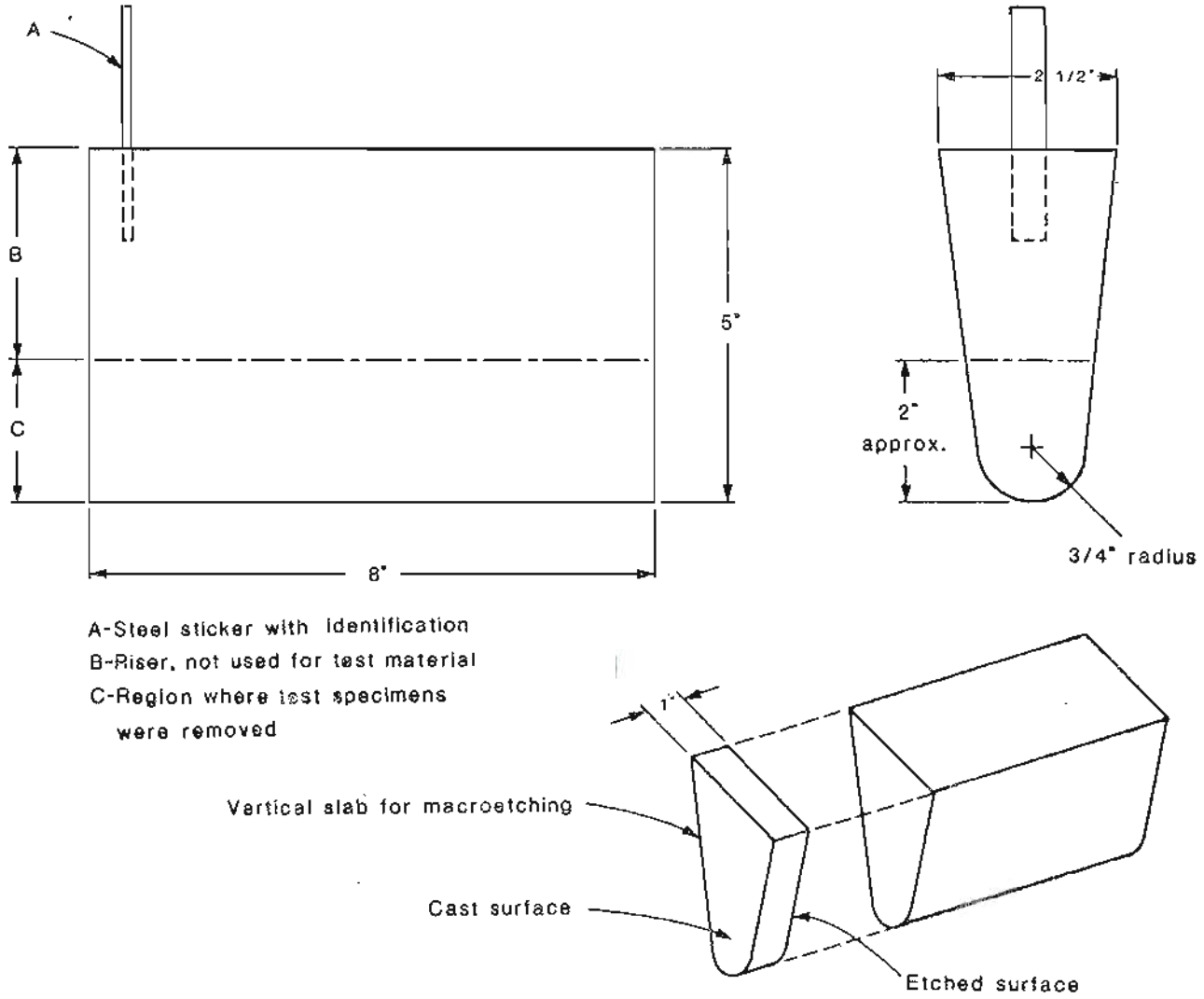

A-Steel sticker with identification
B-Riser, not used for test material
C-Region where test specimens
were removed

FIGURE #1 Test bar configuration and macro etch sample removal

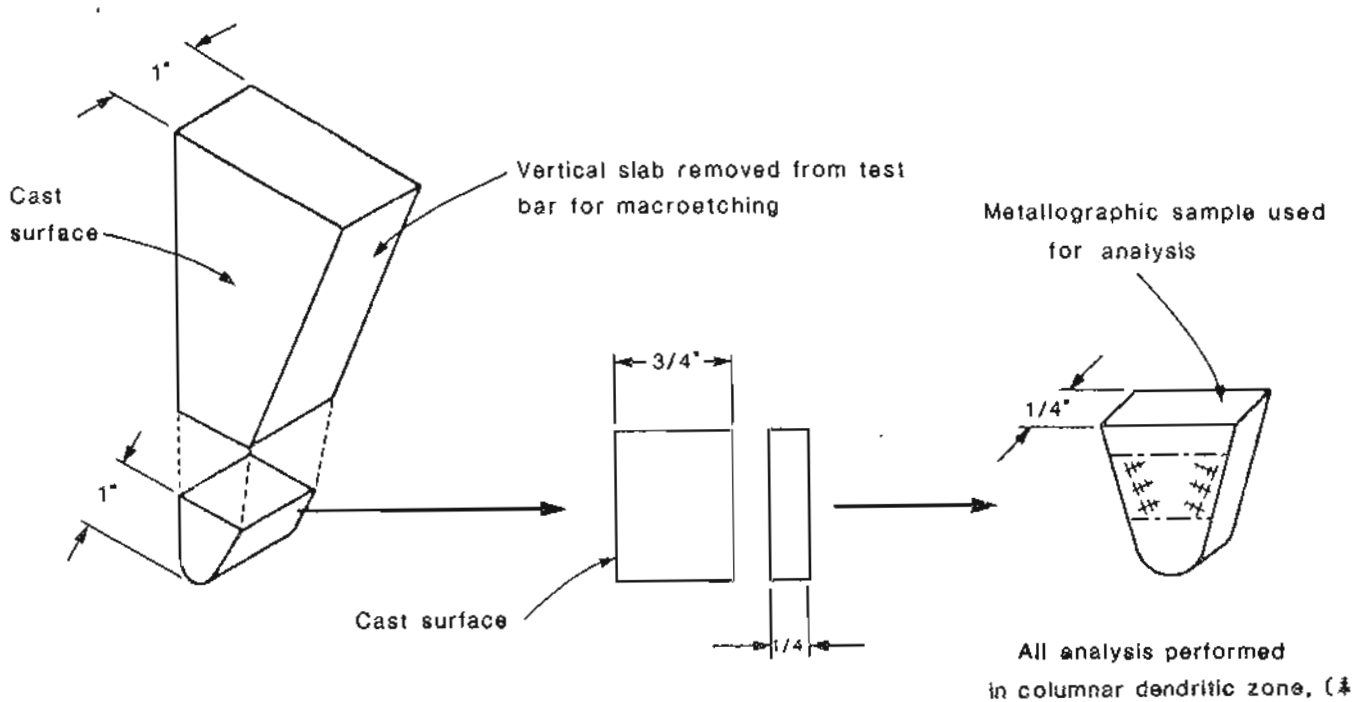

FIGURE #2 Metallographic sample removal from vertical slab taken from test bar

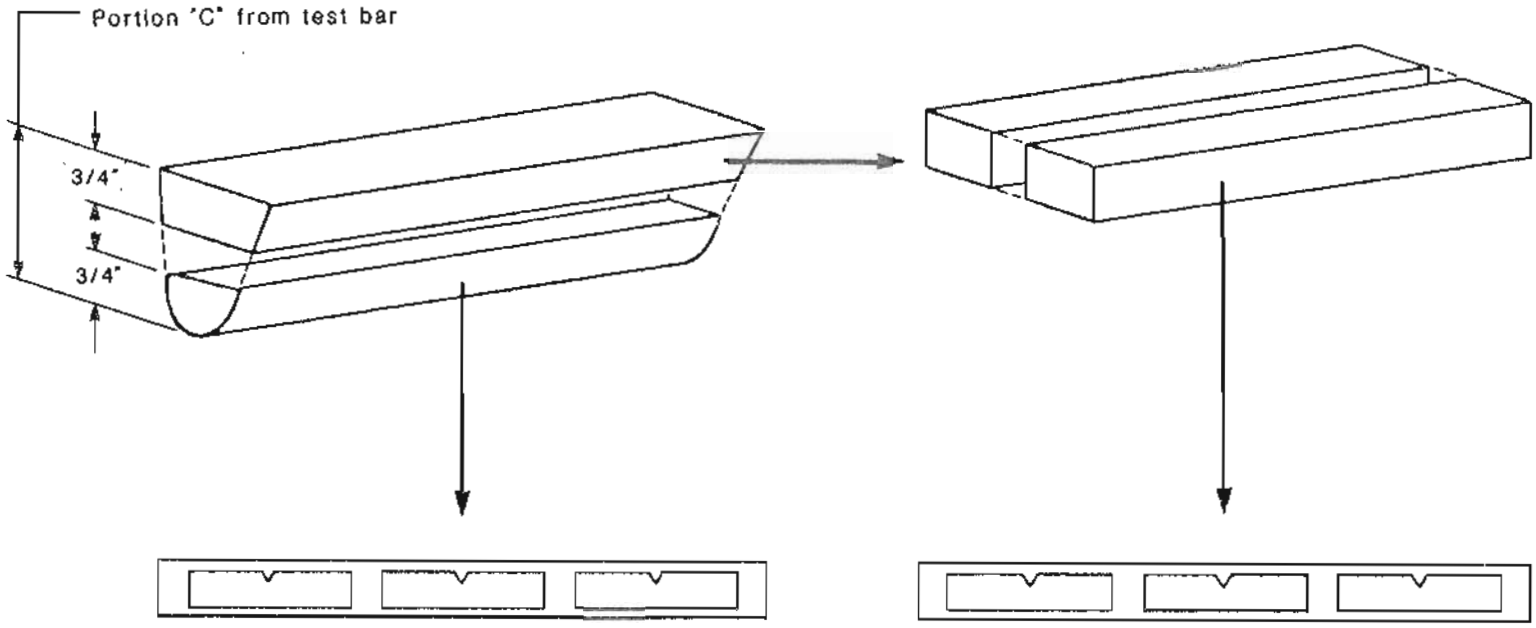

Charpy vee-notch (CVN) configuration showing notch orientation

FIGURE #3 Sectioning test material for subsequent heat treatment and machining

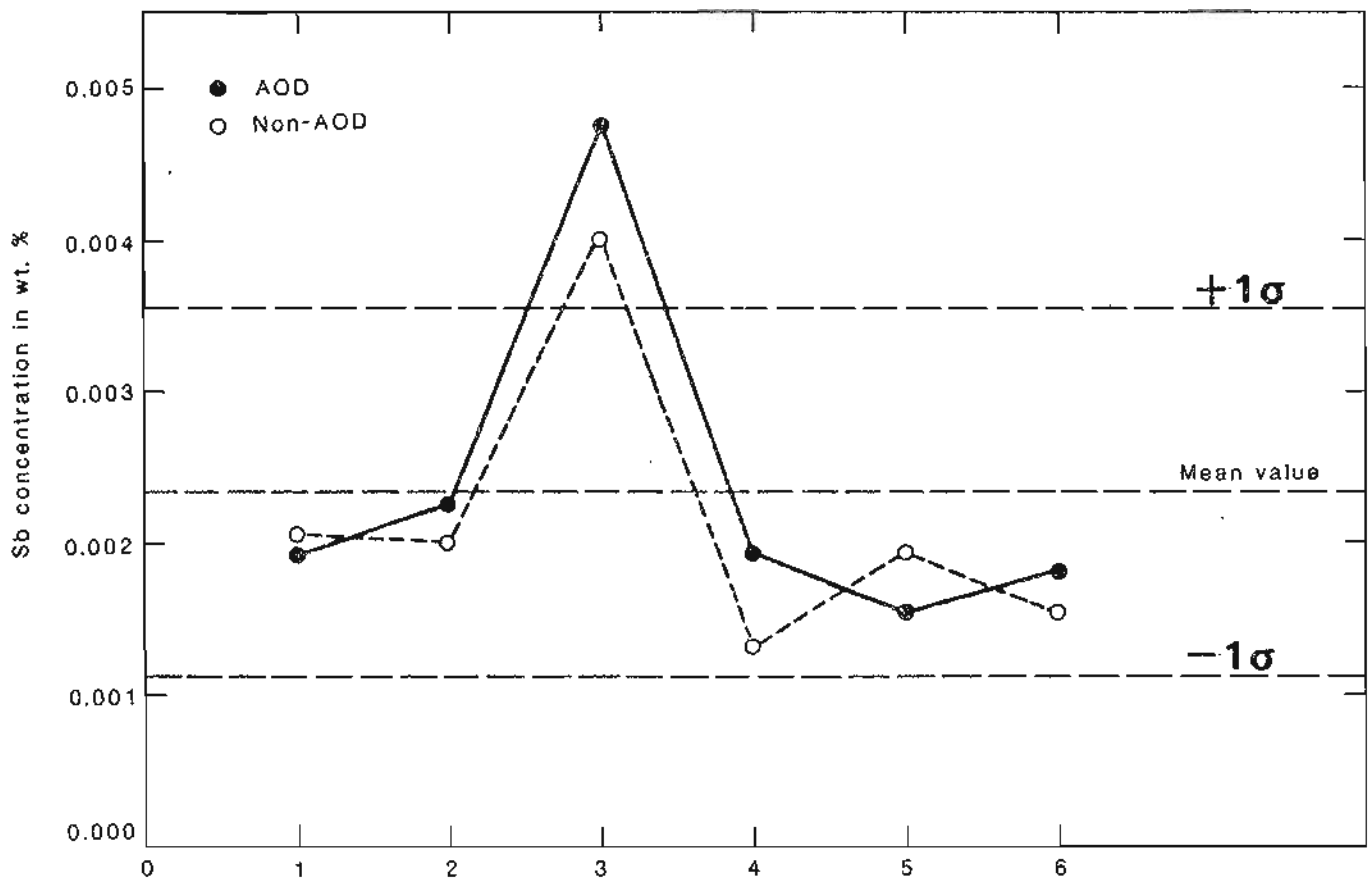

Sb concentration of AOD and non-AOD processed low alloy heats as a function of time

FIGURE #4

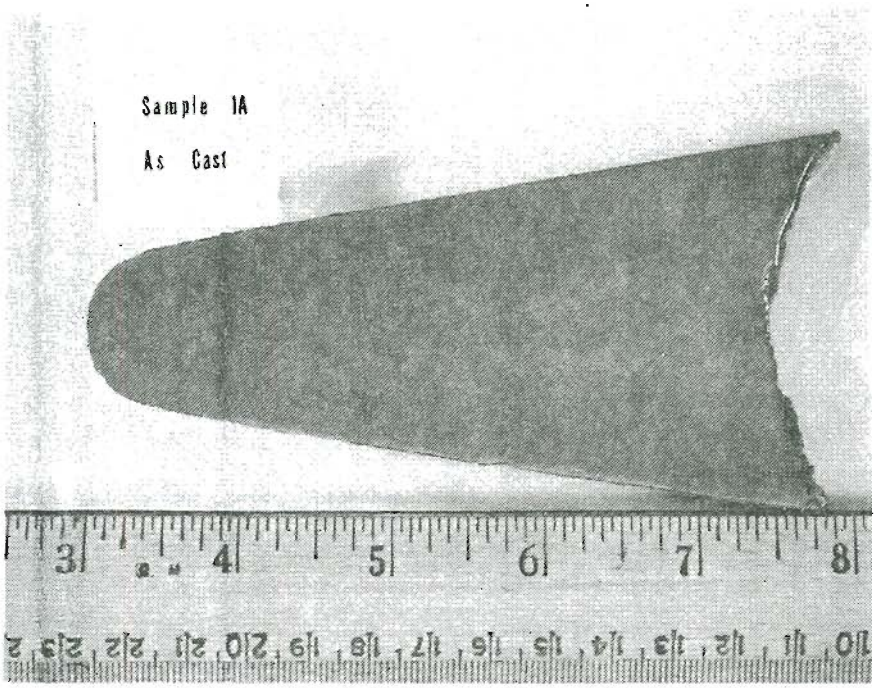

Fig.#5 Etched vertical slab Vilella's

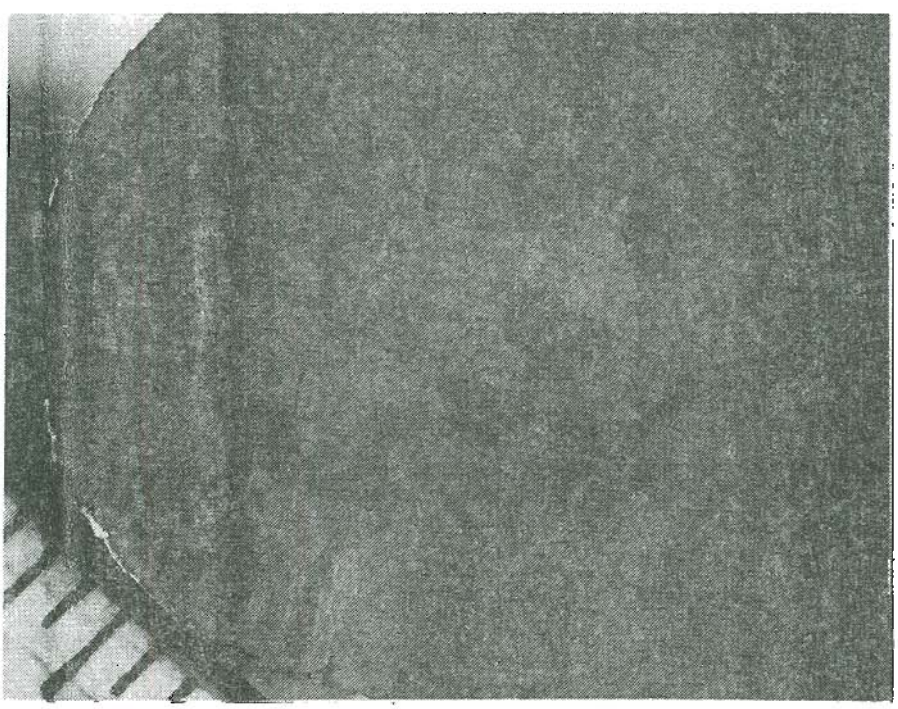

Fig.#6 Group 1-A. Etched as cast vertical slab
Vilella's 4X

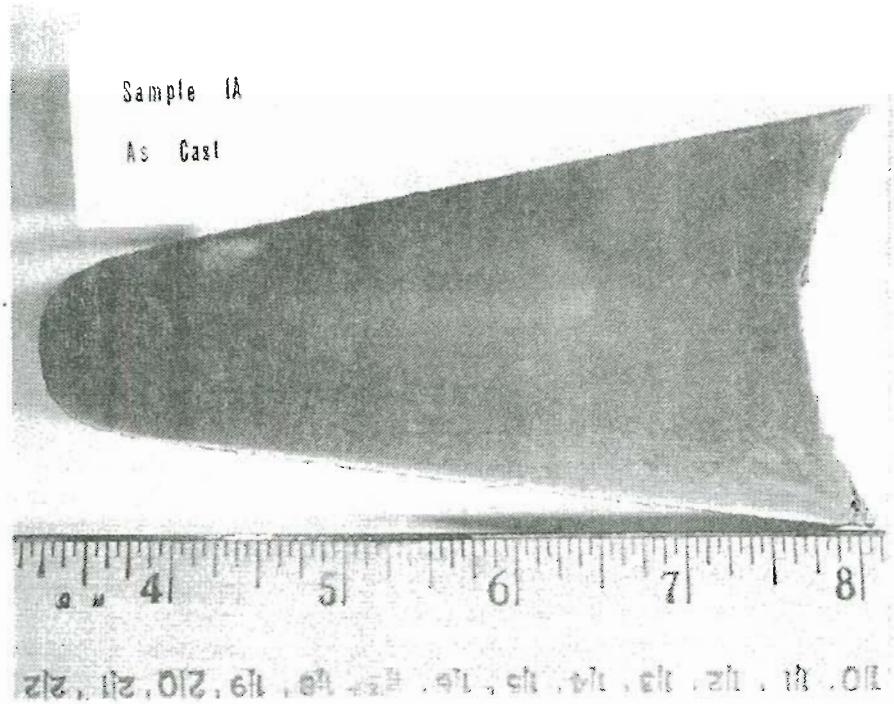

Fig.#7 Etched vertical slab Steads

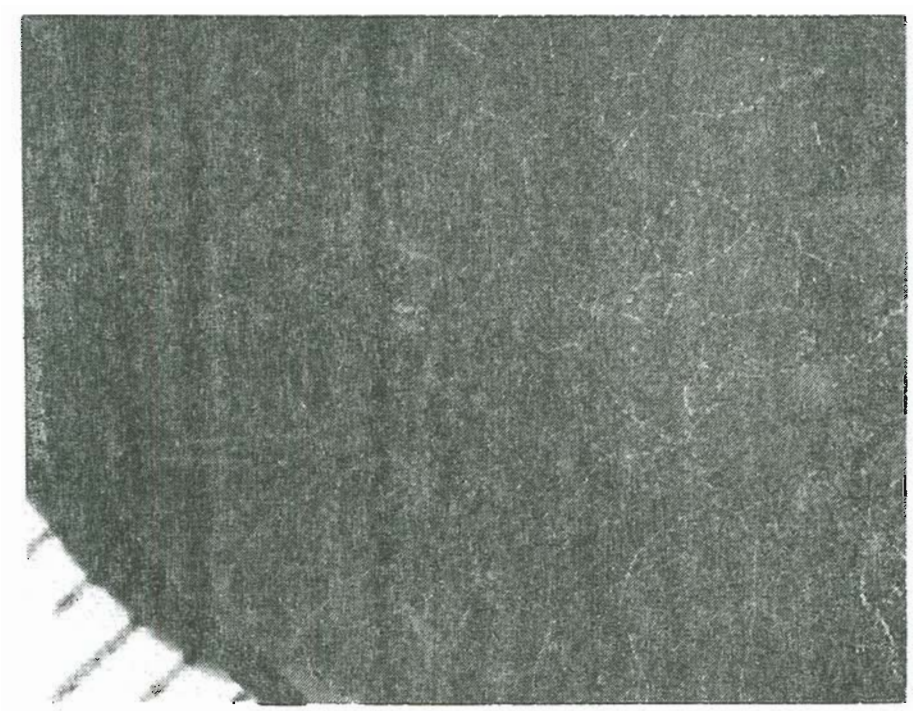

Fig.#8 Group 1-A. Etched as cast vertical slab. Steads 4X

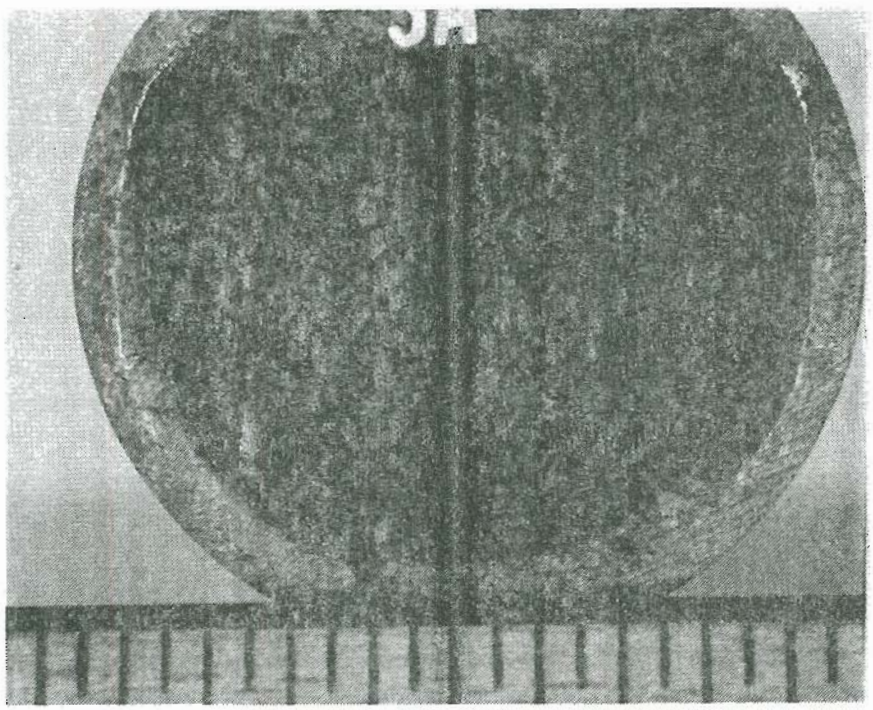

Fig.#9 As cast metallographic sample, group III-A. Note dendrite arm orientation. Steads 3.5X

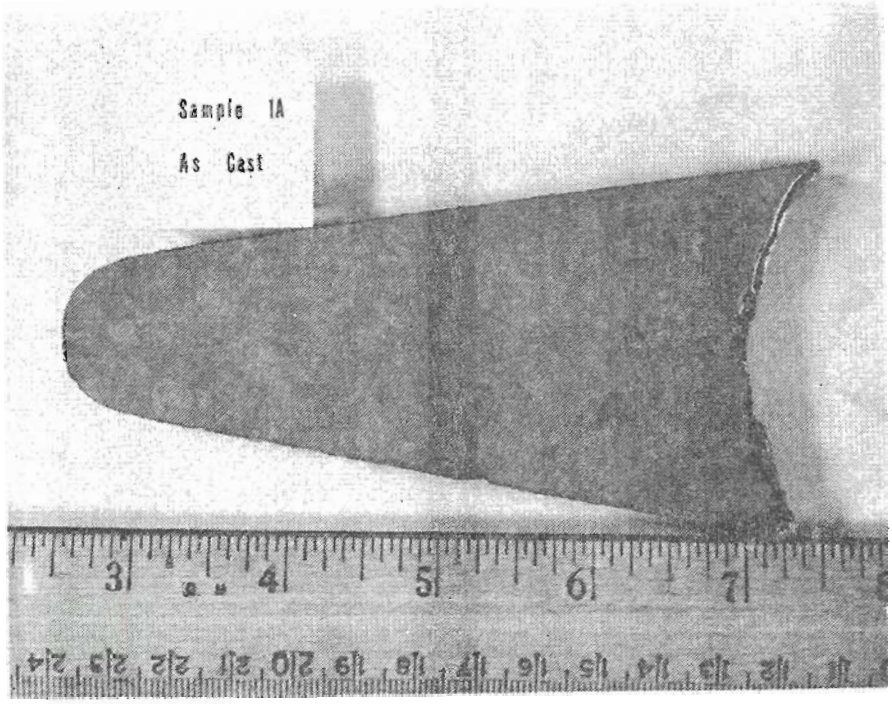

Fig.#10 Etched vertical slab. Aqua regia 0.8X

Fig.# 11 Group 1-A. Etched as cast vertical slab. Aqua Regia 0.8X

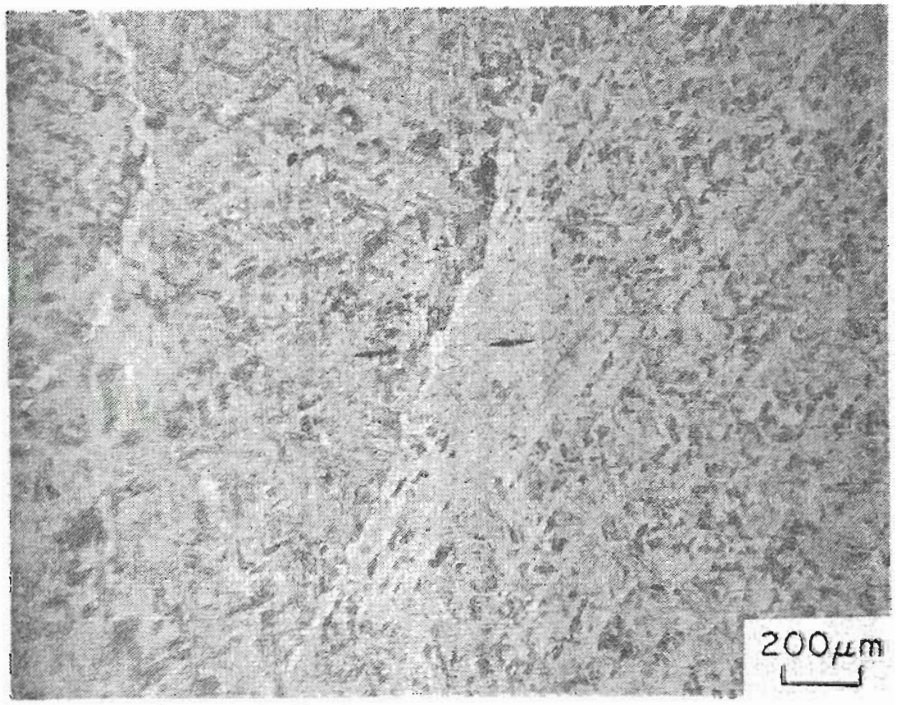

Fig.# 12 Group I-D. Bainitic matrix with pro-eutectoid ferrite at grain boundries. Vilella's 50X

Group #1

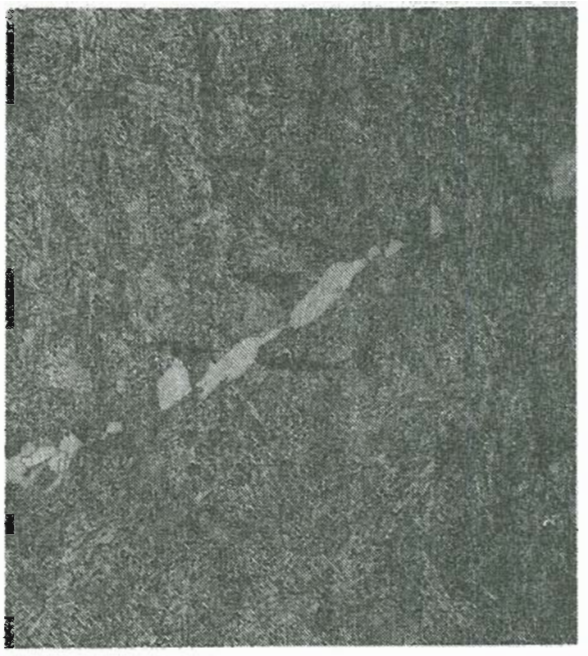

Group #2

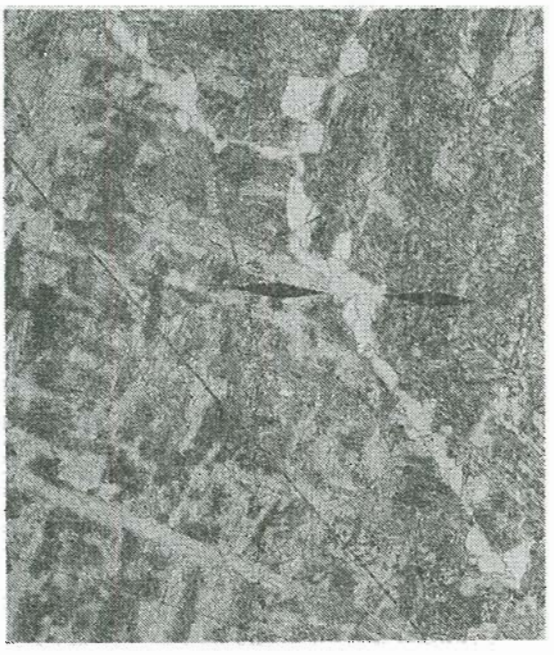

Group #3

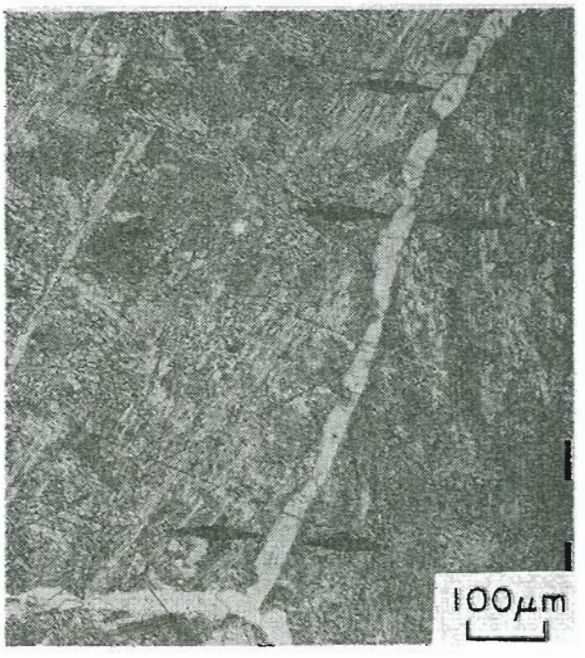

Group #4

Fig.#13 Increasing proeutectoid ferrite at prior austenite grain boundaries with increasing Sb content. Vilella's 100X

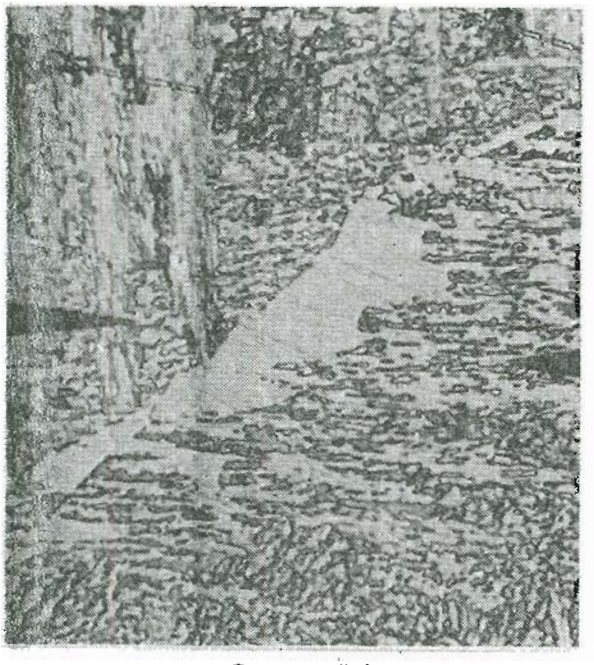

Group#1

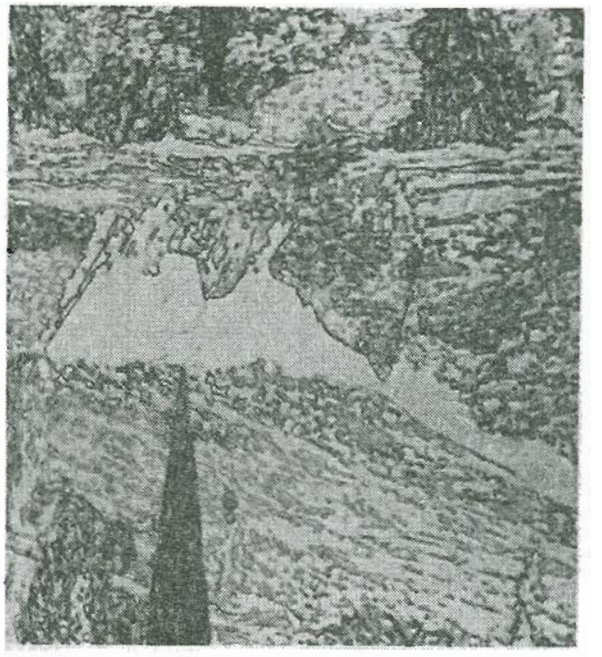

Group#2

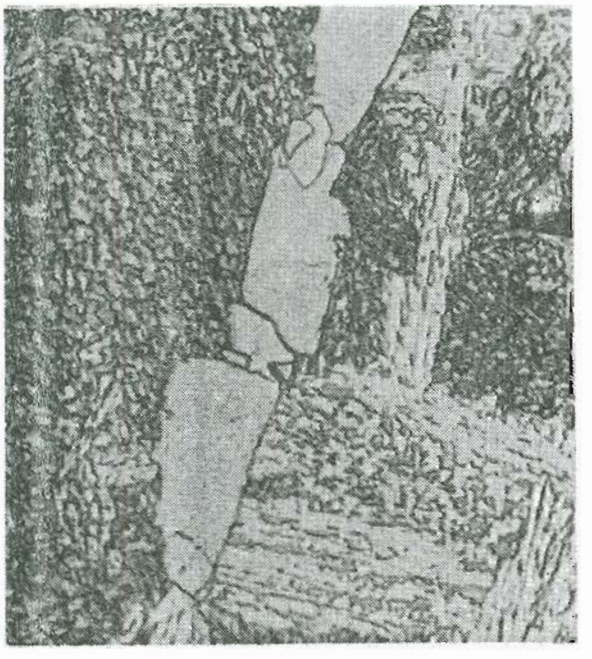

Group#3

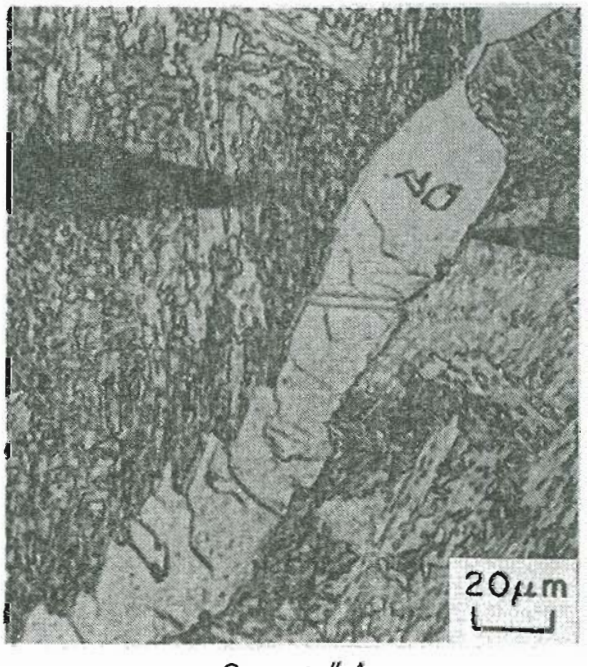

Group#4

Fig.#14 Increasing proeutectoid ferrite at grain boundaries with increasing Sb content. Vilella's 500X

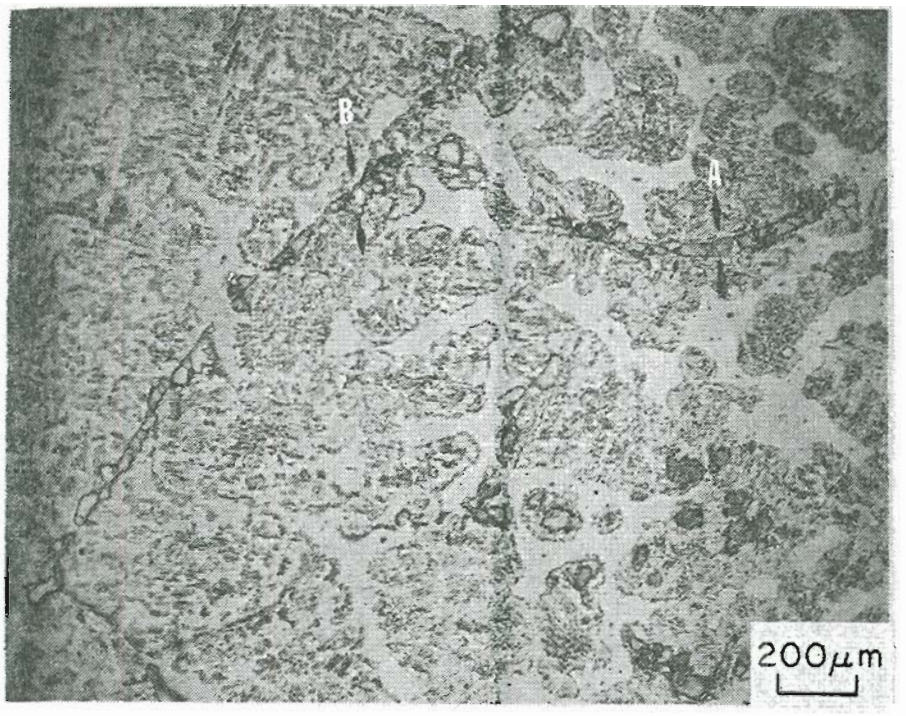

Fig.#15 Note random ferrite (R.F.) in lower right hand corner, in color Group IV-B. Steads 50X

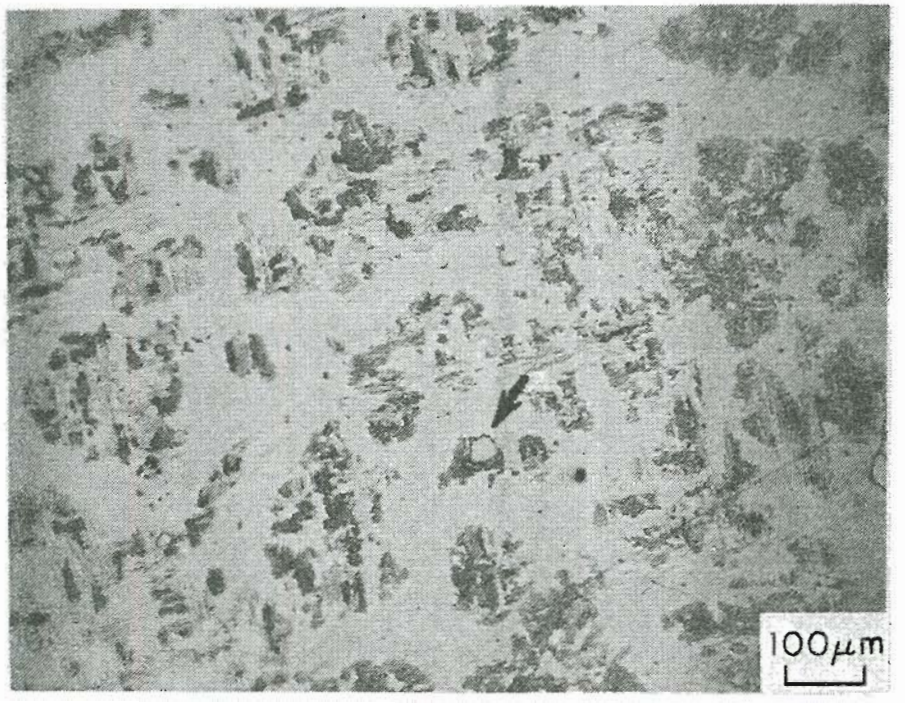

Fig.#16 Group IV. Note R.F. at arrow, in color. Steads 100X

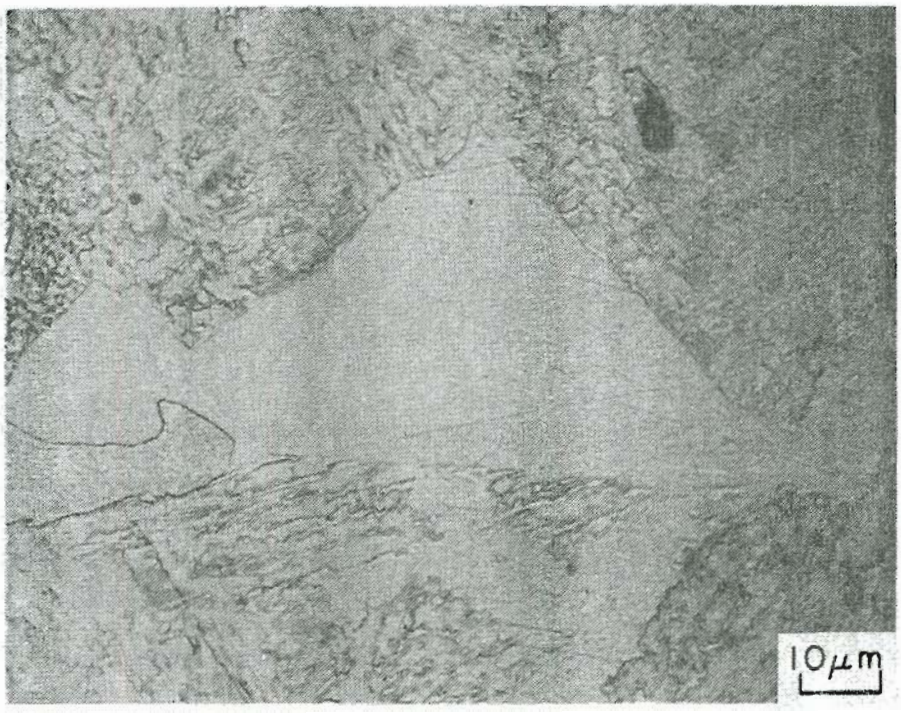

Group I 1000X

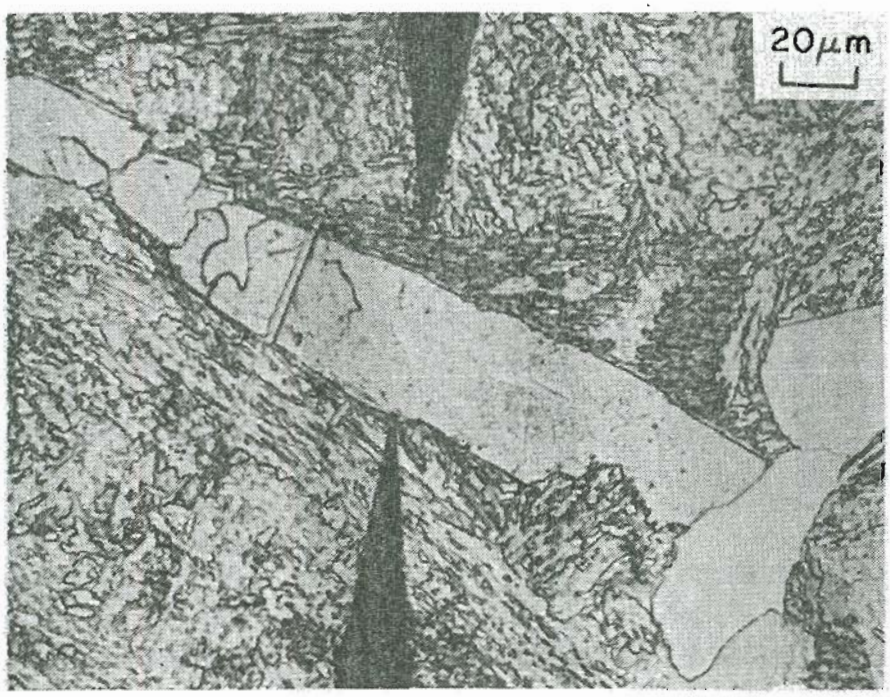

Group IV 500X

Fig.#17 Differences in ferrite staining behavior with Vilella's reagent.

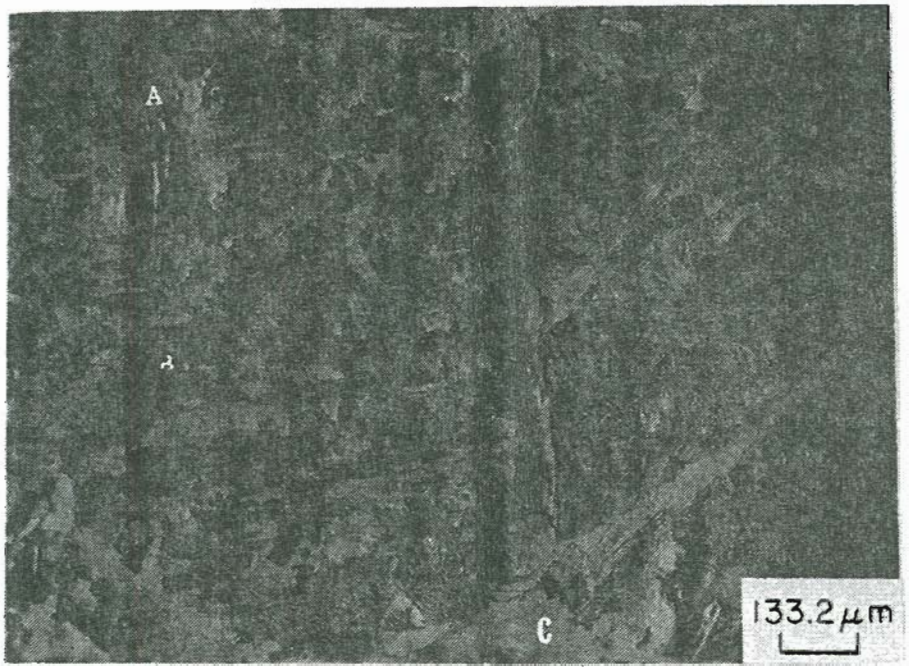

Fig.#18 Note areas A, B, and C. Group IV
Vilella's 76X

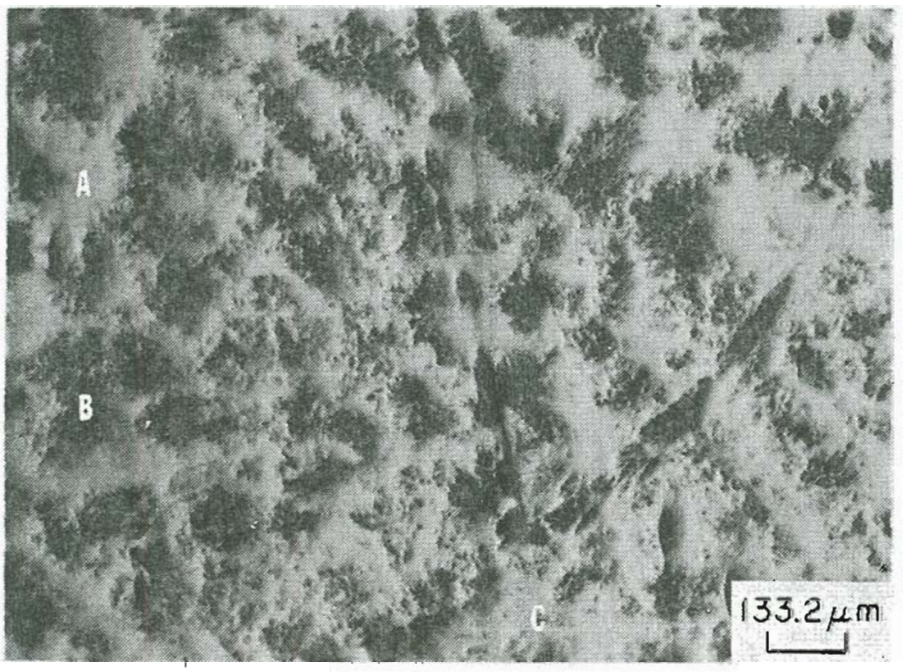

Fig.#19 Same location as Fig.#18
Compare dendrite arm locations to dark regions in Fig.#18
Steads 76X

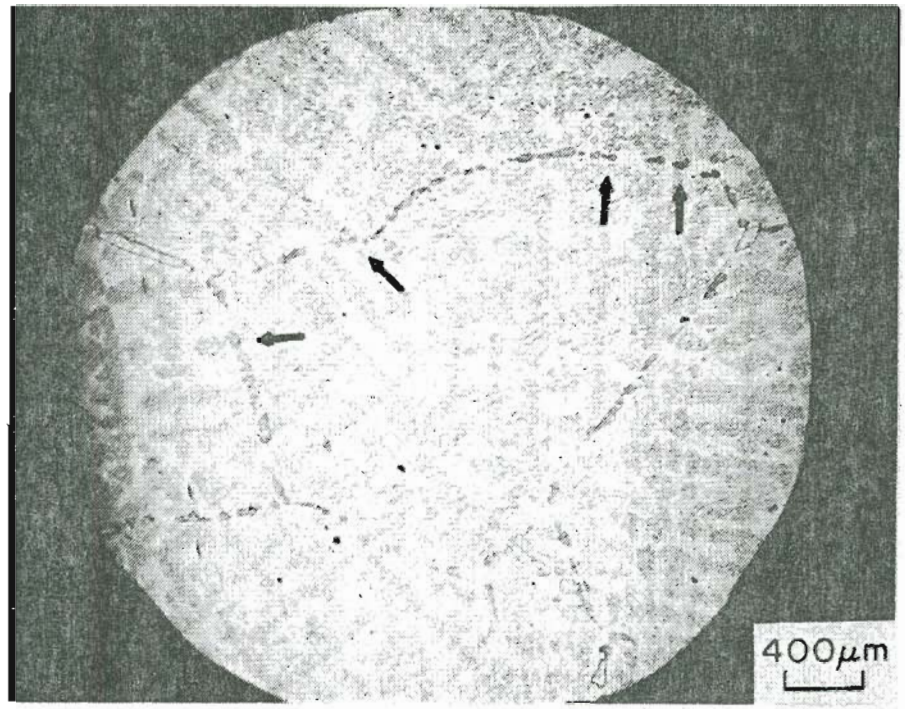

Group I Steads 25X

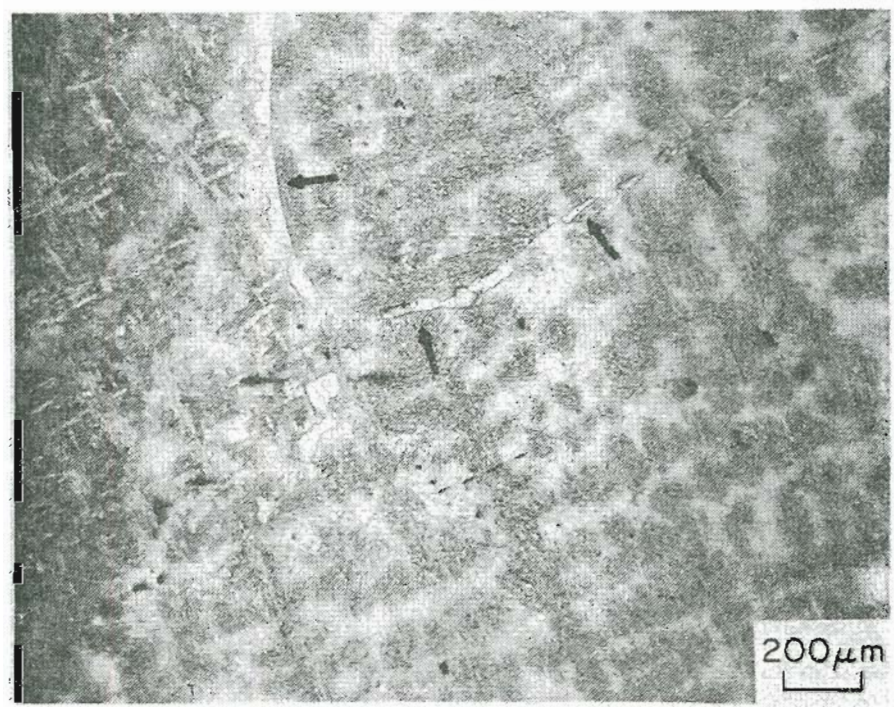

Fig.#20 Group II Dendritic solidification pattern.
Note relationship between ferrite and dendrite arm locations.
Steads 50X

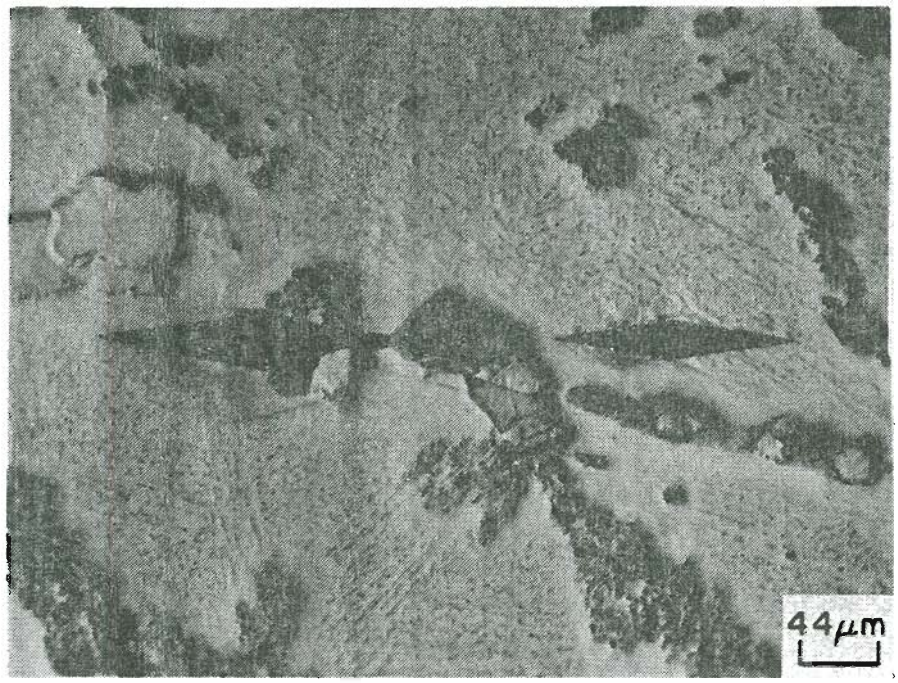

Fig.#21 Group IV-C, GB#3. Example of S.F.. Steads 225X

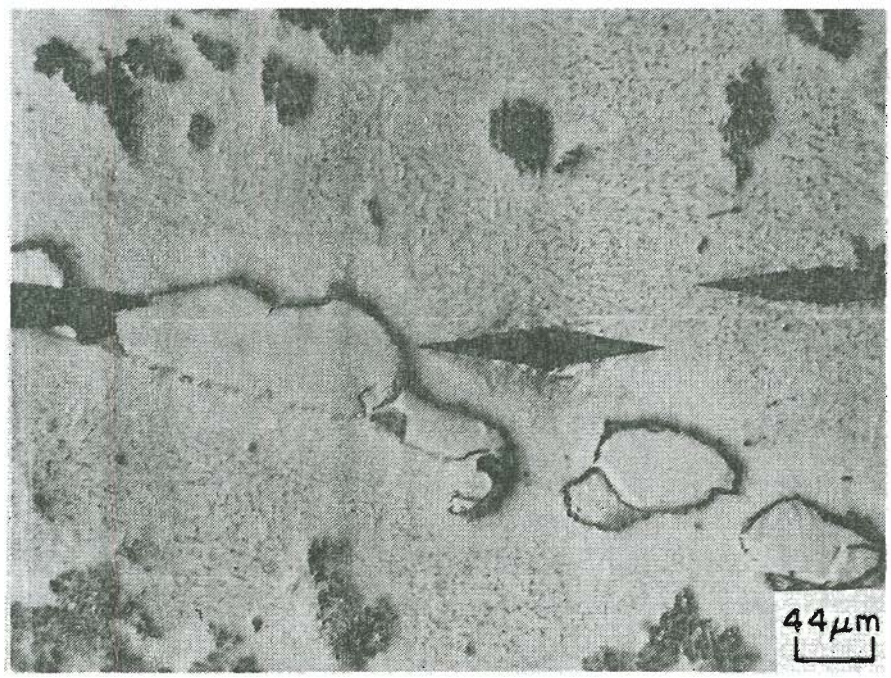

Fig.#22 Group IV-C, GB#3. Example of U.S.F.. Steads 225X

Group #I

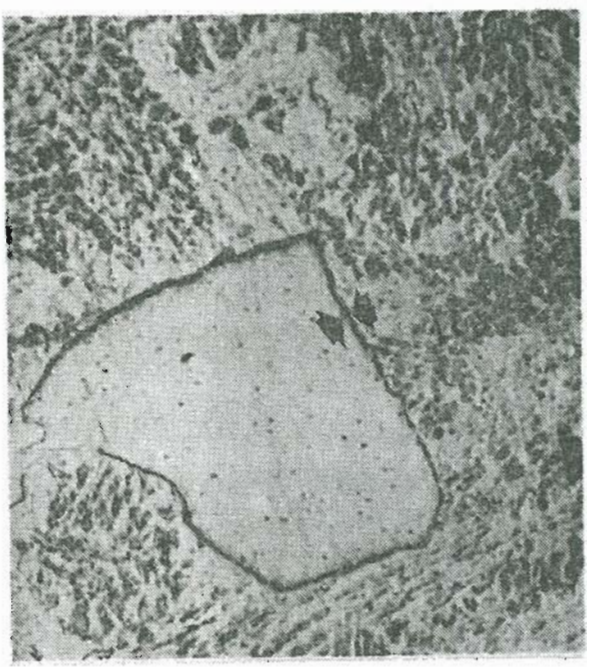

Group #II

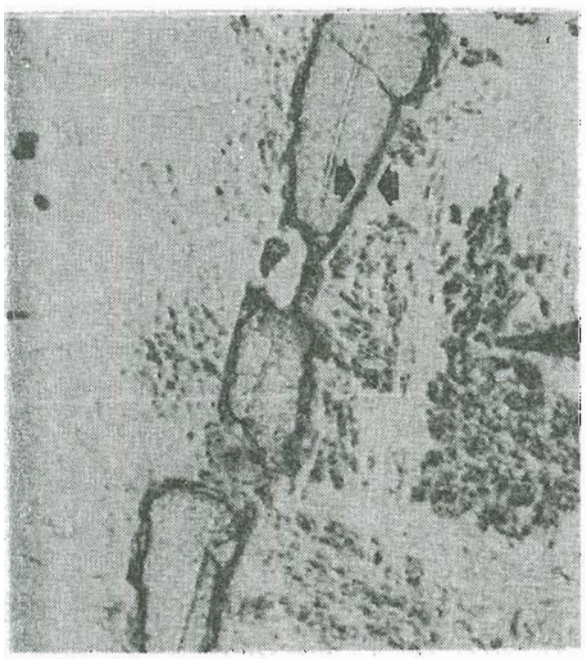

Group #III

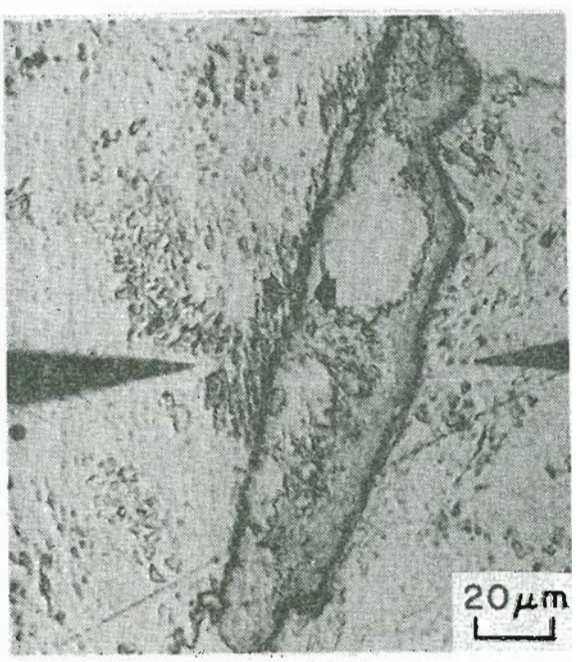

Group #IV

Fig.#23 Increasing ferrite/bainite interface etching characterics with increasing Sb content. 500X Steads

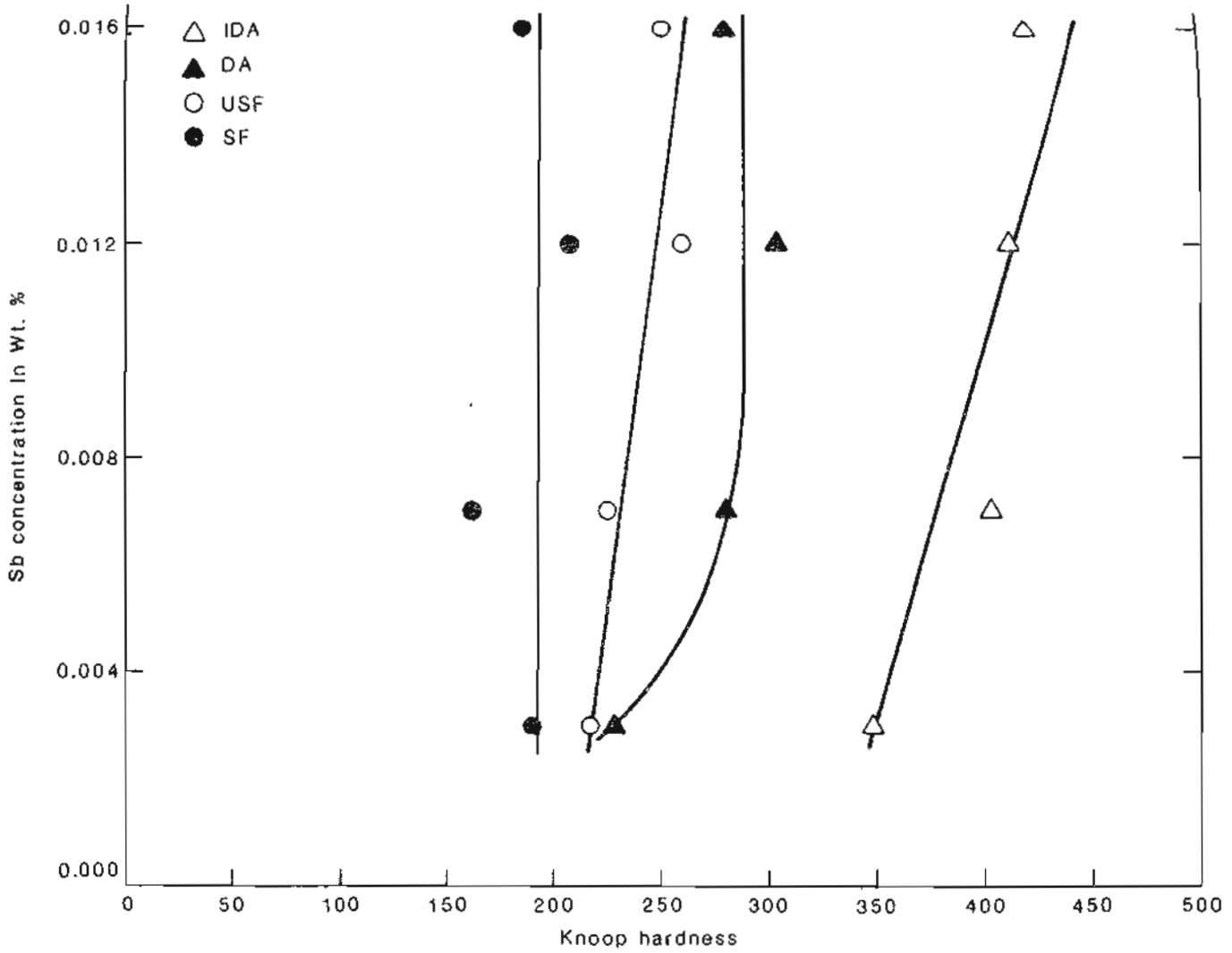

FIGURE #24

As cast microhardness variations of selected microstructural regions VS Sb content

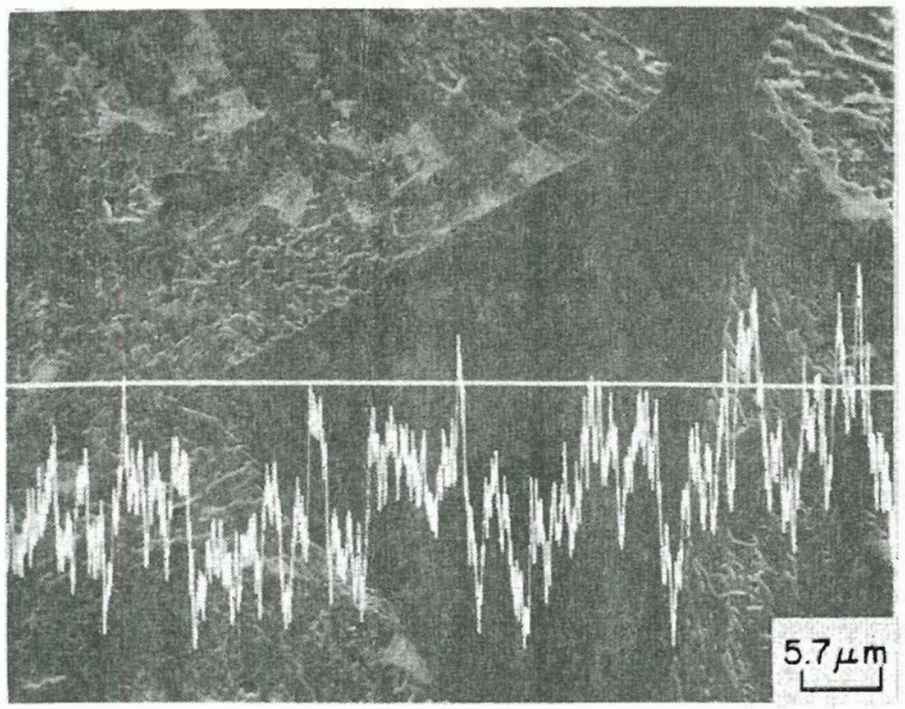

Fig.#25 Si line scan. No apparent change in alloy element content across pro-eutectoid ferrite. Group I-D,GB#2. Vilellas

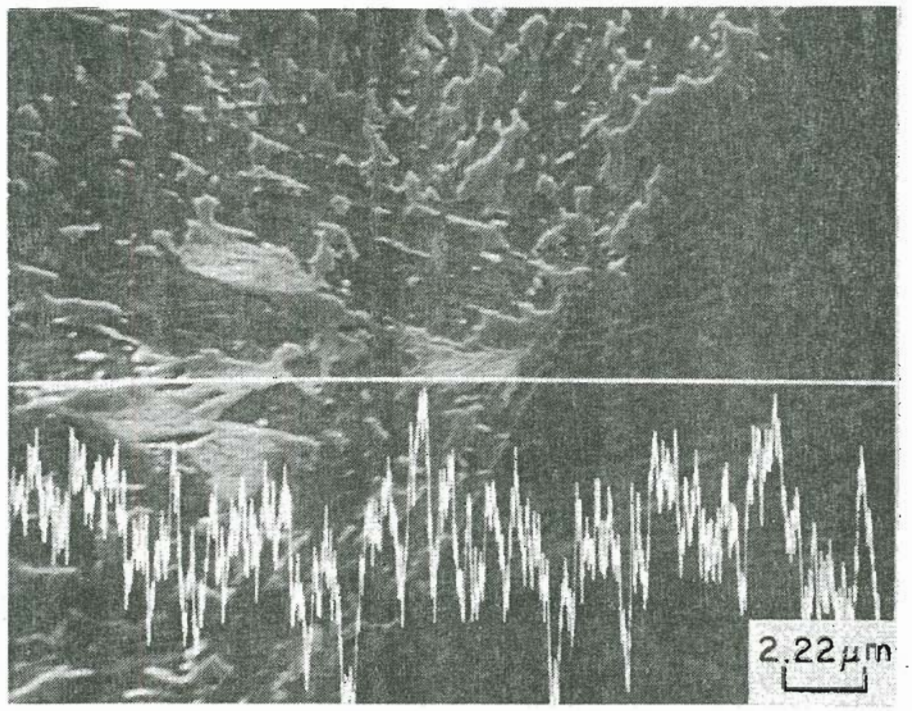

Fig.#26 Cr line scan. No apparent change in alloy element content across bainite/ferrite interface. Poor signal to noise ratio. Group I-D, GB#1. Vilella's

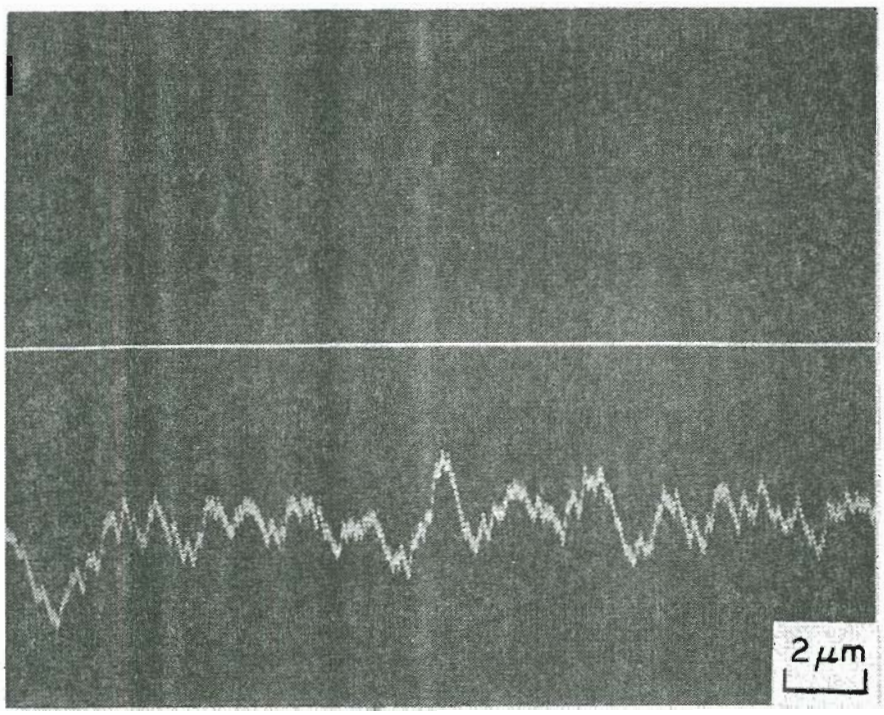

Fig.#27 Unetched Cr line scan. No apparent change in alloy element content across bainite/ferrite interface. Improved signal to noise ratio Group III-A, GB#3.

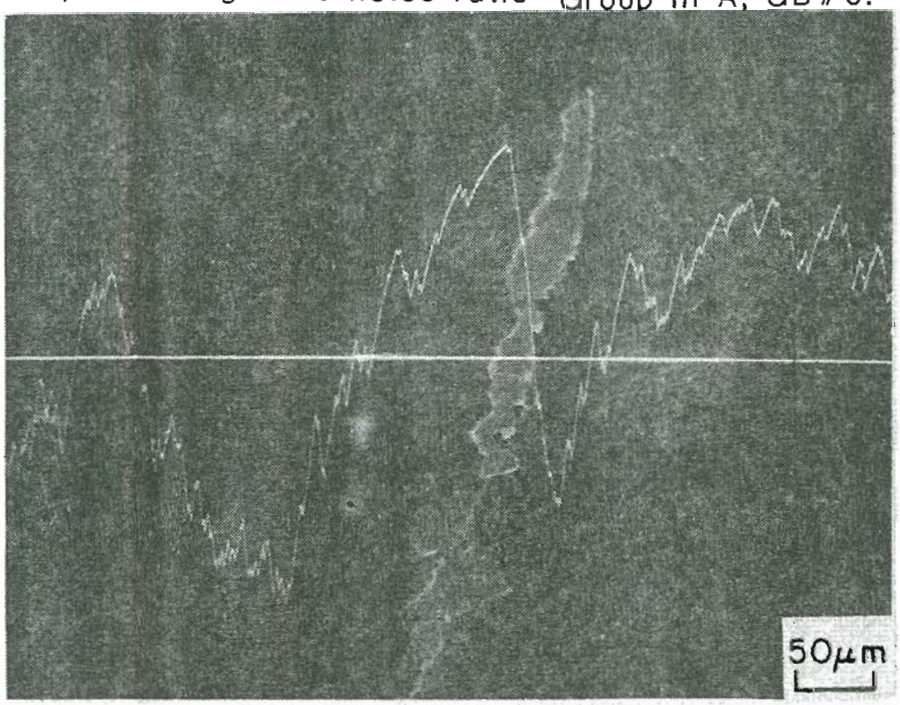

Fig.#28 Cu line scan. Group II
Quasi-sinusoidal Cu distribution Vs D.A. and I.D.A. regions
Steads

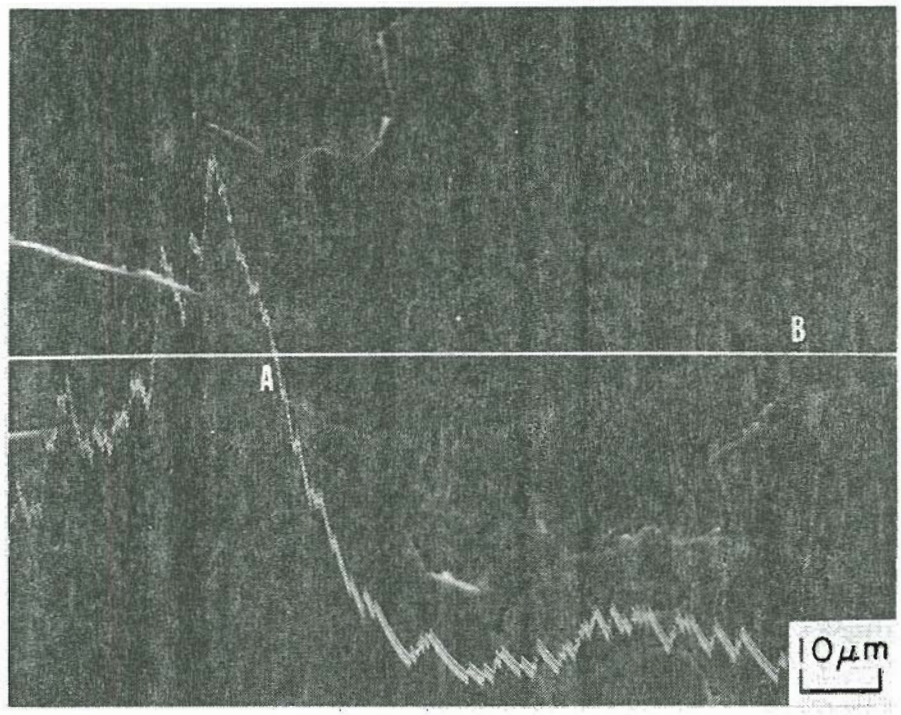

Fig.#29 Cu line scan across U.S.F. region.
Group IV-C, GB#2. Steads 1000X

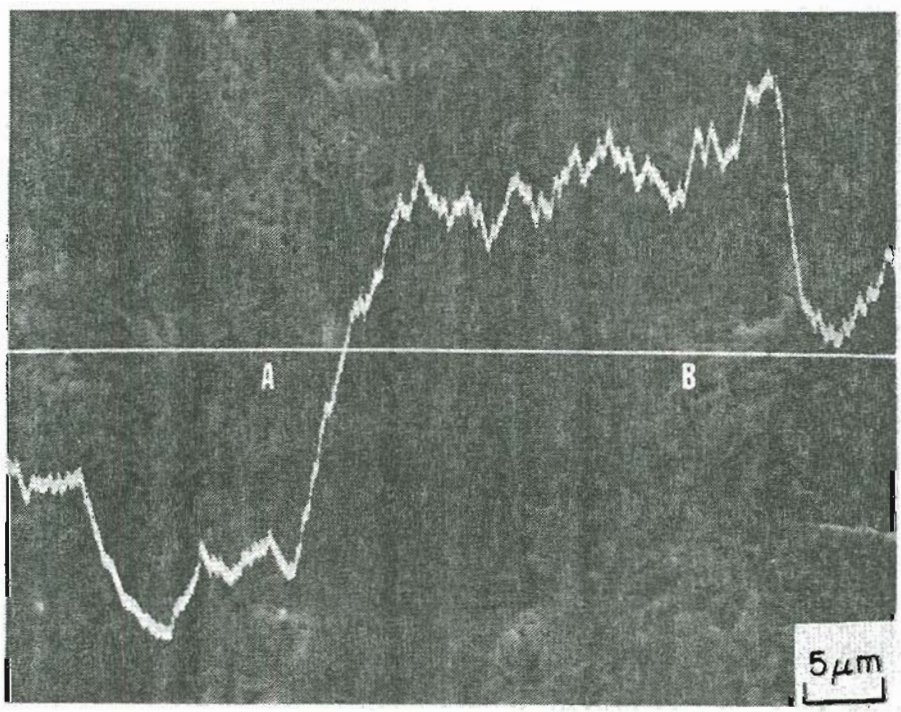

Fig.#30 Cu line scan across S.F. region.
Group IV-C, GB#1. Steads 2000X

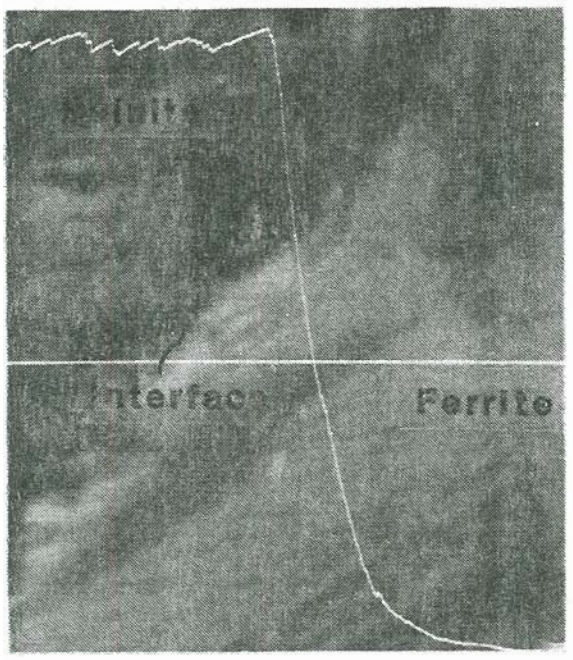

Group I

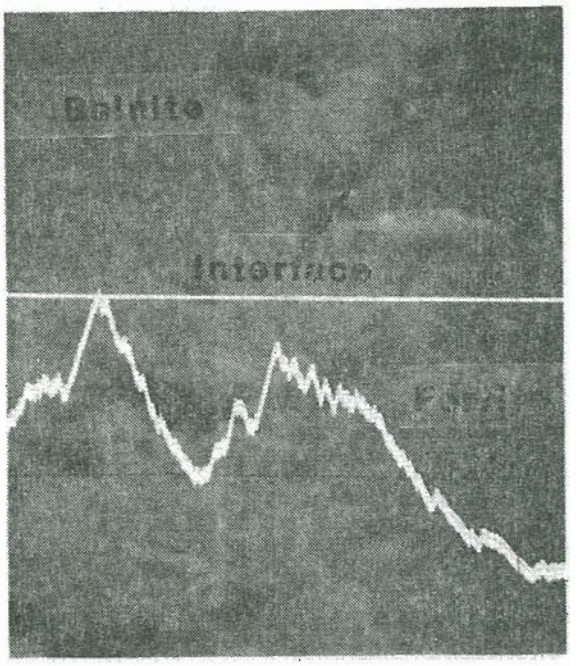

Group II

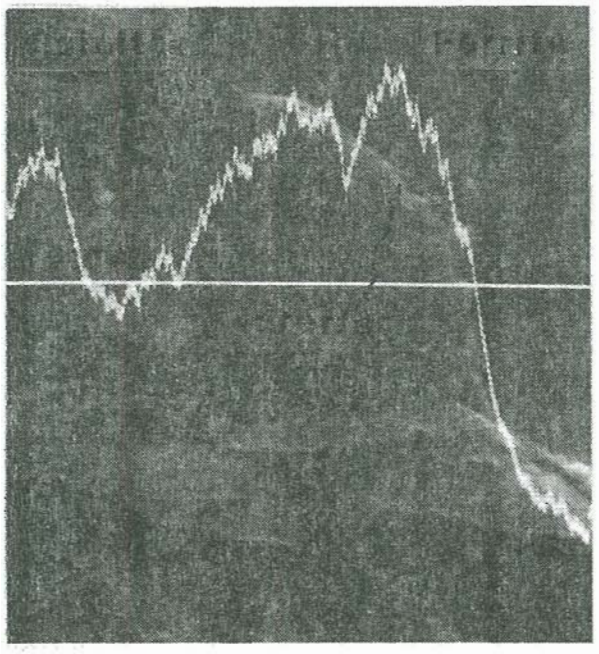

Group III

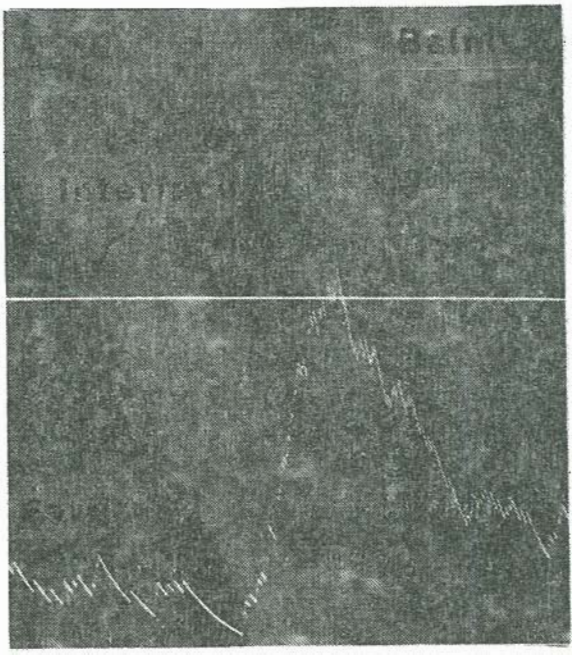

Group IV

Fig.#31 Cu line scans across ferrite/bainite interfaces. Note increasing Cu deposition on bainitic side of interface with increasing Sb content. Steads 10,000X

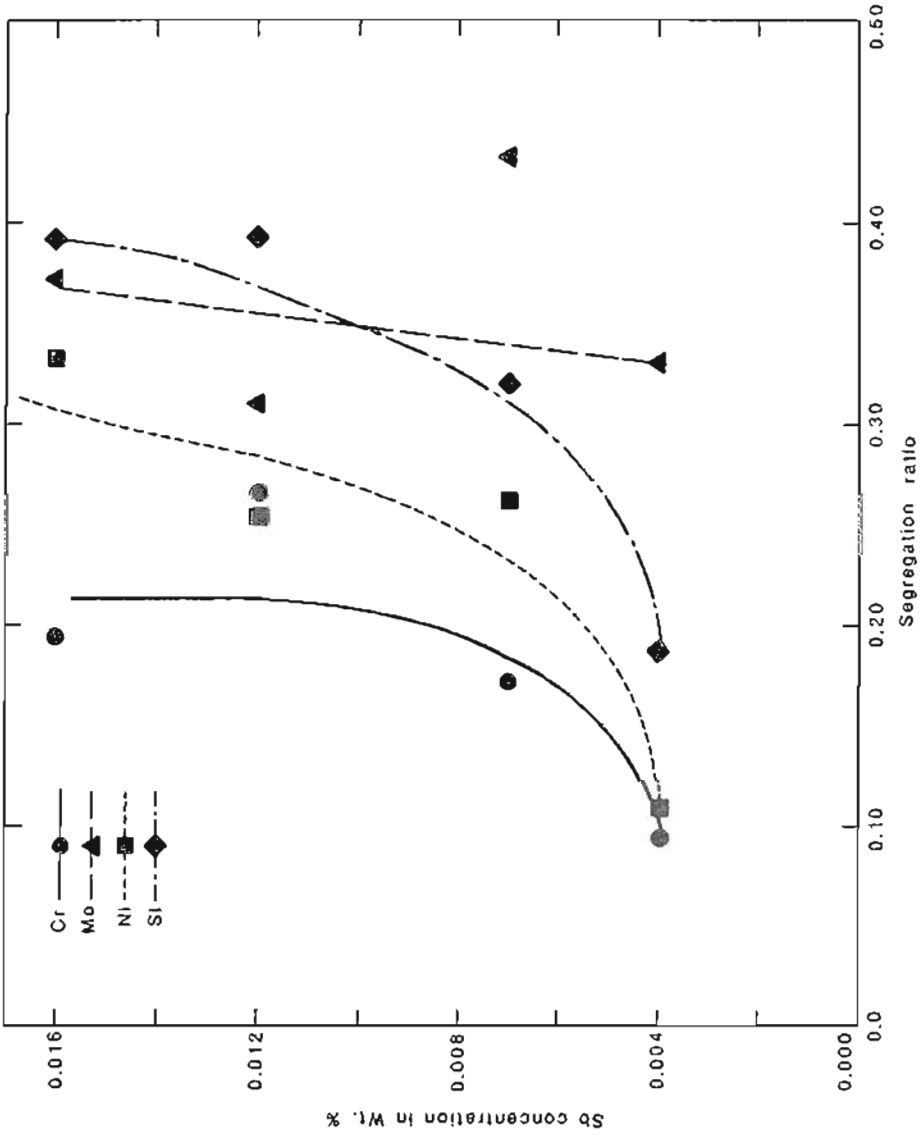

FIGURE #32 The segregation ratio of various elements VS Sb content

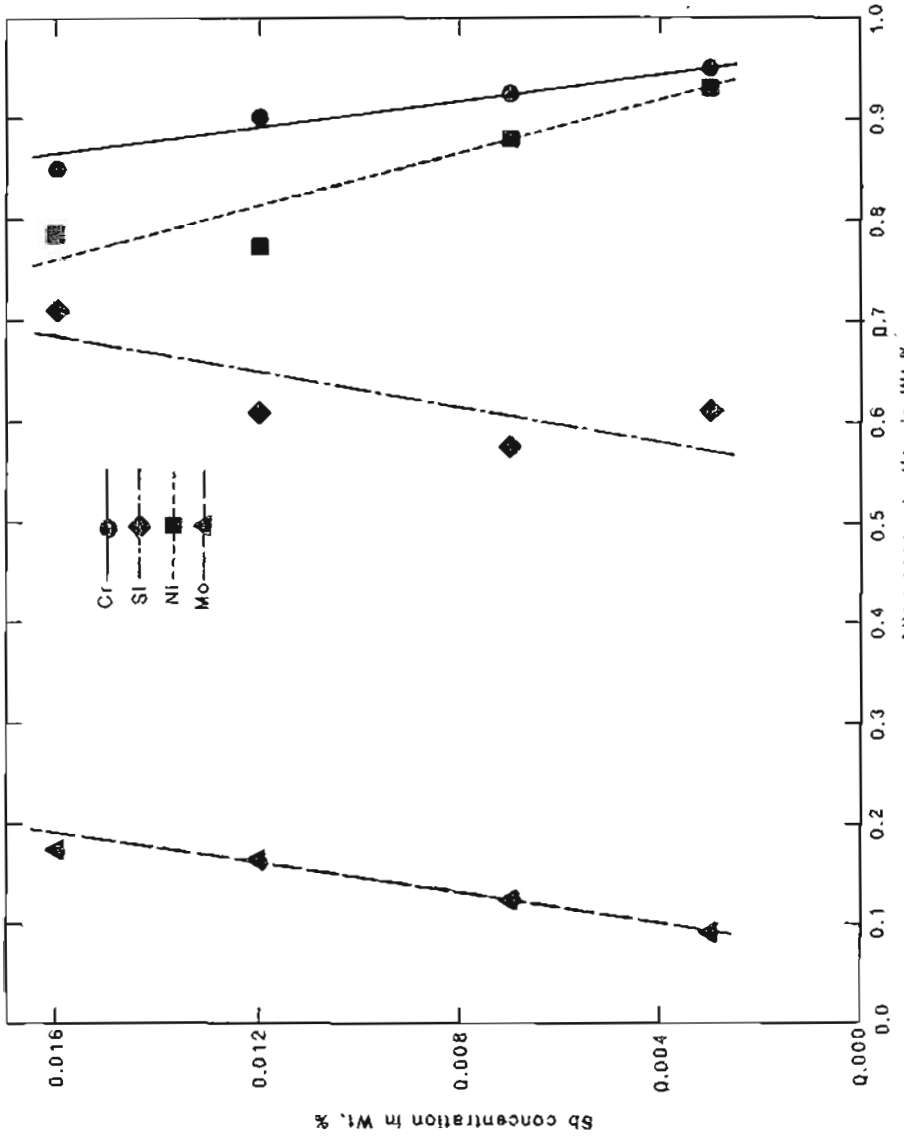

FIGURE #33 Compositional variations of unstained ferrite (USF)

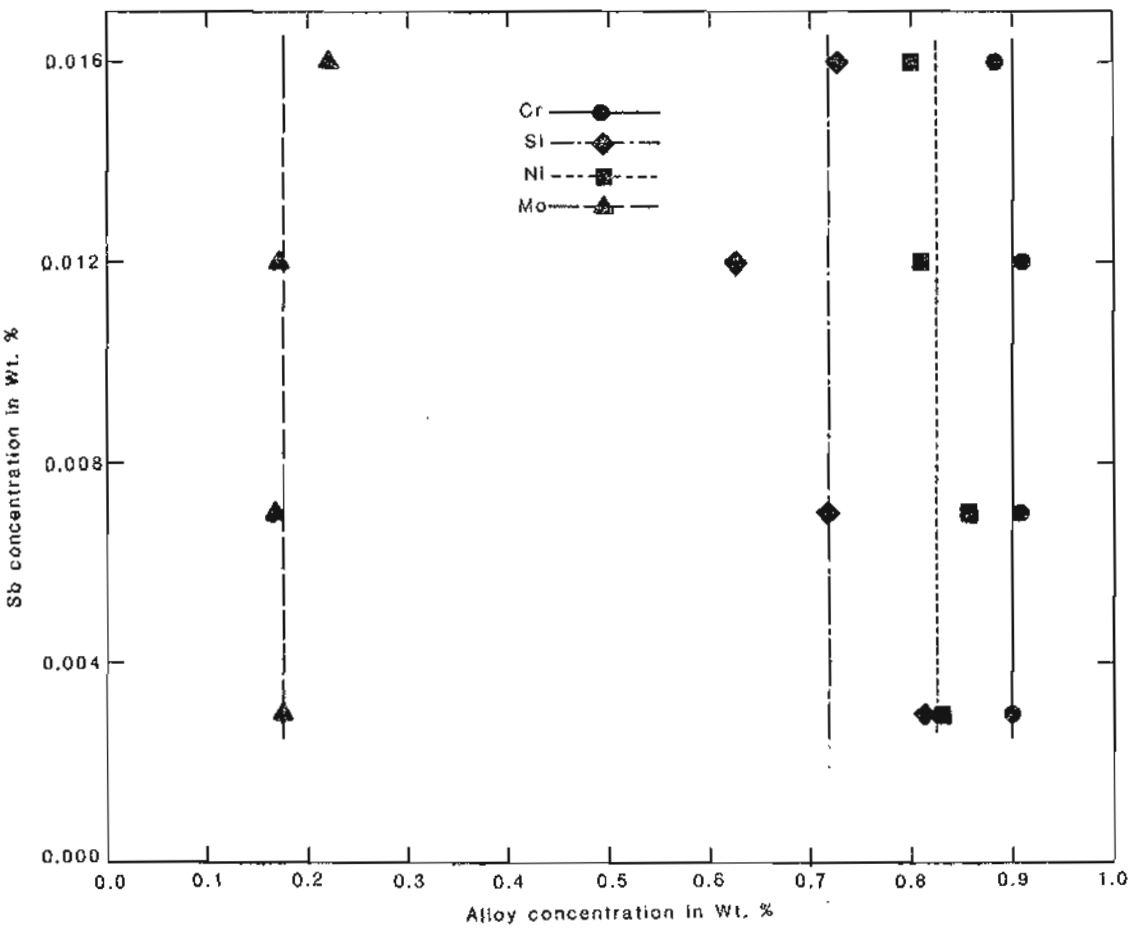

FIGURE #34 Compositional variation of stained ferrite (SF)

FIGURE #35 WDX analysis for C in selected regions
10Kv 25NA

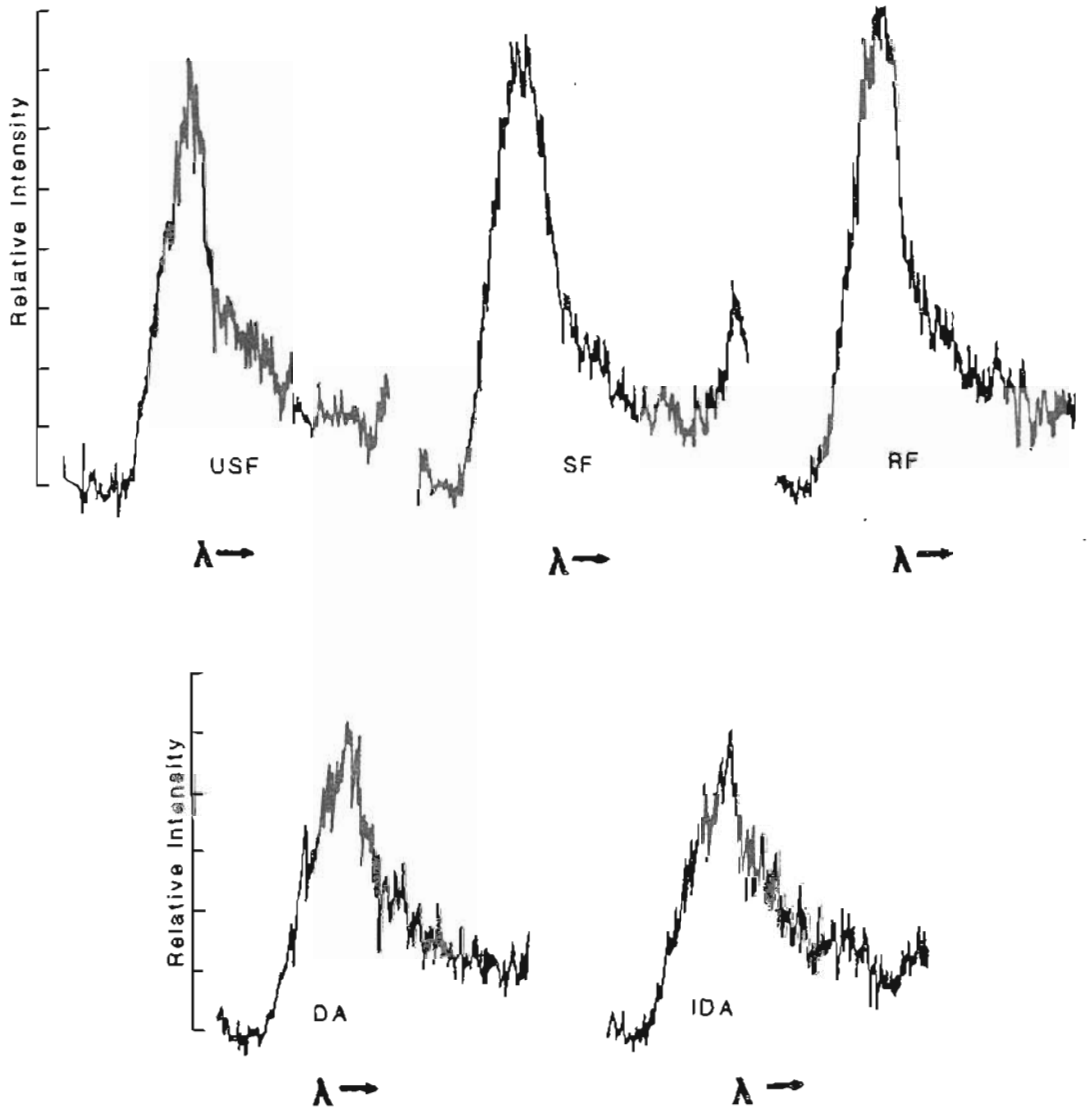

Note difference in peak height ratio between ferritic regions and DA/IDA regions.

FIGURE #38 WDX analysis for Sb in selected regions.
20Kv 30NA

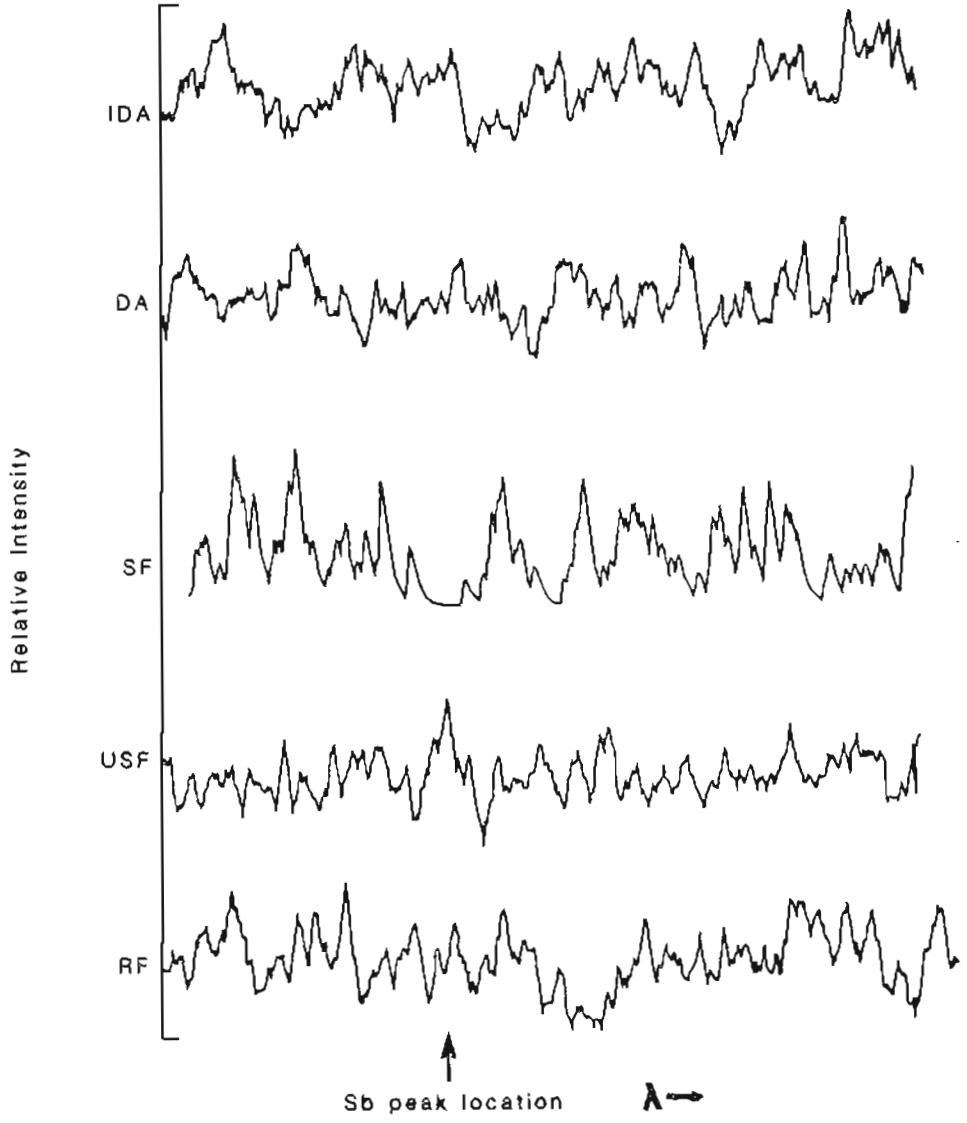

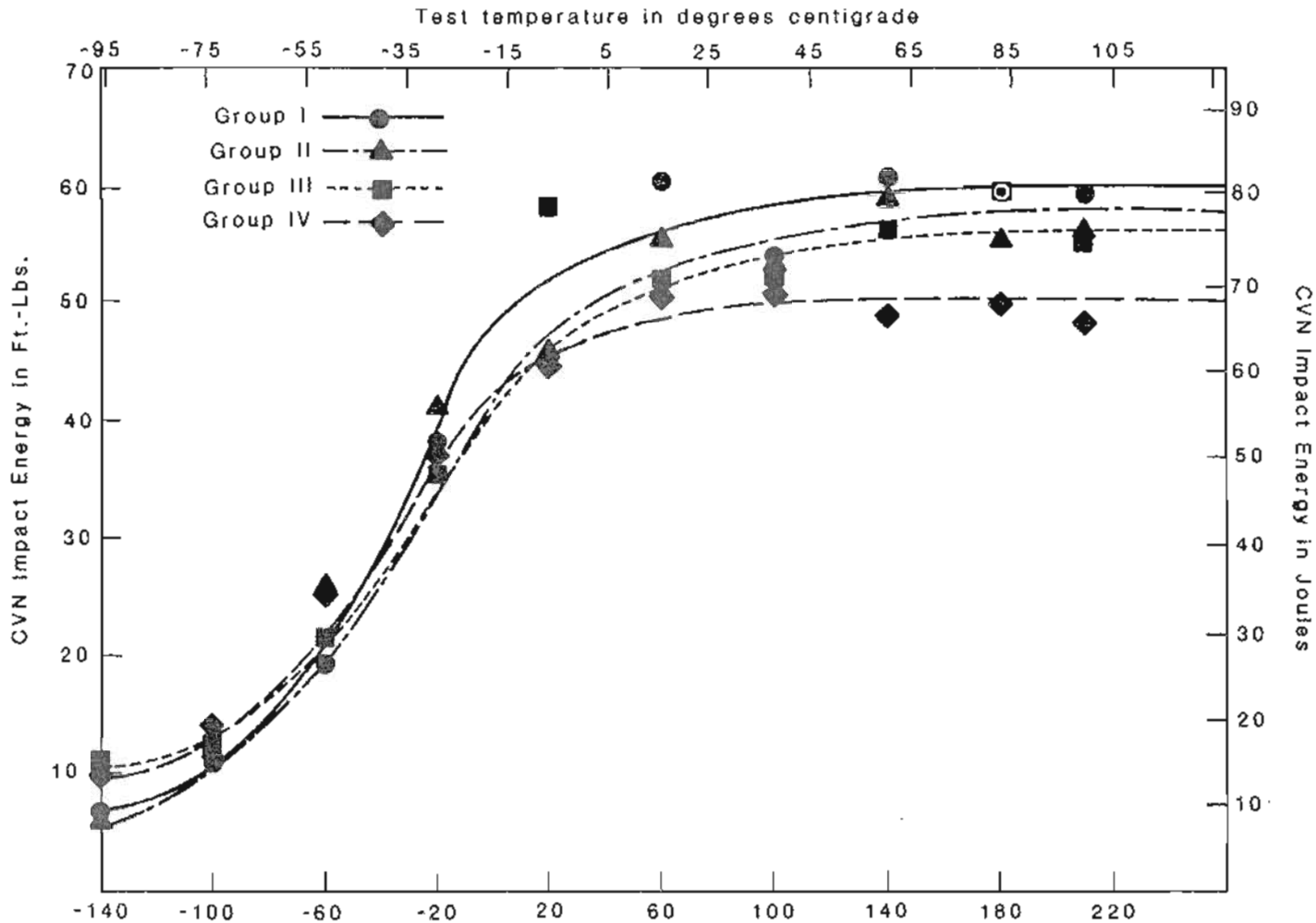

FIGURE #37 CVN Impact Energy Transition Curves

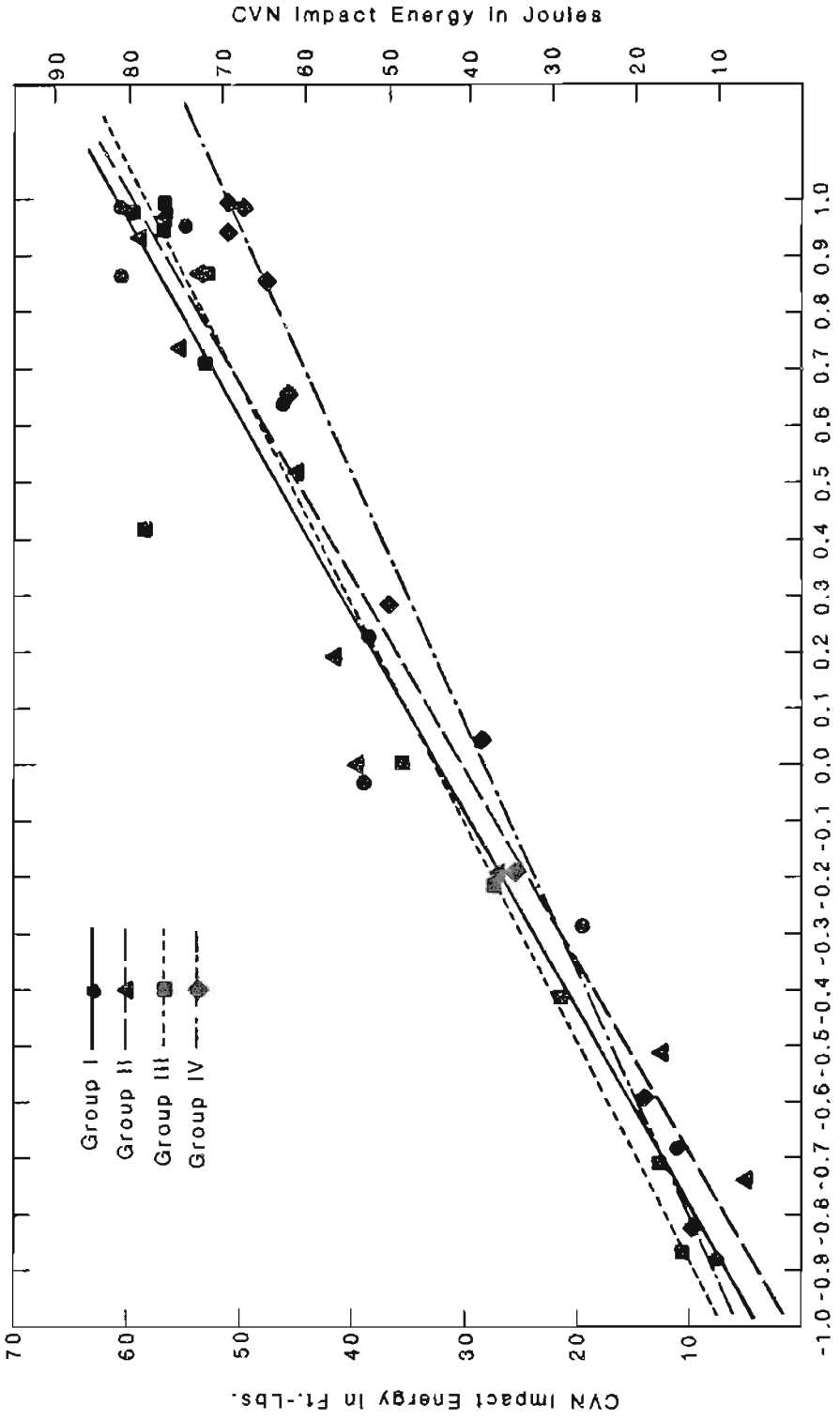

$$Z = \tanh\left[\frac{T-T_0}{C}\right]$$

FIGURE #38 CVN Impact Energy Values VS **Z**

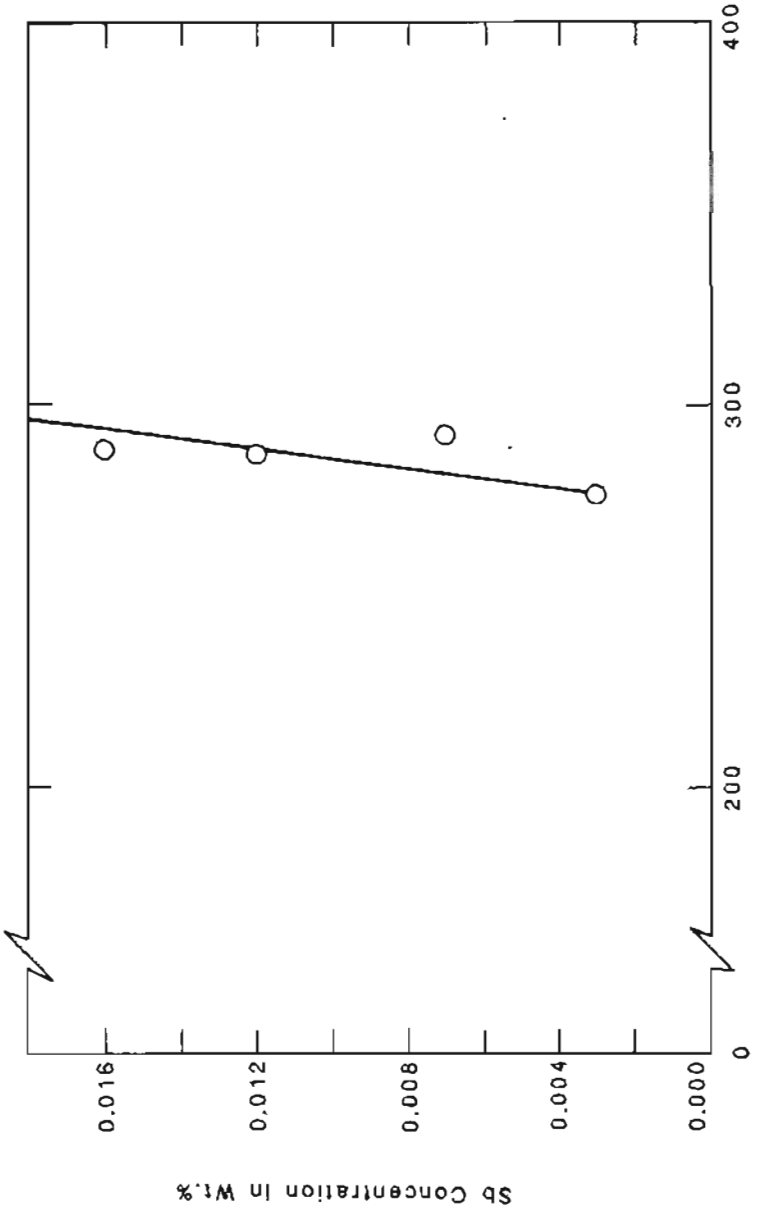

FIGURE #39 Brinell Hardness VS Sb Content
Heat Treated "A" Condition

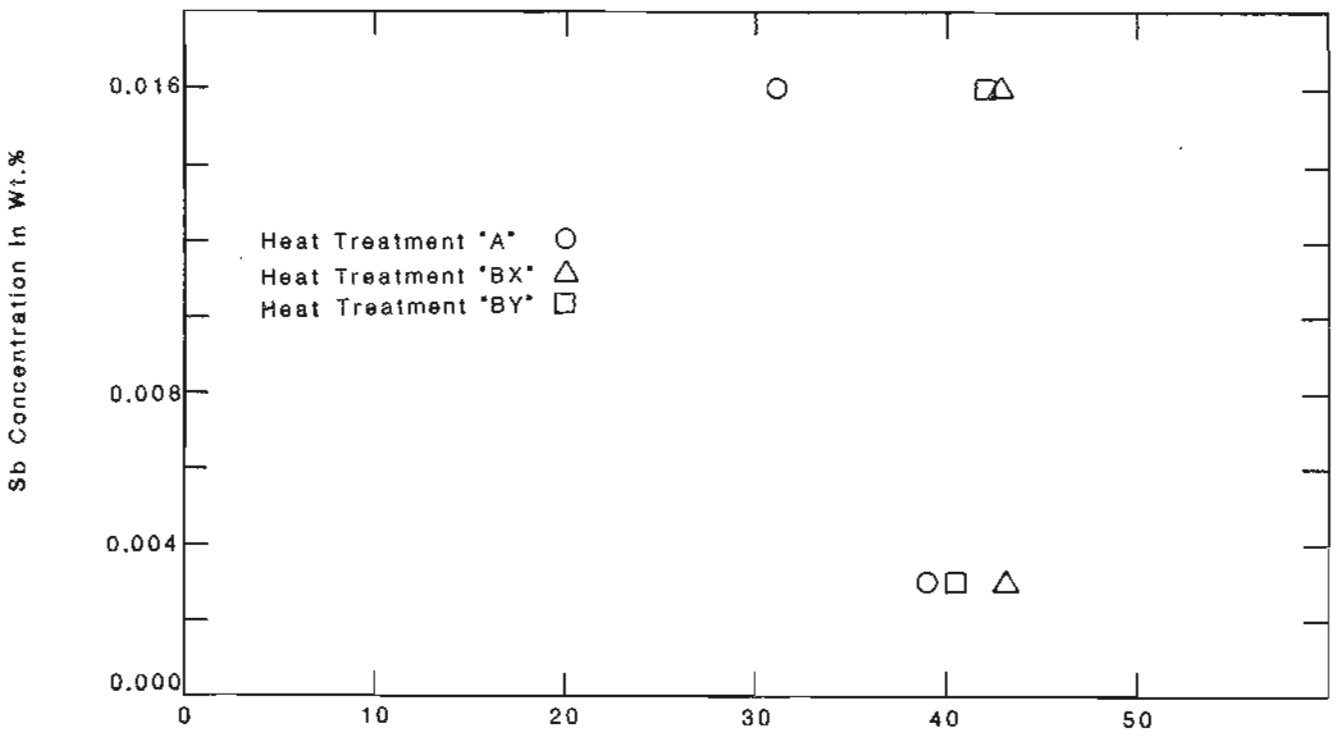

FIGURE #40 Effects of Various Heat Treatments on Impact Properties VS Sb Content

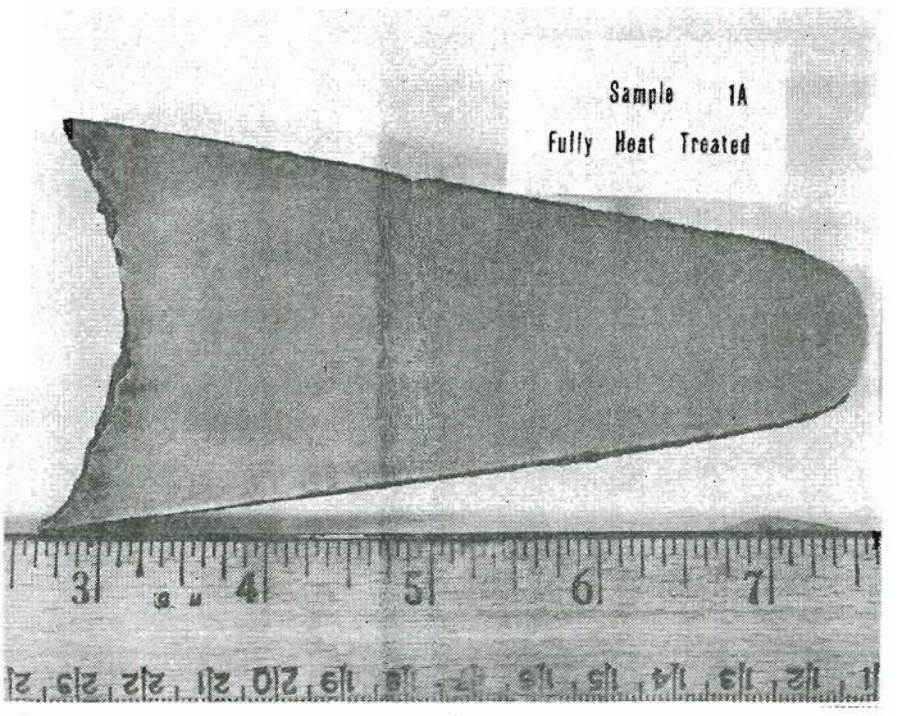

Fig.#41 Etched vertical slab. 0.9X
Vilella's

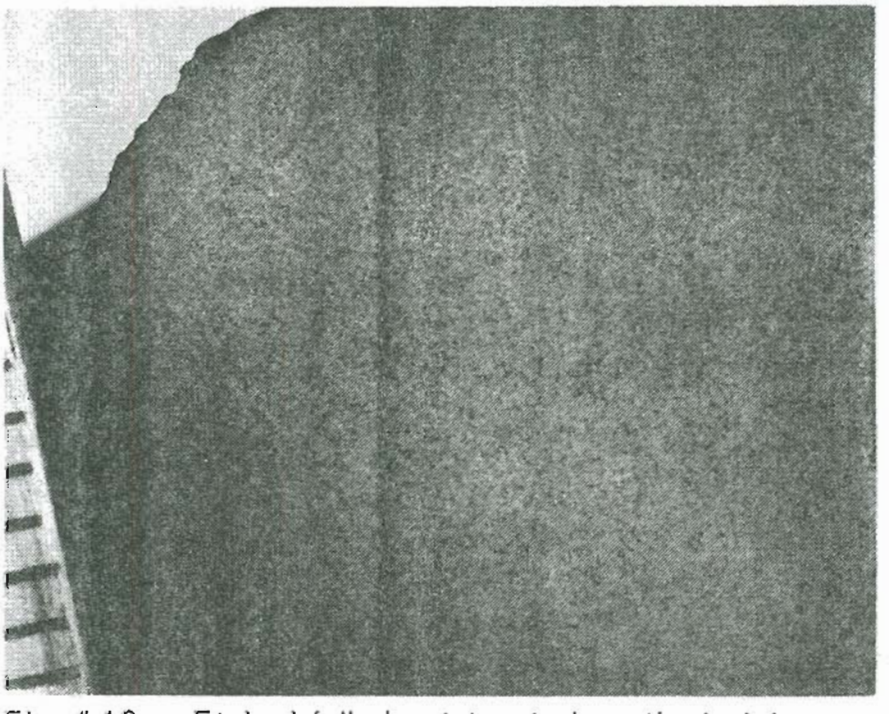

Fig.#42 Etched fully heat treated vertical slab.
Group I-A. Vilella's 4X

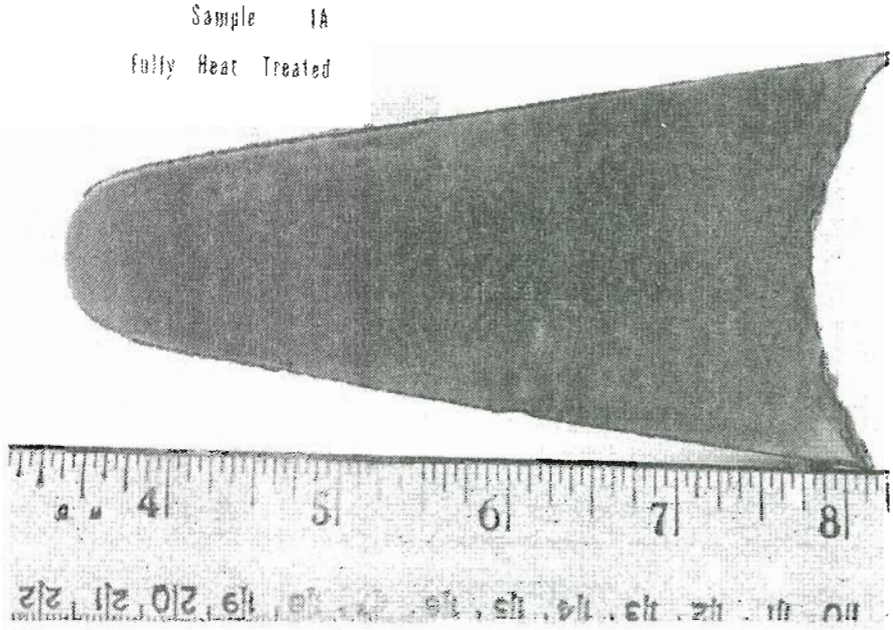

Fig.#43 Etched vertical slab. 0.85X
Steads

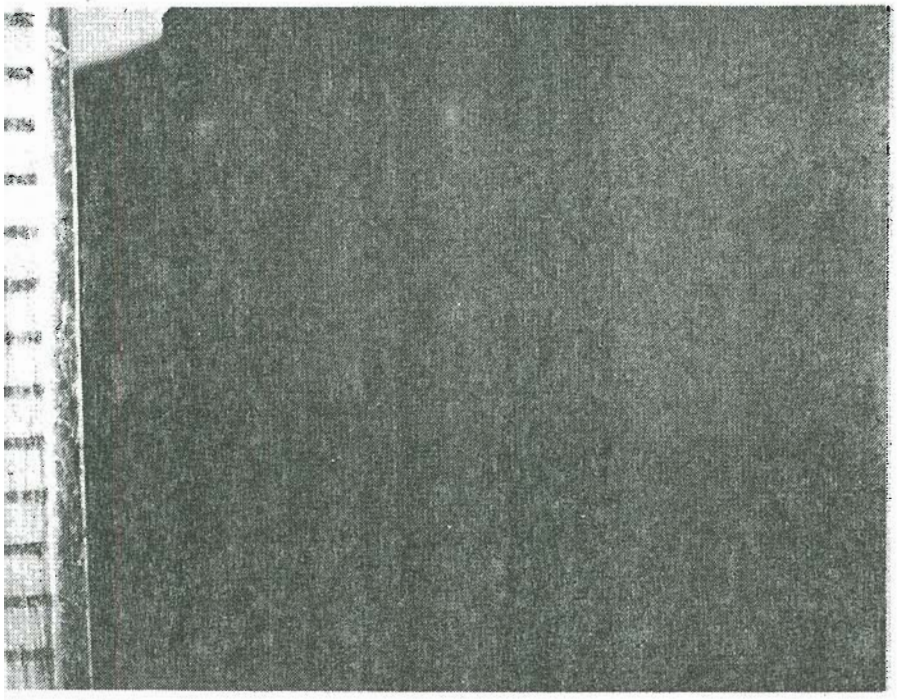

Fig.#44 Etched fully heat treated vertical slab.
Group 1-A. Steads 4X

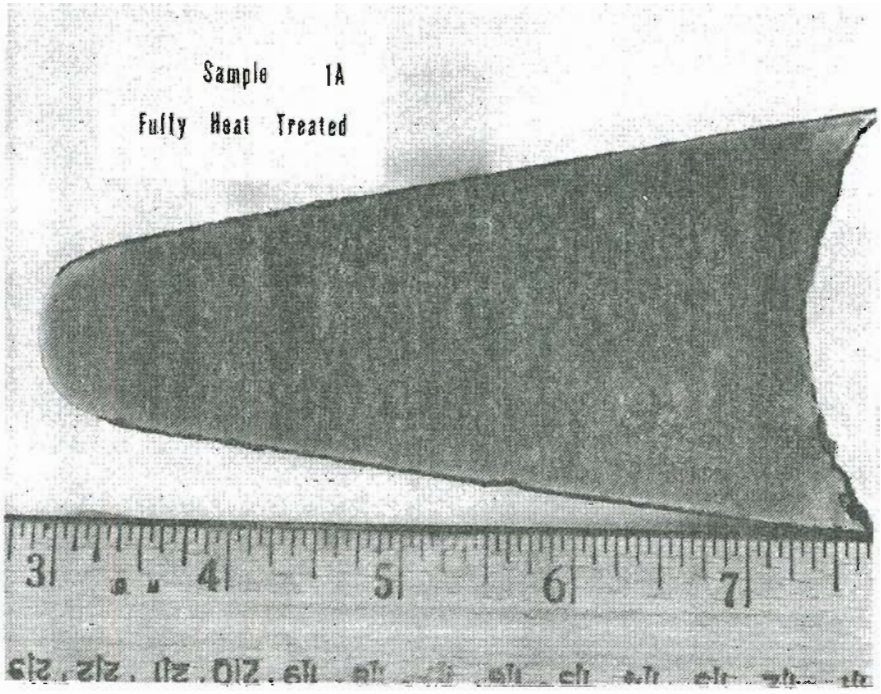

Fig.#45 Etched vertical slab. 0.9X
Aqua regia

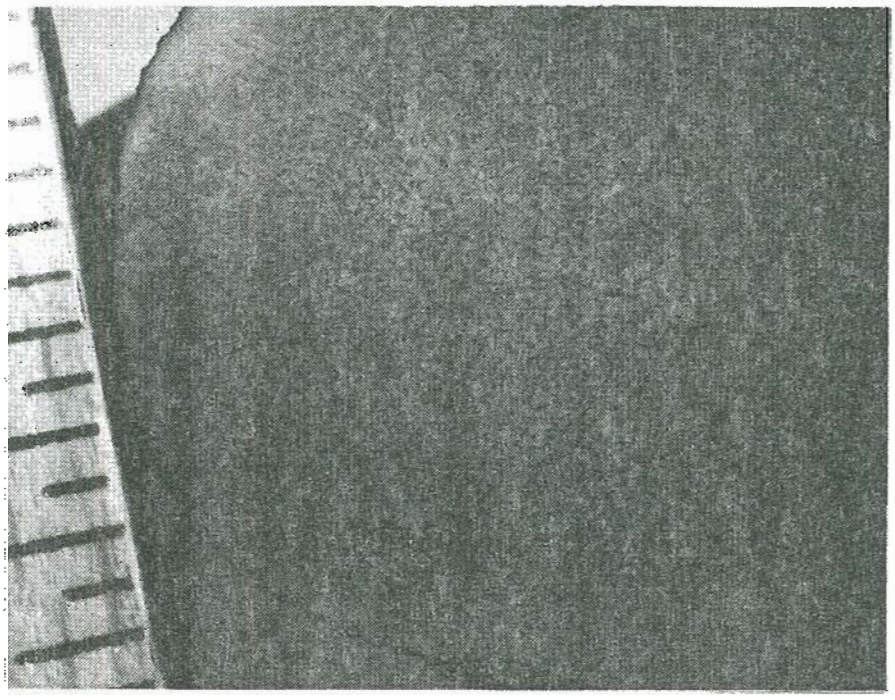

Fig.#46 Etched fully heat treated vertical slab.
Group I-A. Aqua regia 4X

Group #I

Group #II

Group #III

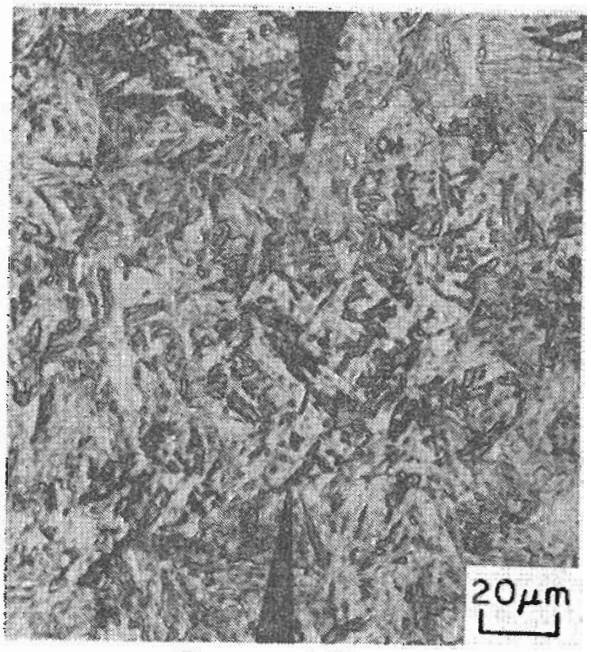

Group #IV

Figure #47 Tempered martensitic microstructure after heat treatment "A" 500X Vilella's

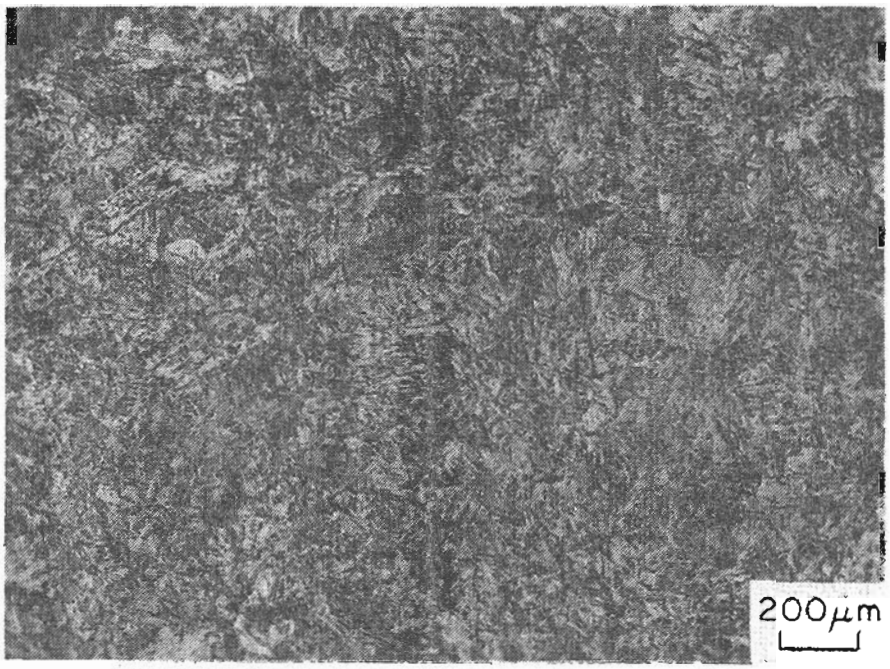

Fig.#48 Group I-B Heat treated to condition "A".
Vilella's 50X

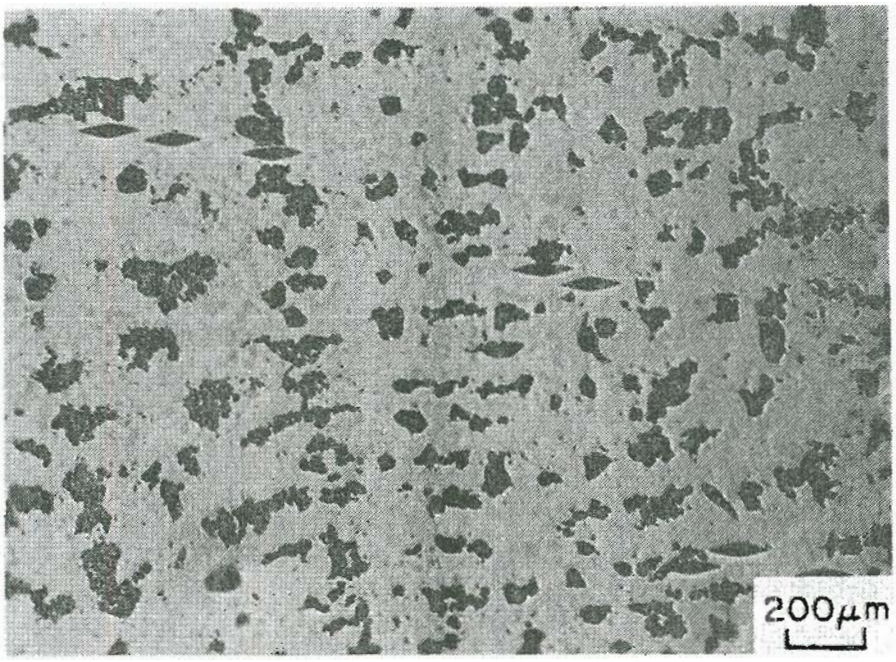

Fig.#49 Group I-B Same location and heat treatment as Fig.#48.
DA (dark etching) and IDA (light etching) regions. Steads 50X

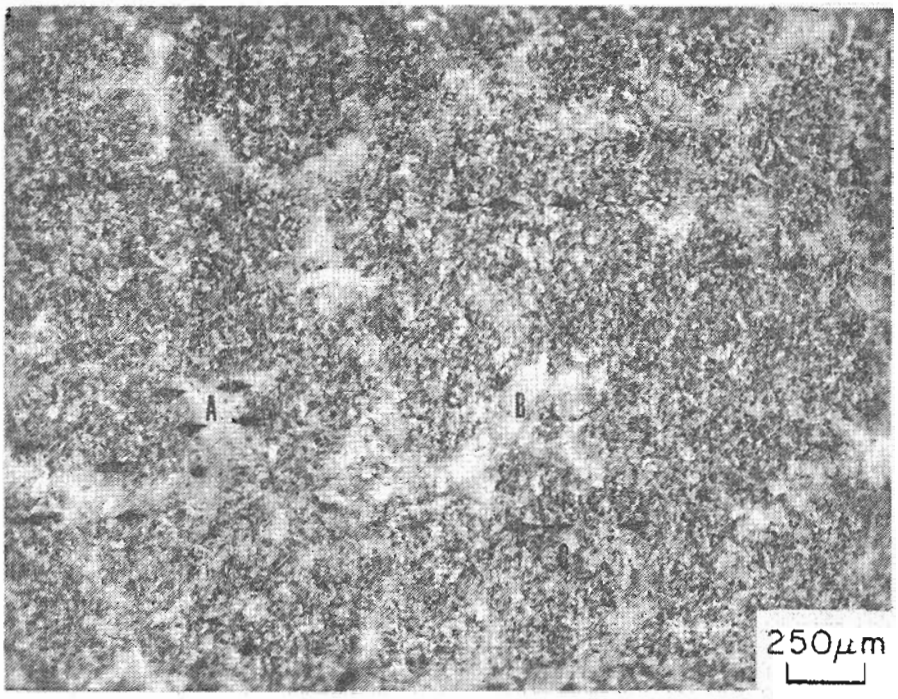

Fig.#50 Group IV-A Heat treated to condition "A".
Vilella's 40X

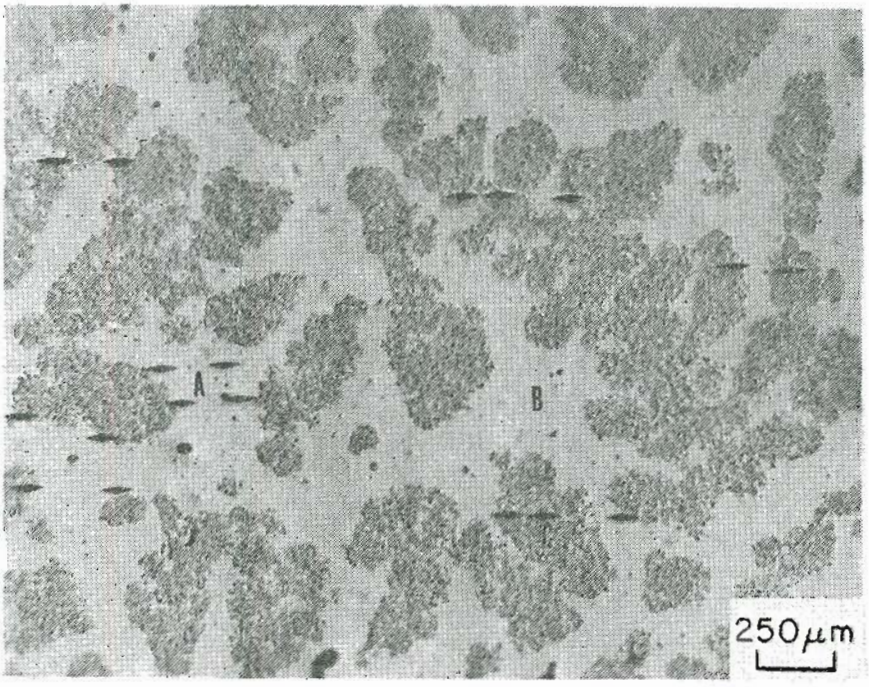

Fig.#51 Group IV-A Same location and heat treatment as Fig.#50. DA (dark etching) and IDA (light etching) regions.
Steads 40X

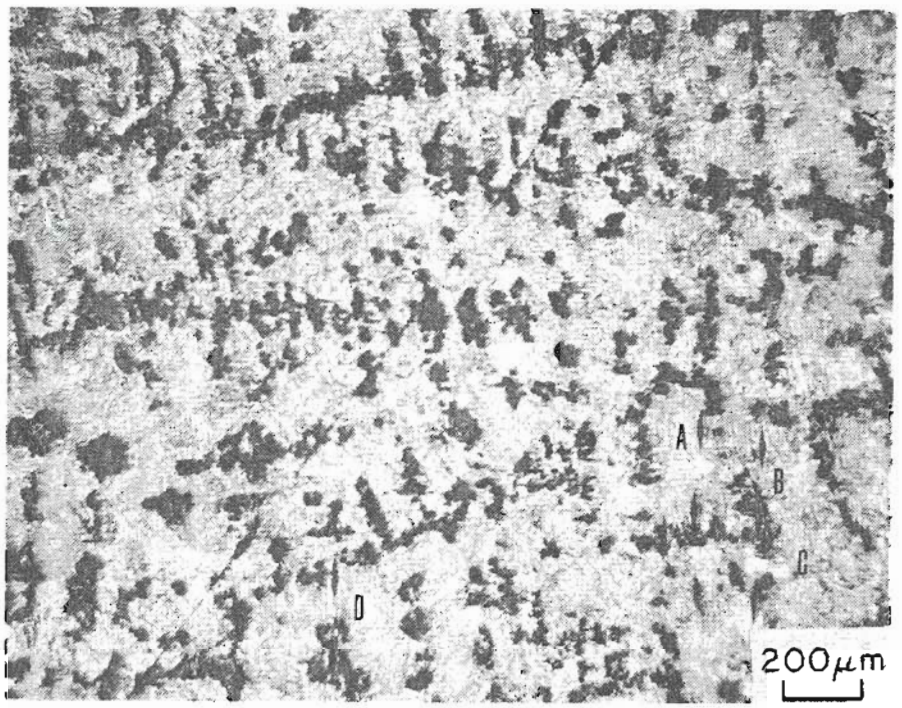

Fig.#52 Group I-D, 6. Steads/Vilella's 50X

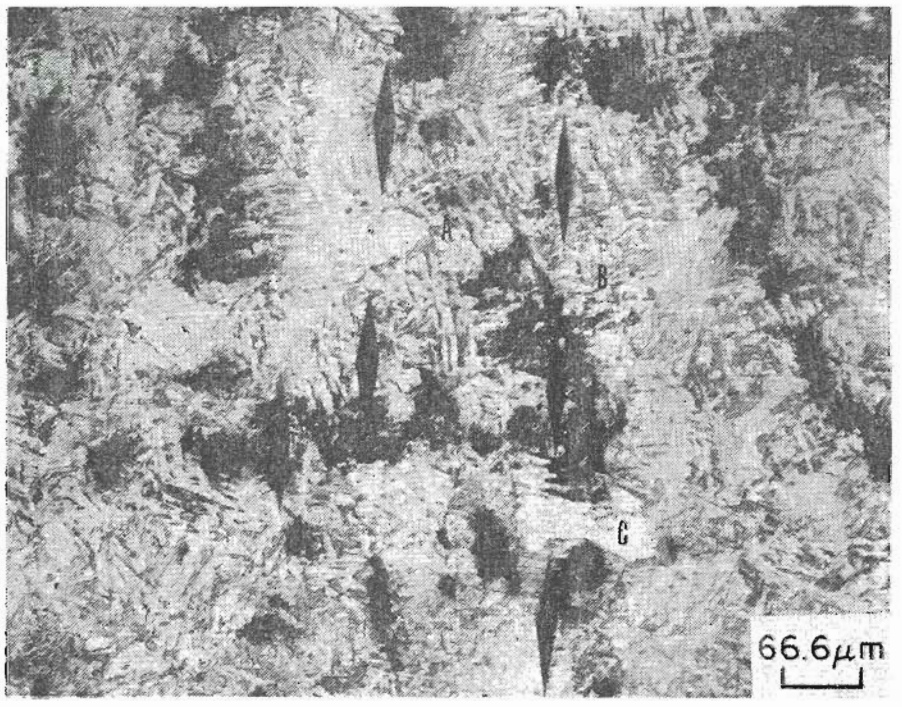

Fig.#53 Note visible grain boundries in I.D.A. regions.
Group I-D, 6. Steads/Vilella's 150X

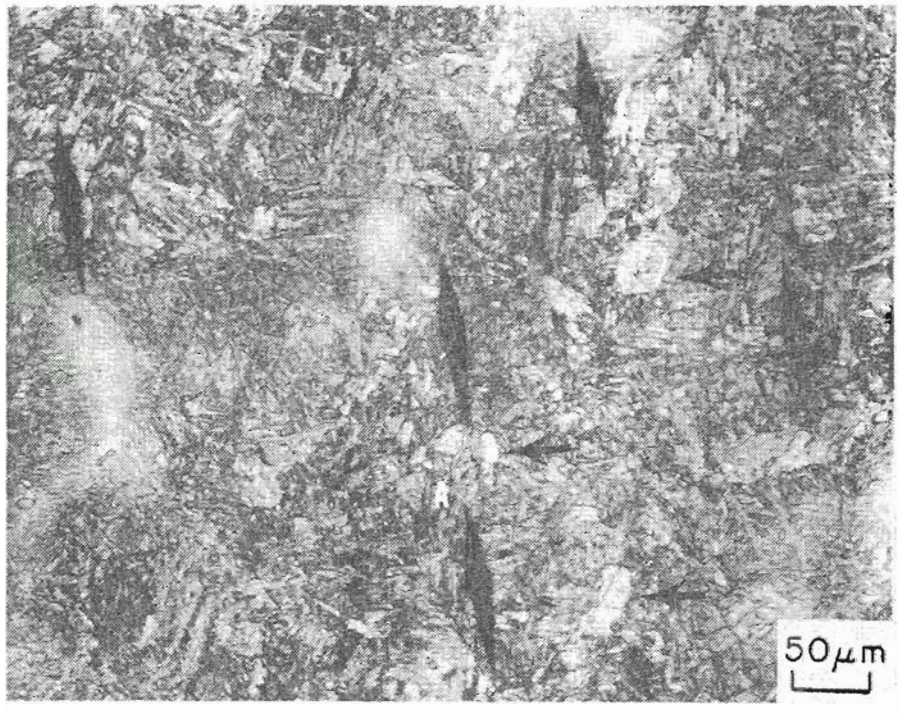

Fig.#54 Group III-A, 1. Vilella's 200X

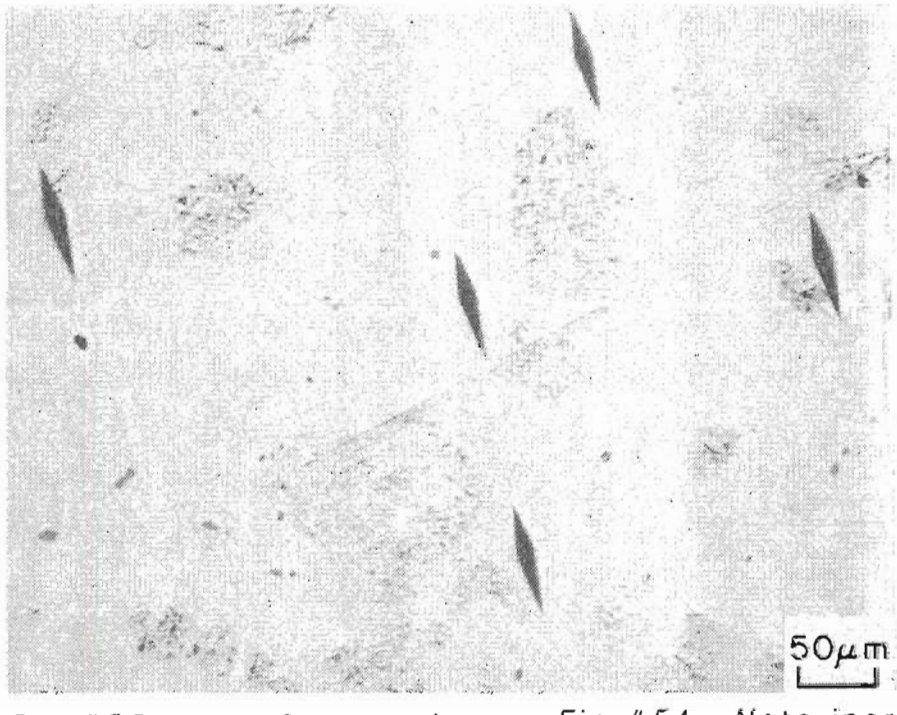

Fig.#55 Same region as Fig.#54 Note increased grain boundary visibility in IDA regions Group III-A, 1. Steads 200X

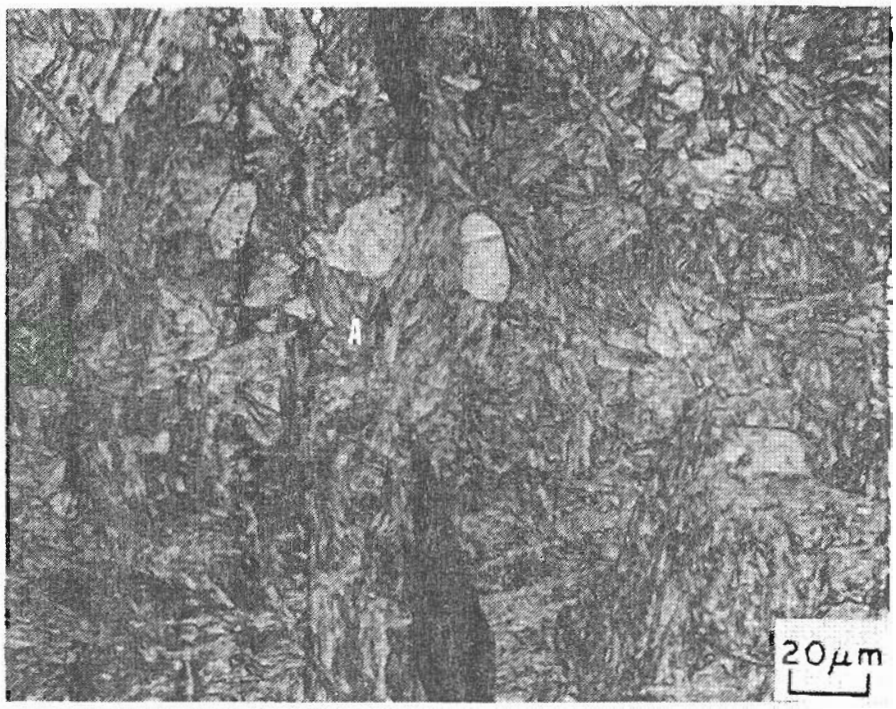

Fig.#56 Higher magnification of area A from Fig.#54
Group III-A, 1. Vilella's 500X

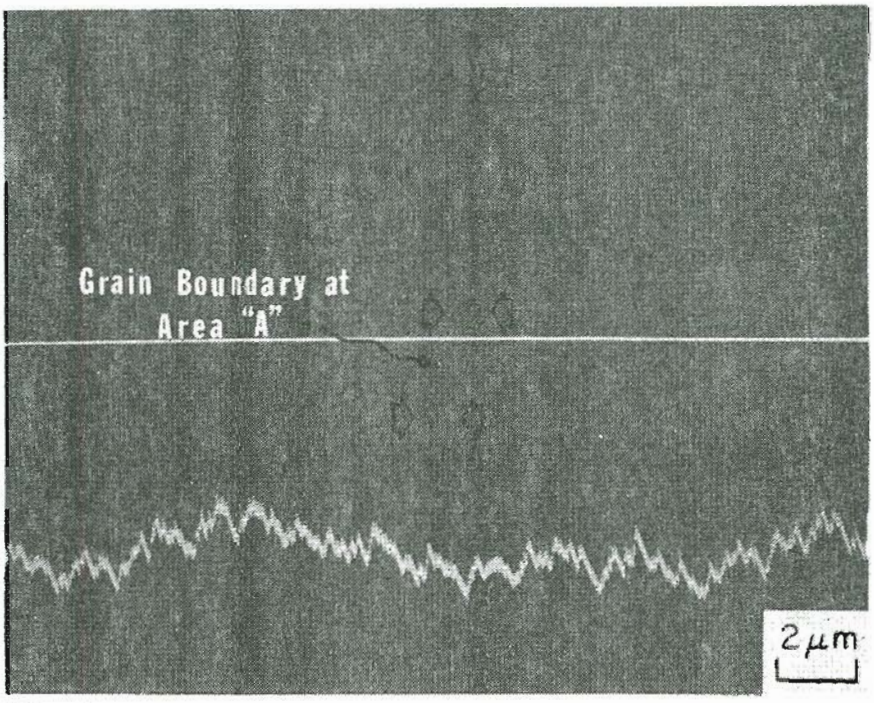

Fig.#57 Cr line scan across grain boundry at area A.
Group III-A, 1. unetched 5000X

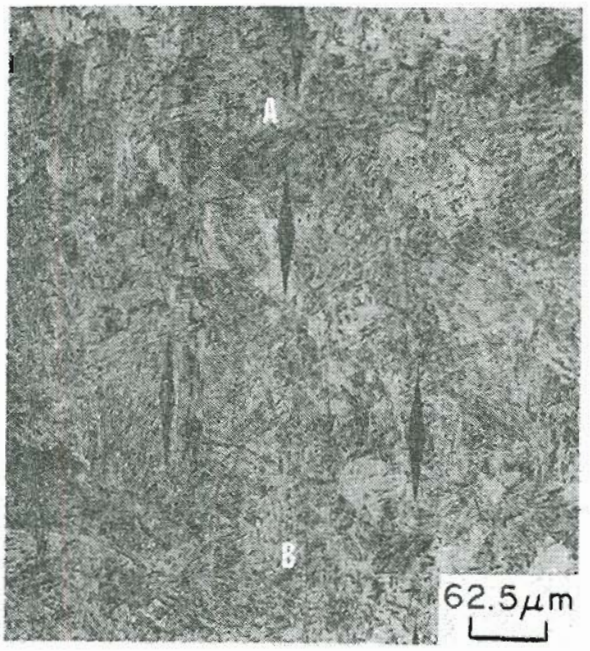

160X

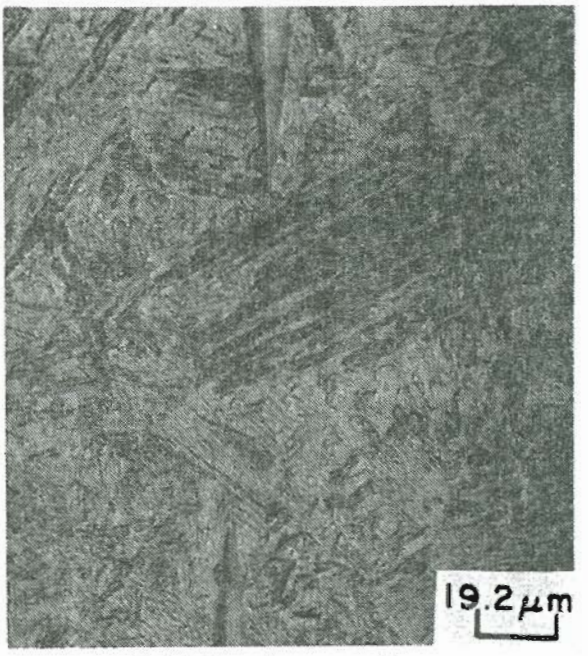

520X Area A

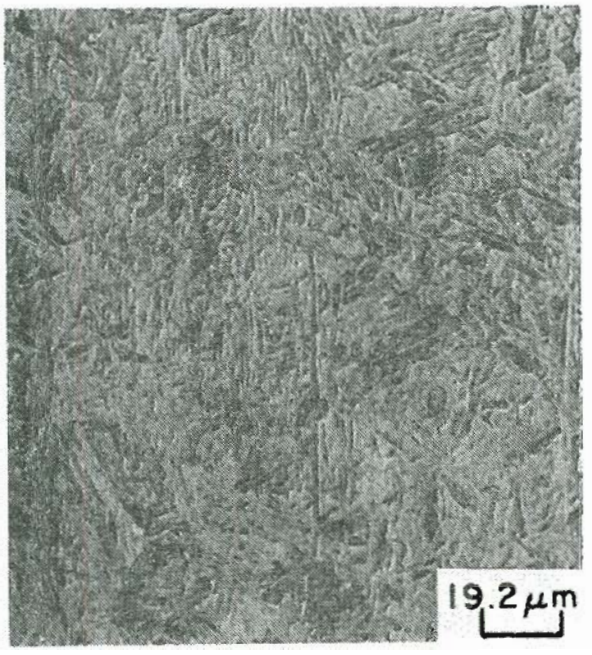

520X Area B

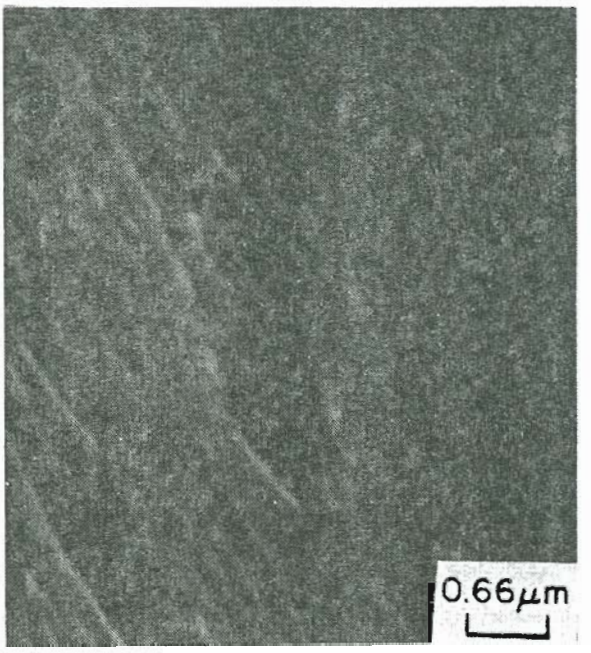

15,000X

Area A viewed with the SEM

Fig.#58 Group I, heat treatment 'C'.
Martensitic microstructure.

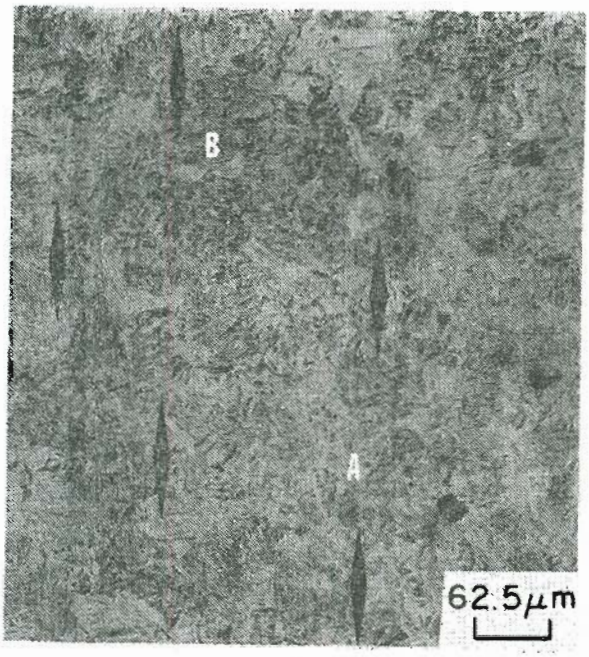

160X

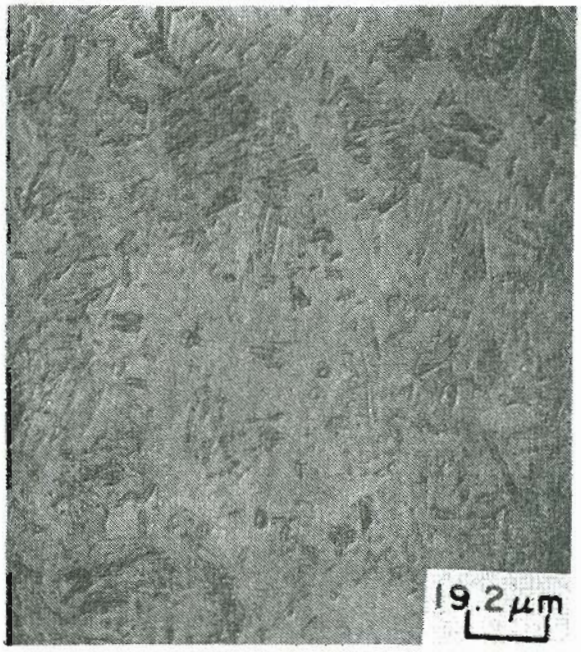

520X Area A

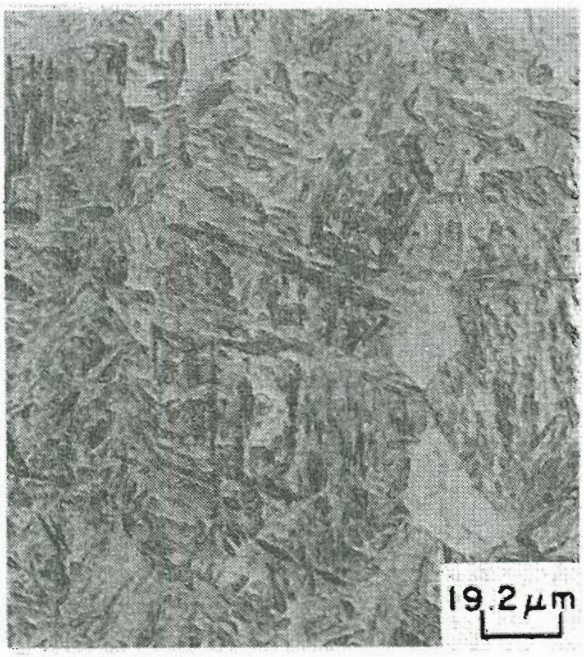

520X Area B

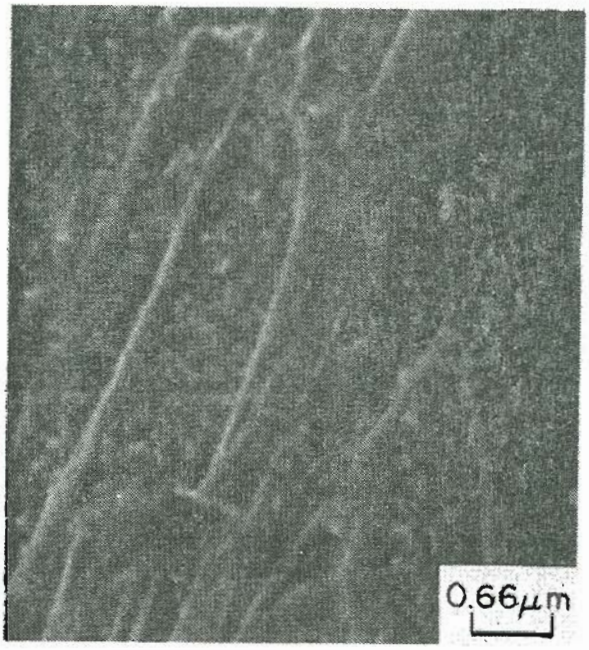

15,000X
Area B viewed with the SEM.

Fig.#59 Group IV, heat treatment "C". Compare to Fig.#58
No appearent change in martensitic microstructure.

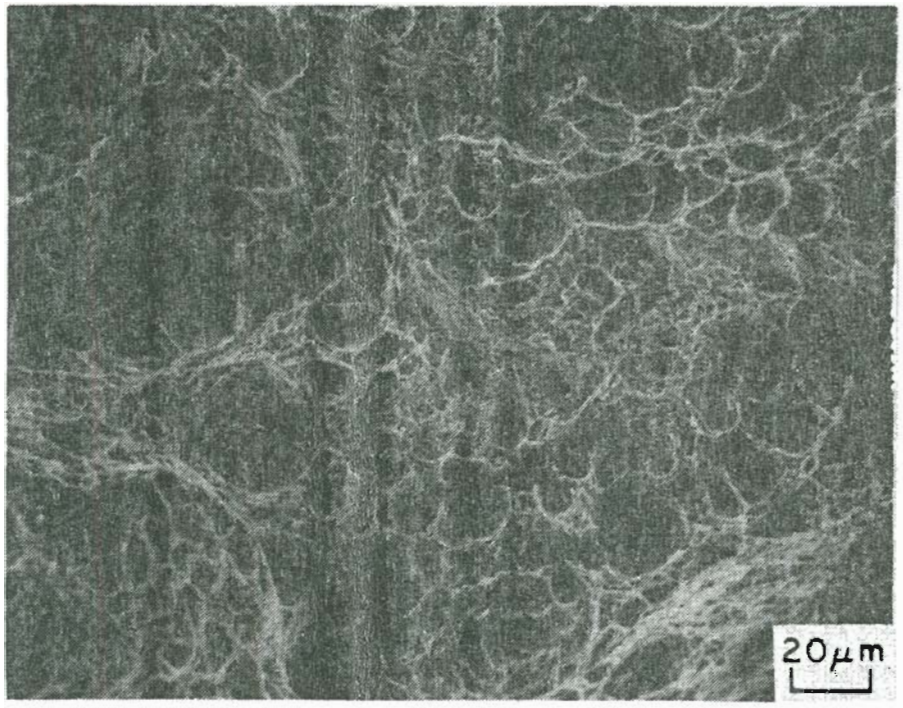

Fig.#60 Group I-D, 6-A. 212F 500X

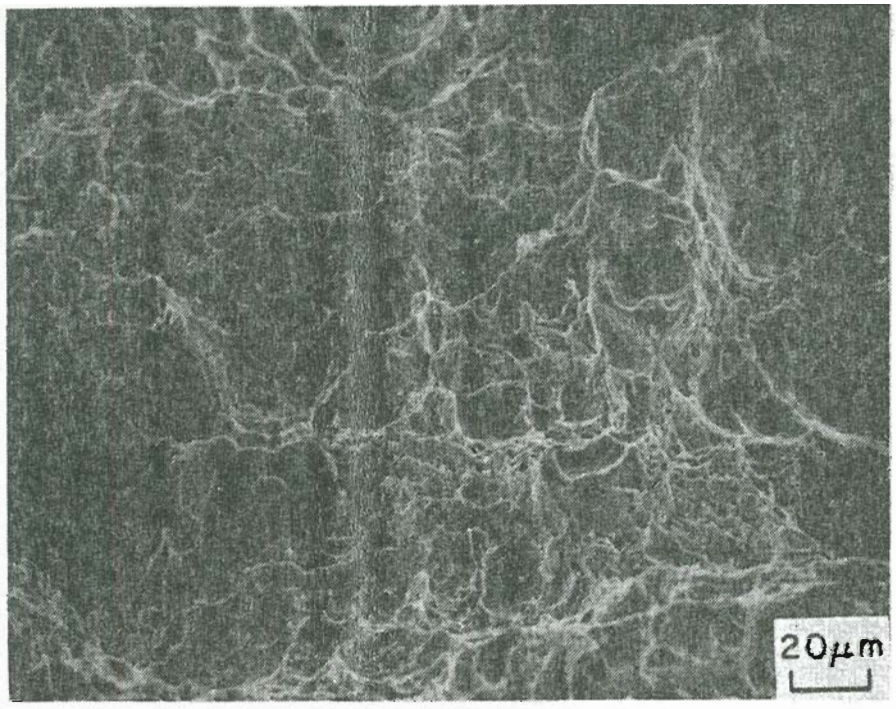

Fig.#61 Group I-D, 6-B. 212F 500X

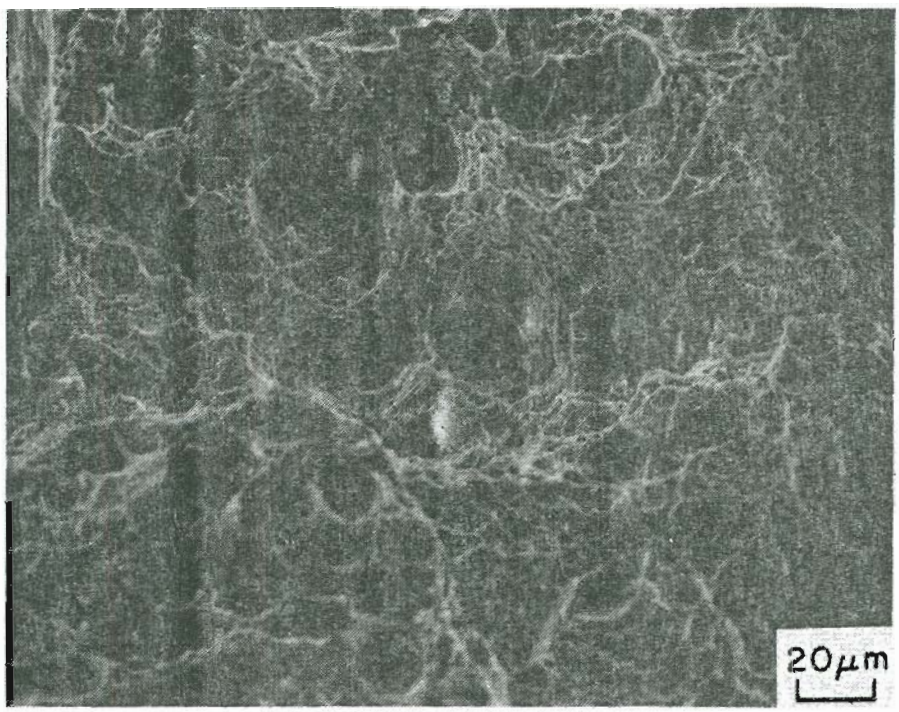

Fig.#62 Group I-C, 7-C. Room 500X

Fig.#63 Group I-C, 7-B. Room. 500X

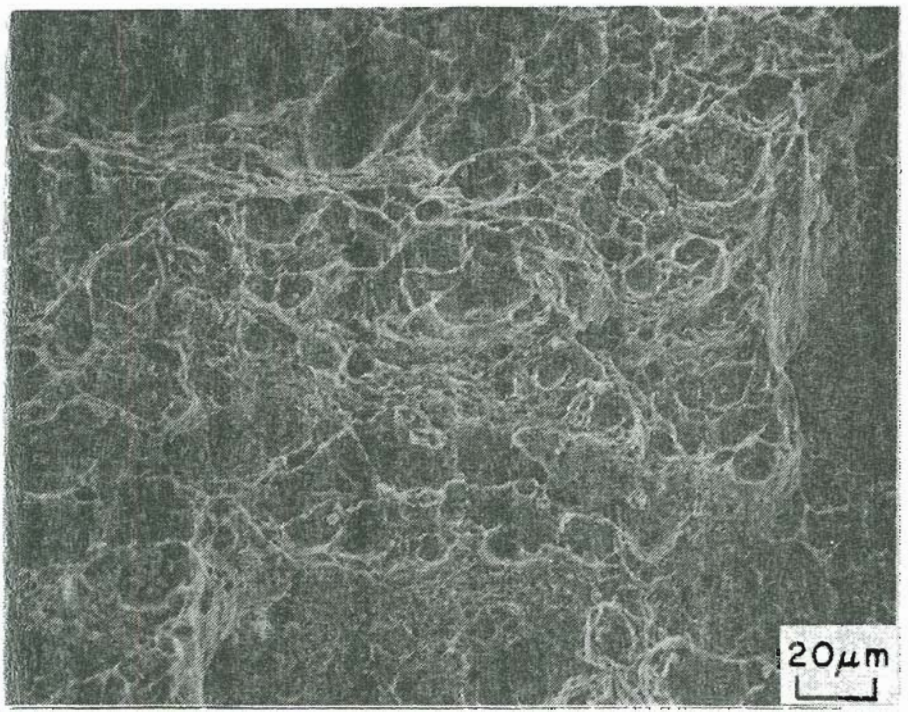

Fig.#64 Group I-B, 8-D. -40F 500X

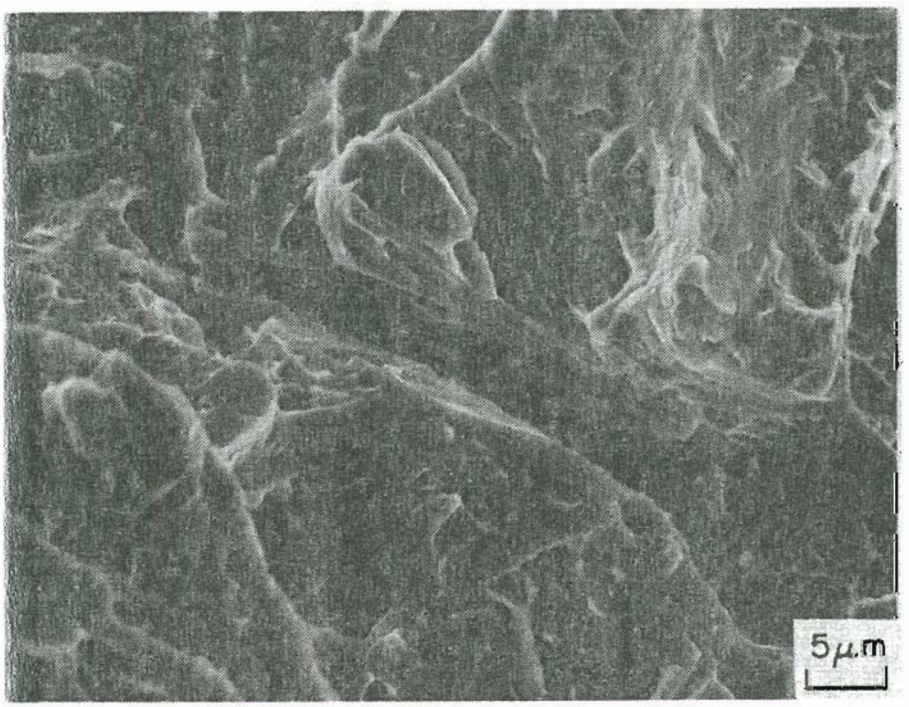

Fig.#65 Group I-B, 8-A, a. -40F 2000X

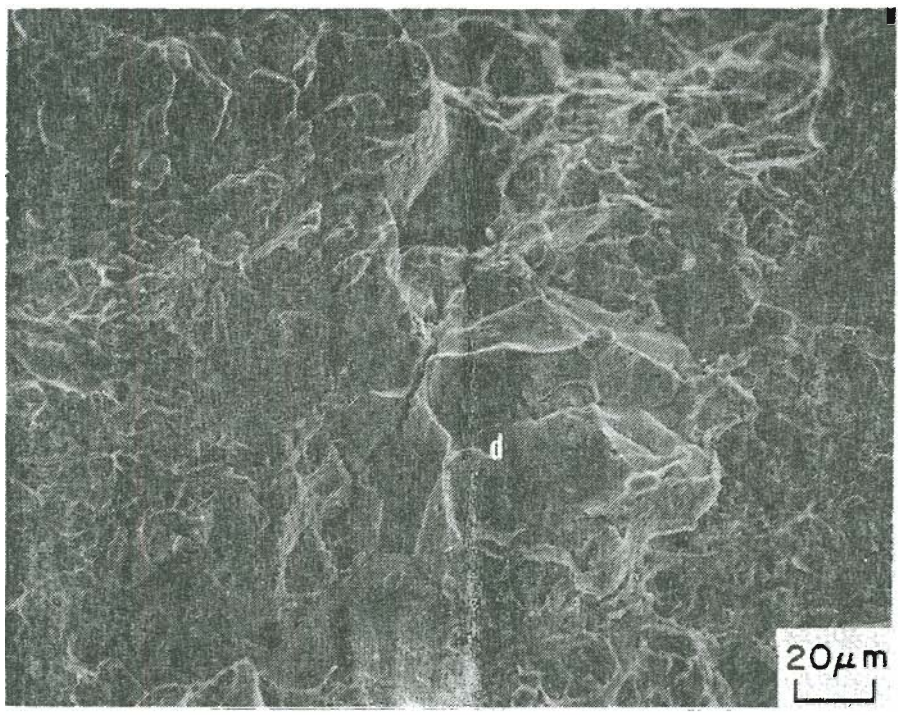

Fig.#66 Group I-E, 2-D. -140F 500X

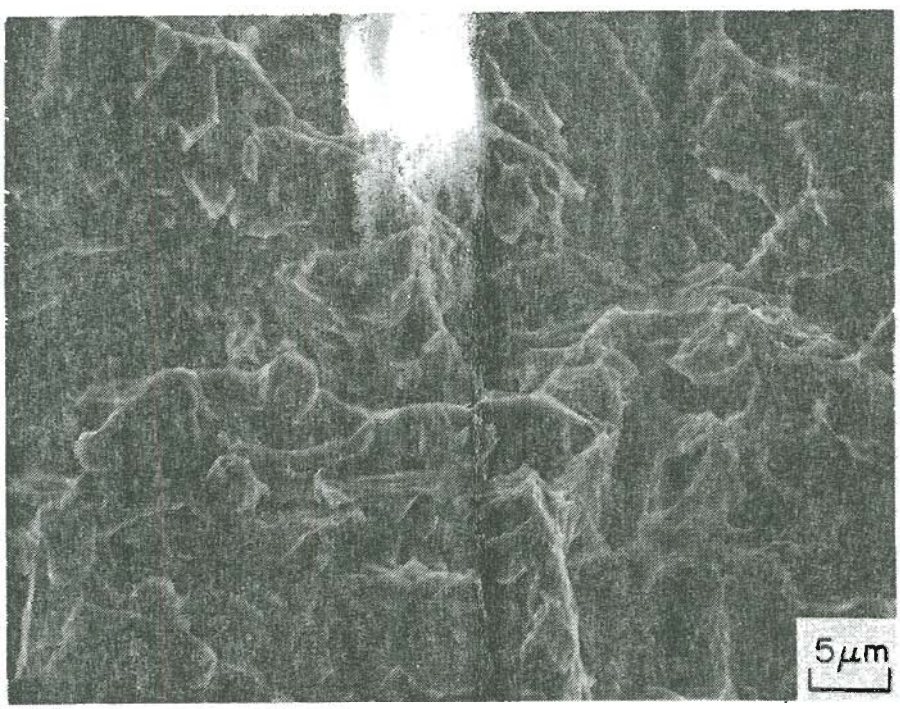

Fig.#67 Group I-B, 2-C. -140F 2000X

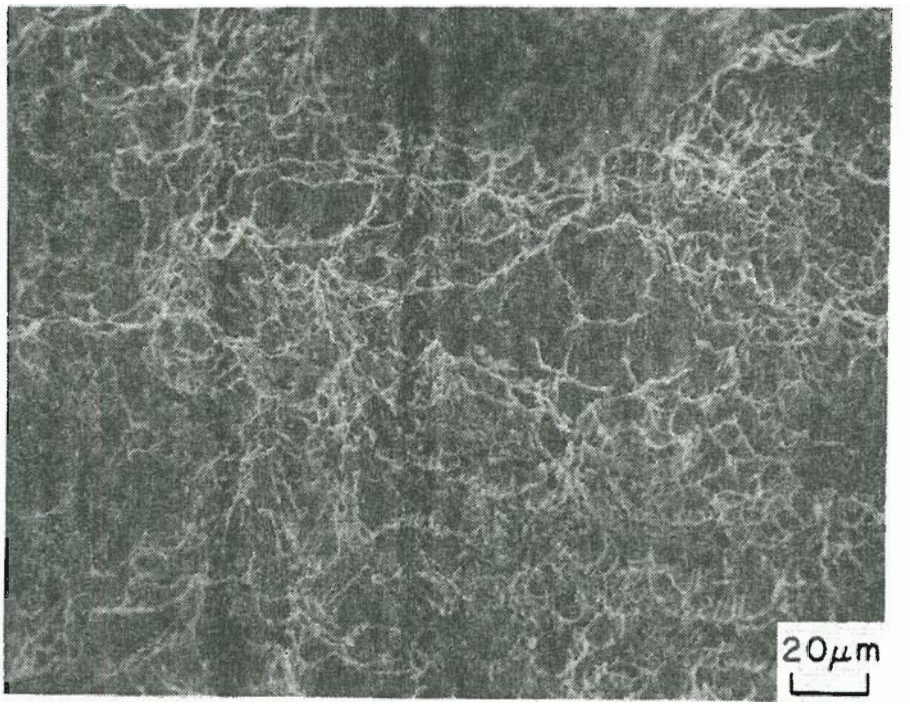

Fig.#68 Group II-D, 7-B. 212F 500X

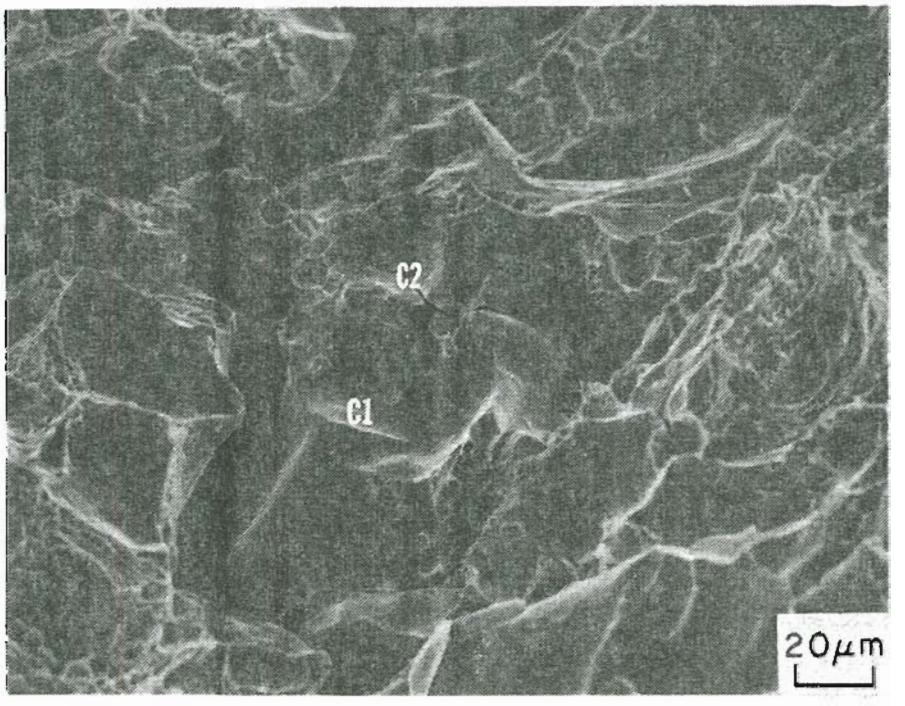

Fig.#69 Group II-D, 7-C. 212F 500X

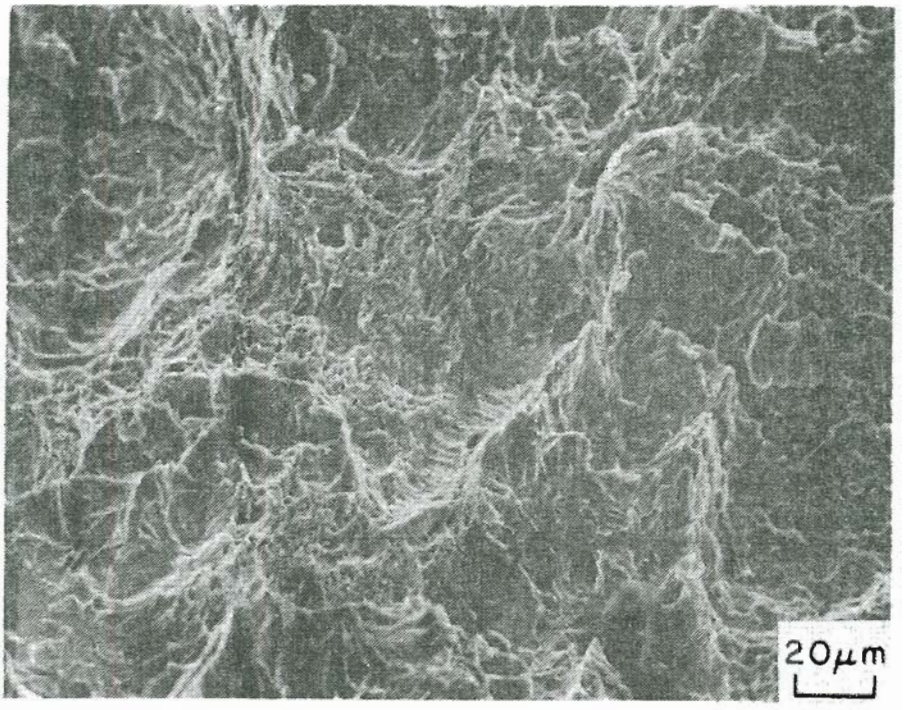

Fig.#70 Group II-B, 7-B. -40F 500X

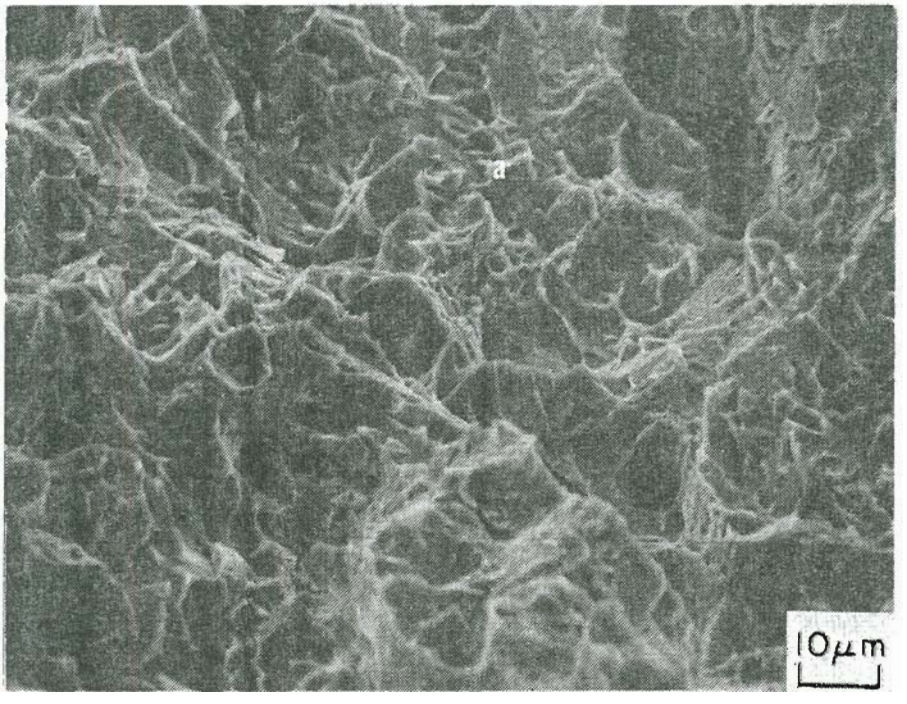

Fig.#71 Group II-B, 7-A. -40F 1000X

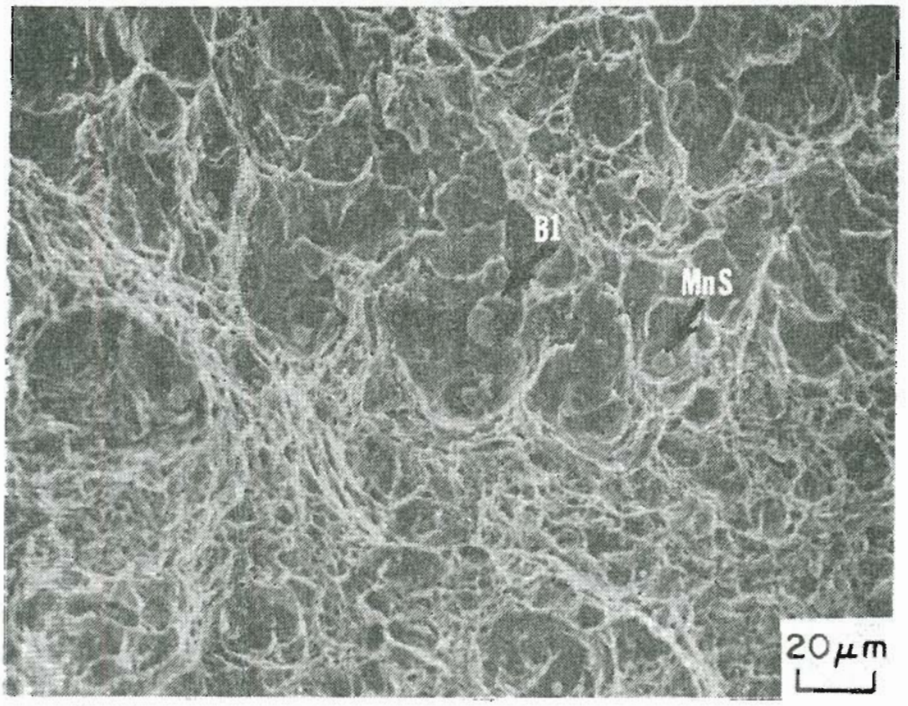

Fig.#72 Group II-C, 7-B. Room 500X

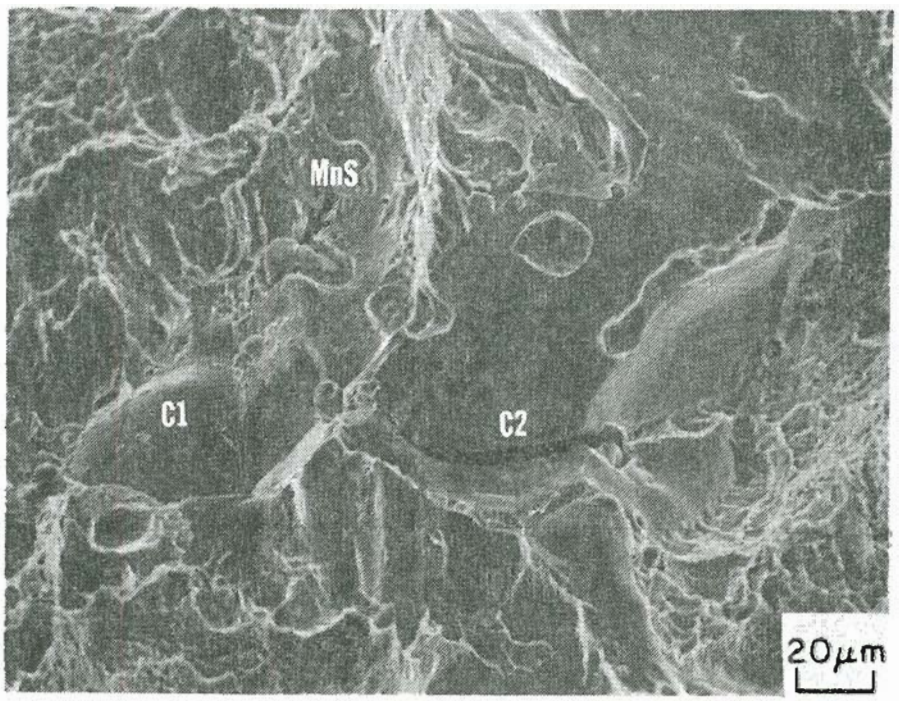

Fig.#73 Group II-C, 7-C. Room 500X

Fig.#74 Group II-B, 1-D. -140F 200X

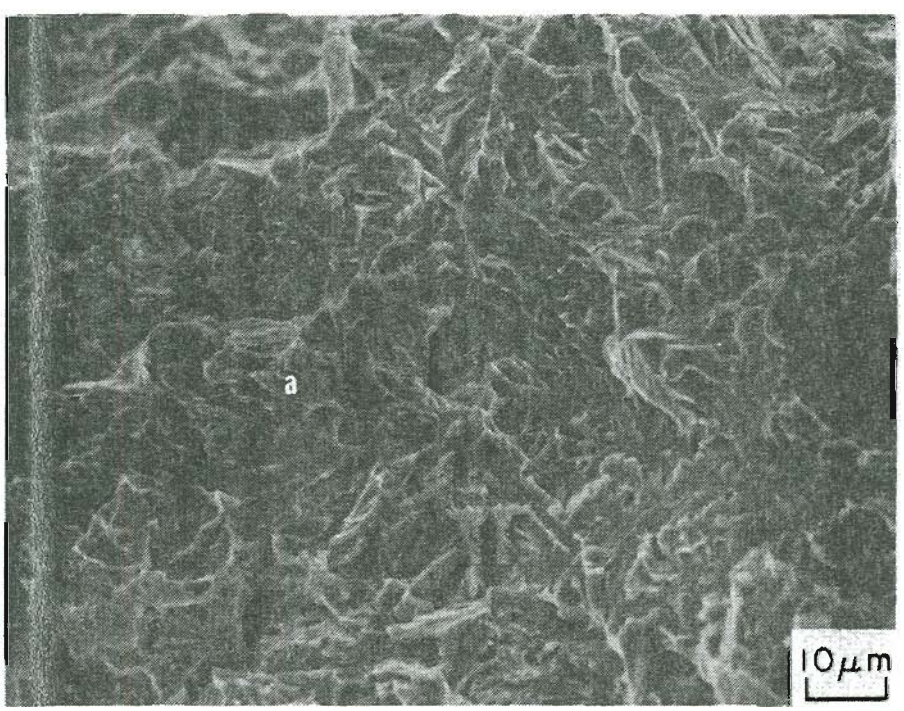

Fig.#75 Group II-B, 1-A. -140F 1000X

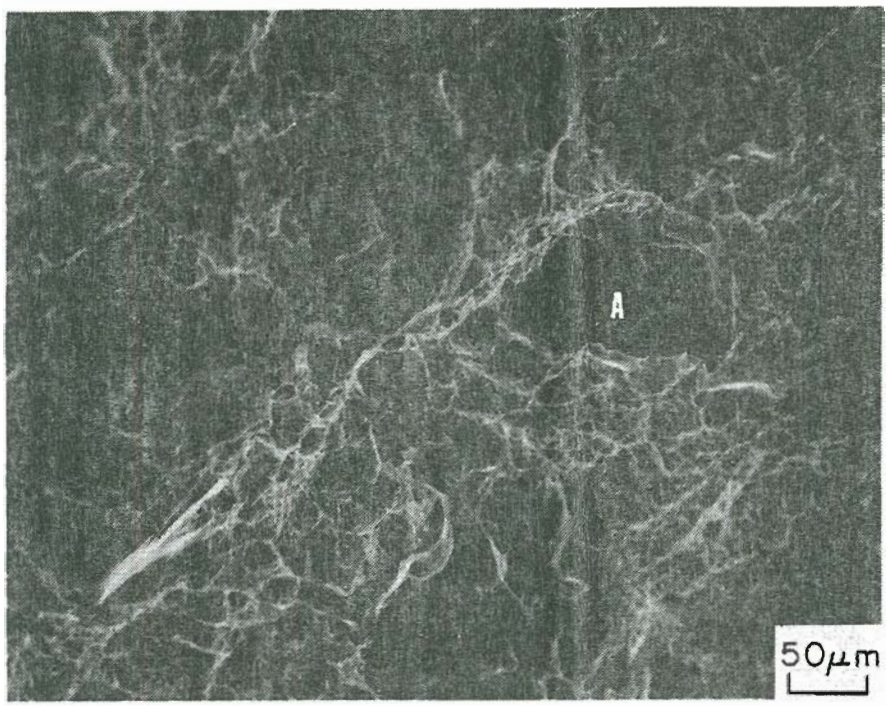

Fig.#76 Group III-C, 5-A. 212F 200X

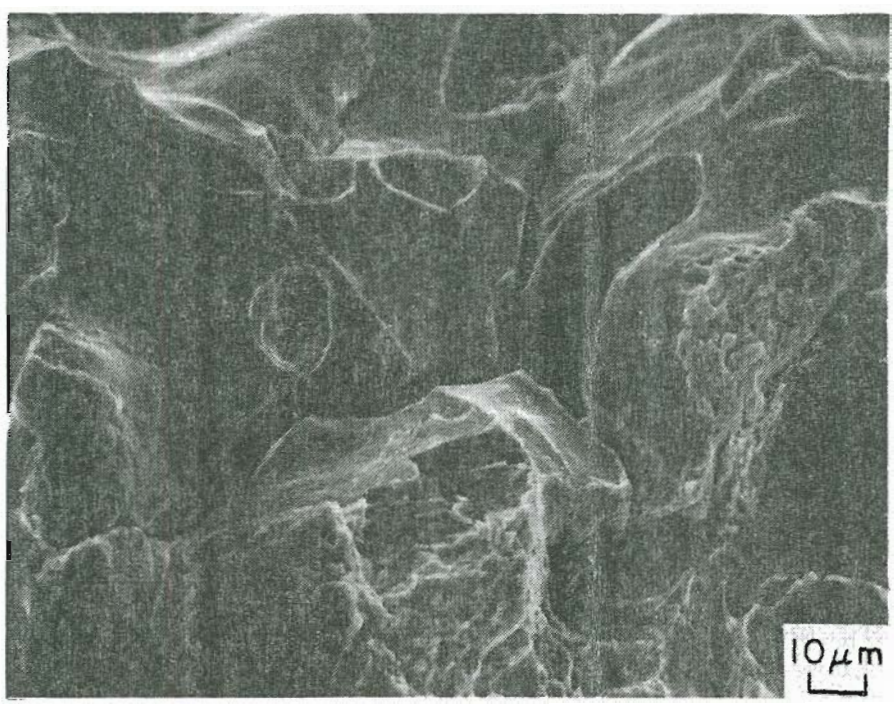

Fig.#77 Group III-C, 2-A. 212F 1000X

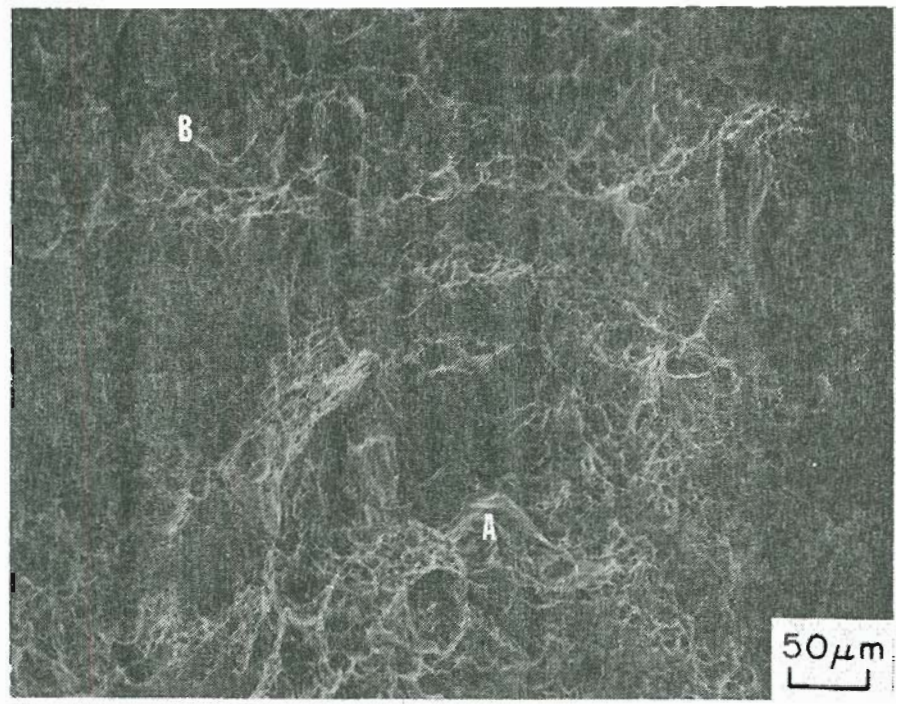

Fig.#78 Group III-B, 6-A. Room 200X

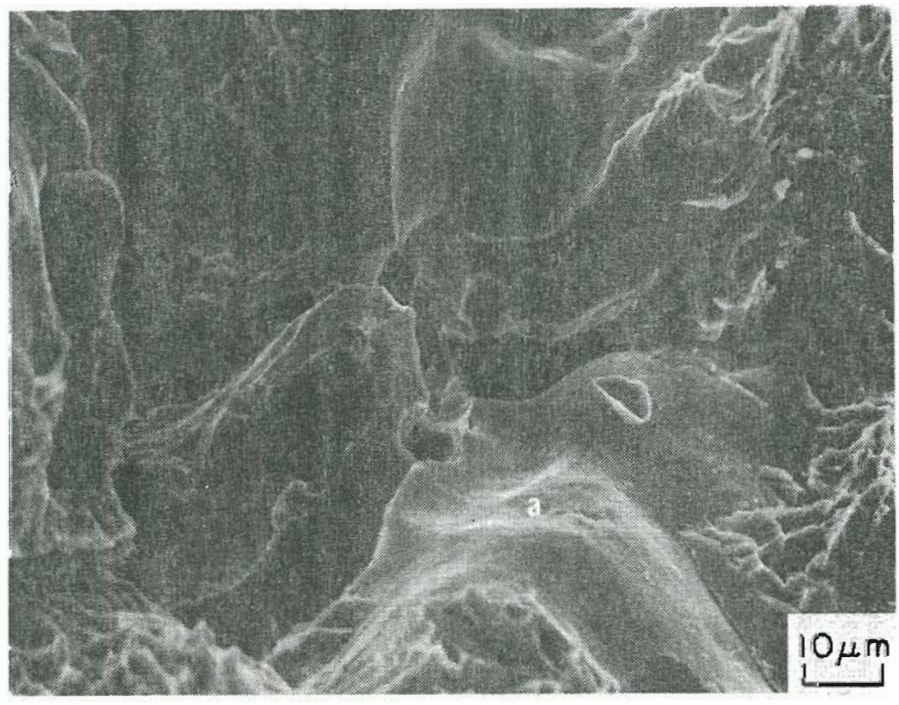

Fig.#79 Group III-B, 6-A. Room 1000X

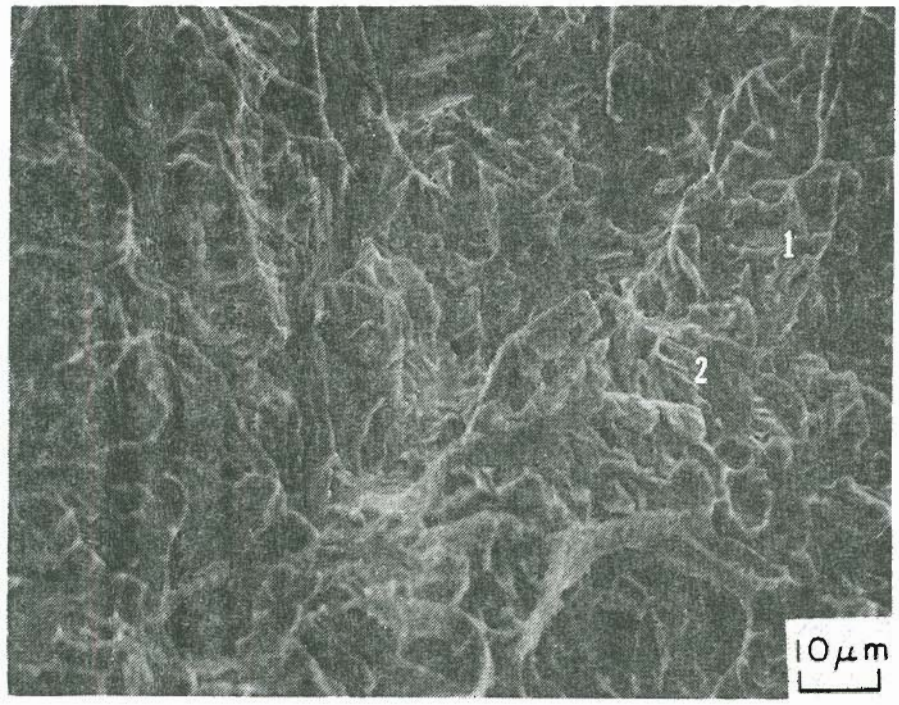

Fig.#80 Group III-A, 7-D, b. -40F 1000X

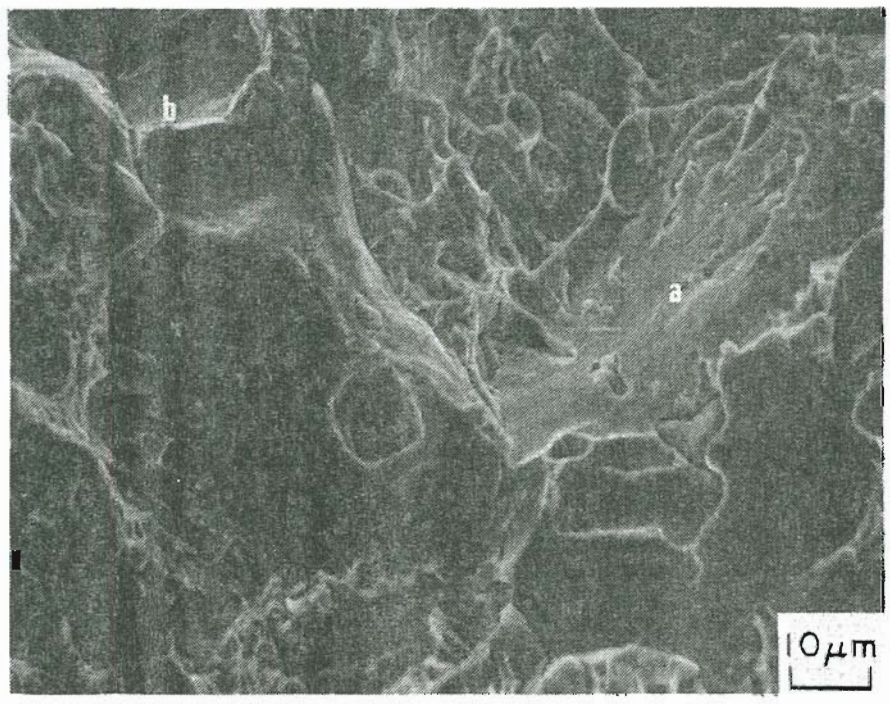

Fig.#81 Group III-A, 7-B, b. -40F 1000X

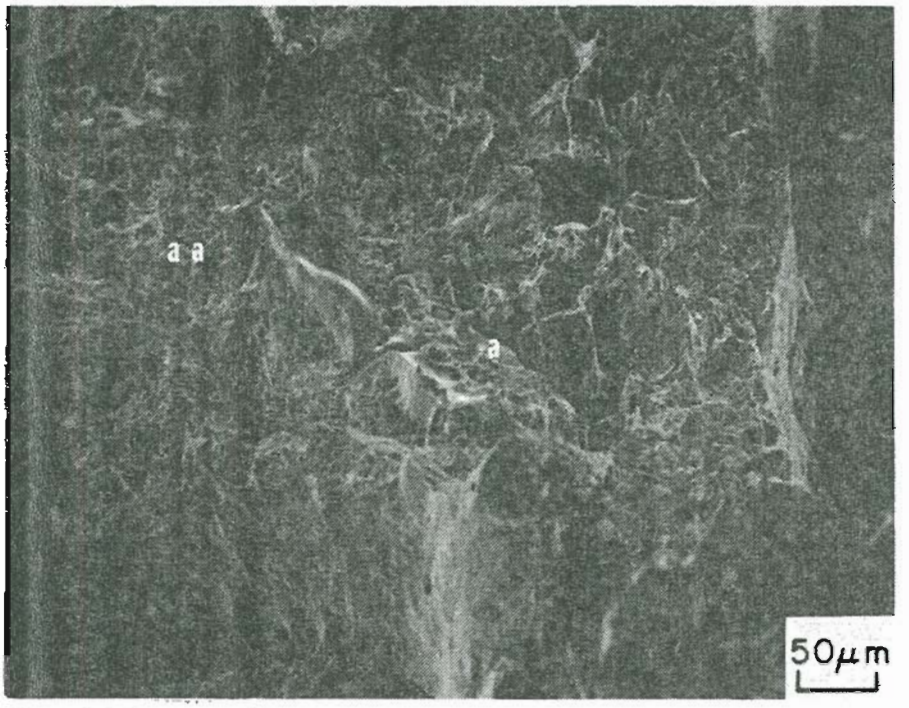

Fig.#82 Group III-A, 1-A. -140F 200X

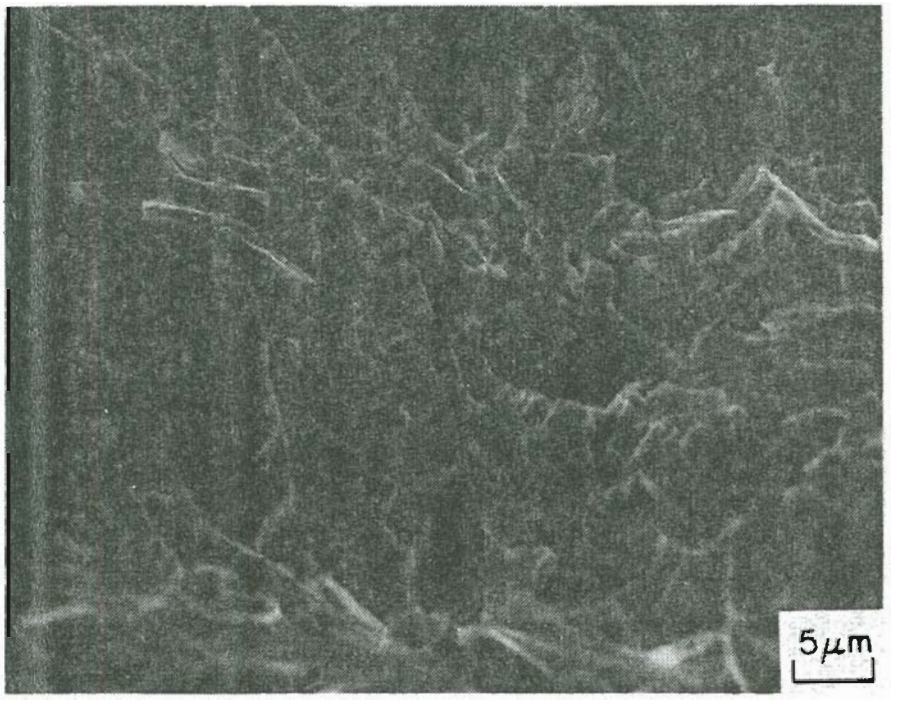

Fig.#83 Group III-A, 1-aa. -140F 2000X

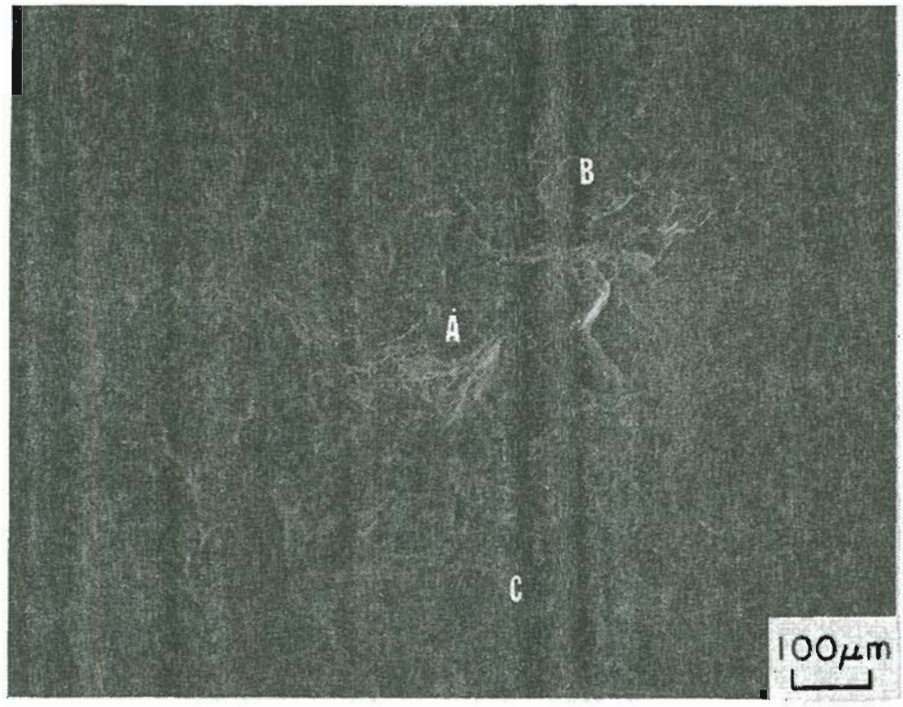

Fig.#84 Group IV-C, 2-F. 212F 100X

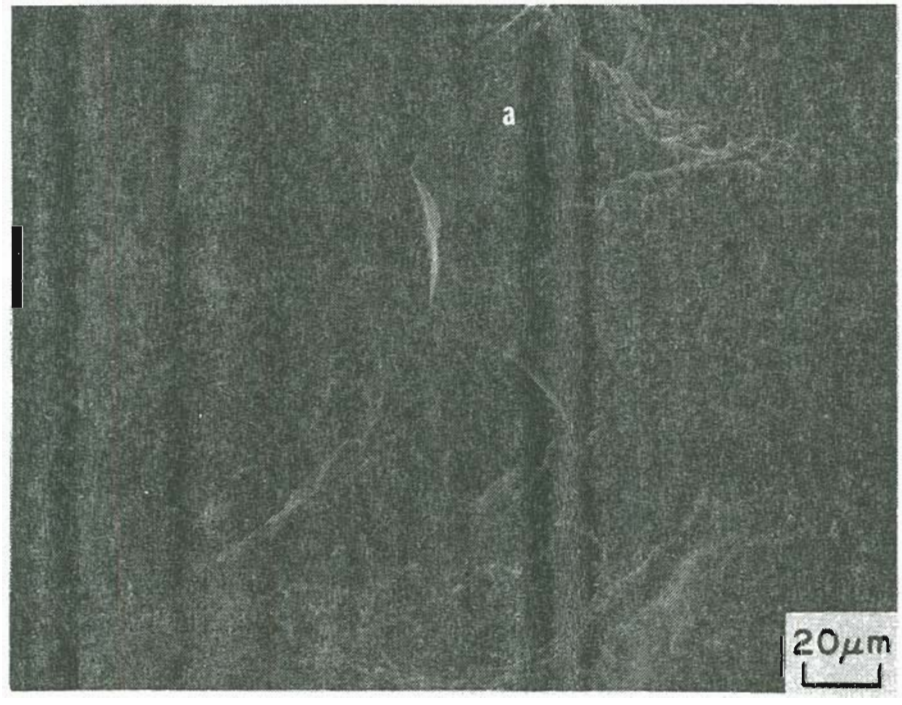

Fig.#85 Group IV-C, 2-F, A-a. 212F 500X

Fig.#86 Group IV-D, 4-A, A-aa. Room 500X

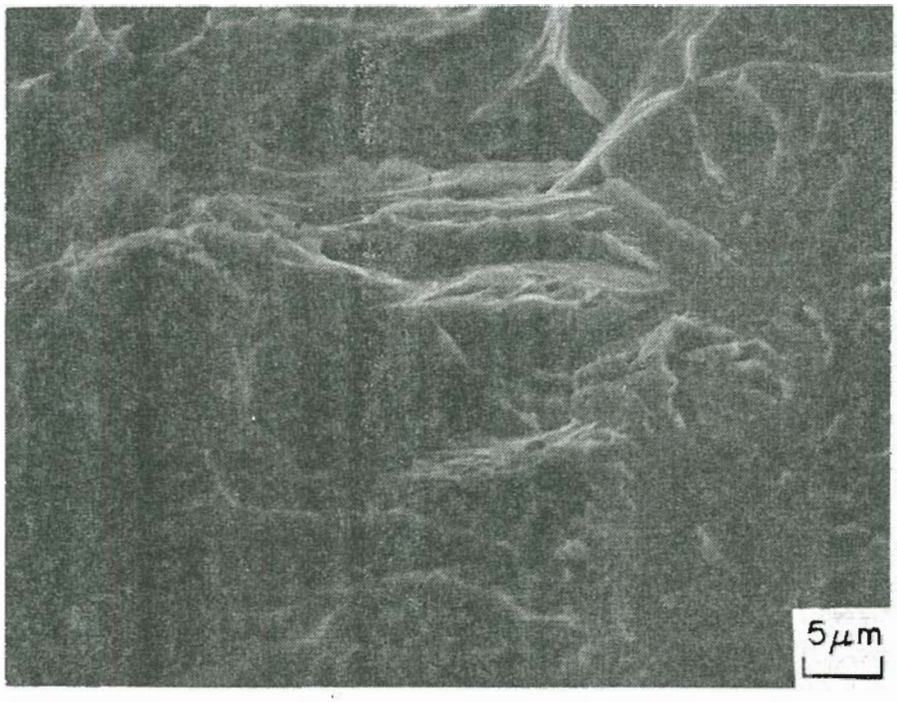

Fig.#87 Group IV-D, 4-C, C-c. Room 2000X

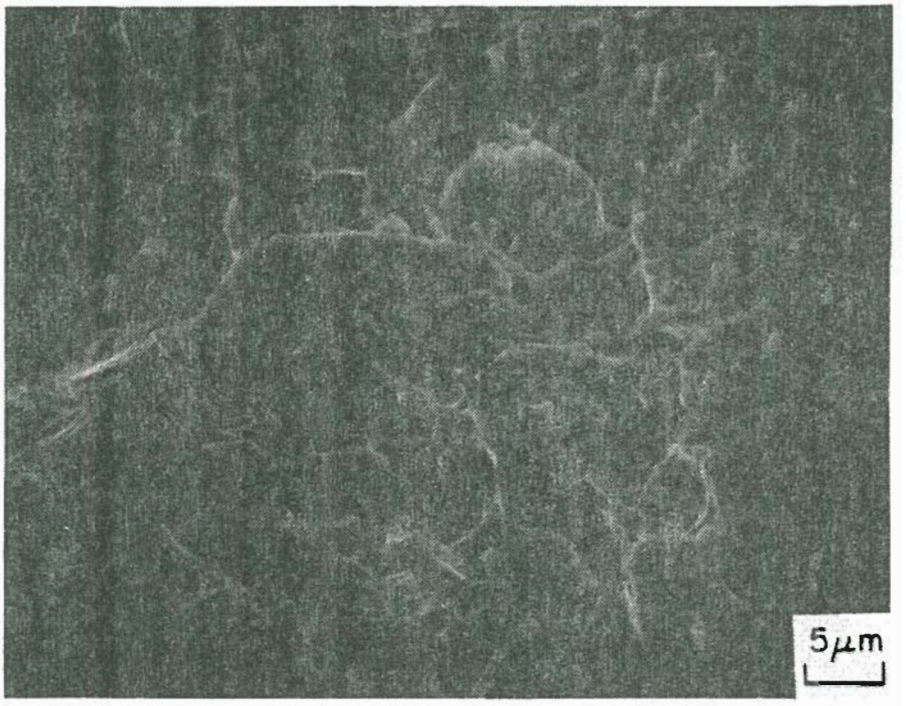

Fig.#88 Group IV-C, 2-B, A. -40F 2000X

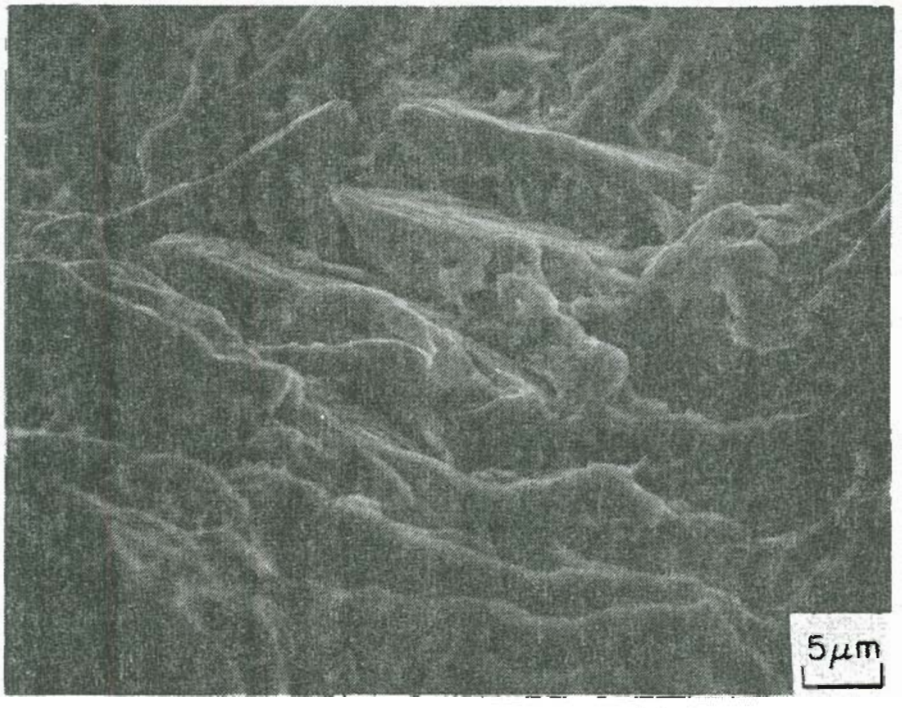

Fig.#89 Group IV-C, 2-C, a. -40F 2000X

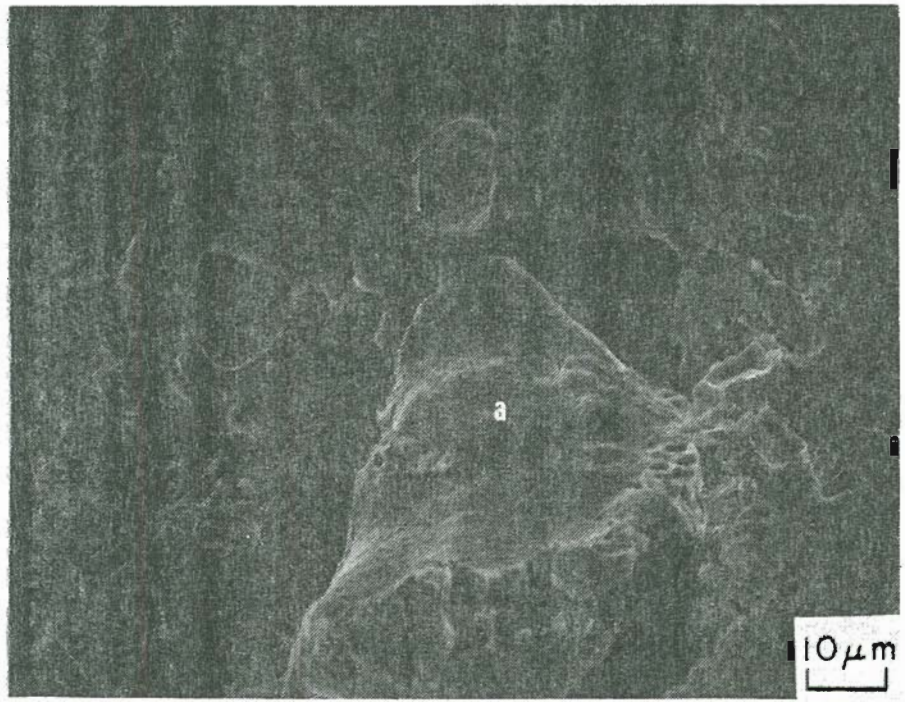

Fig.#90 Group IV-A, 2-B, A. -140F 1000X

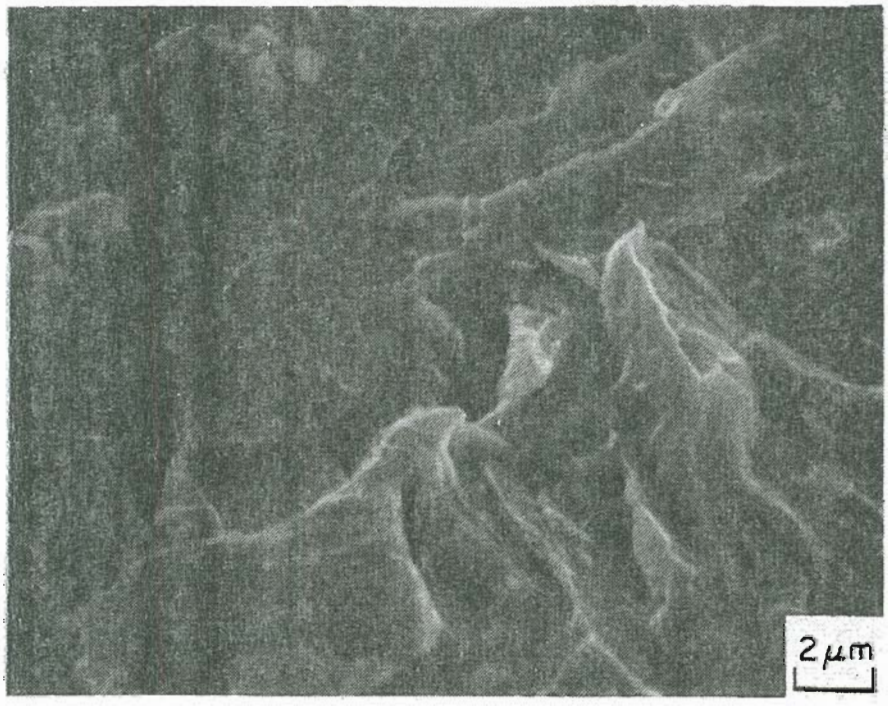

Fig.#91 Group IV-A, 2-A, B. -140F 5000X

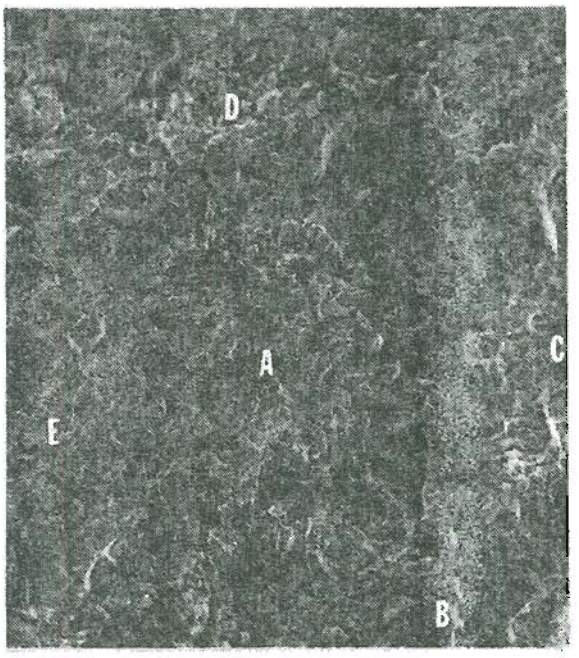

Group I

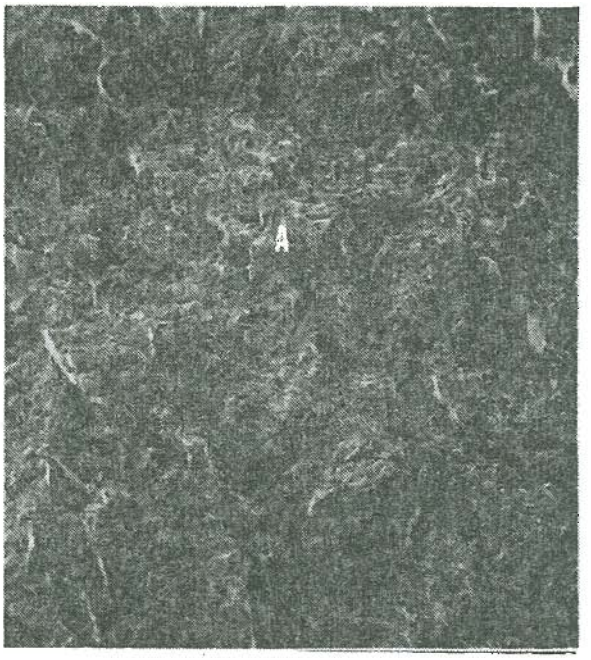

Group II

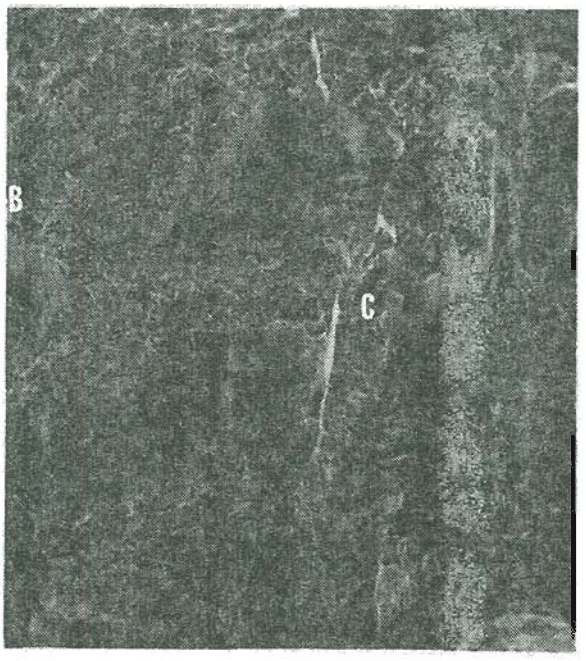

Group III

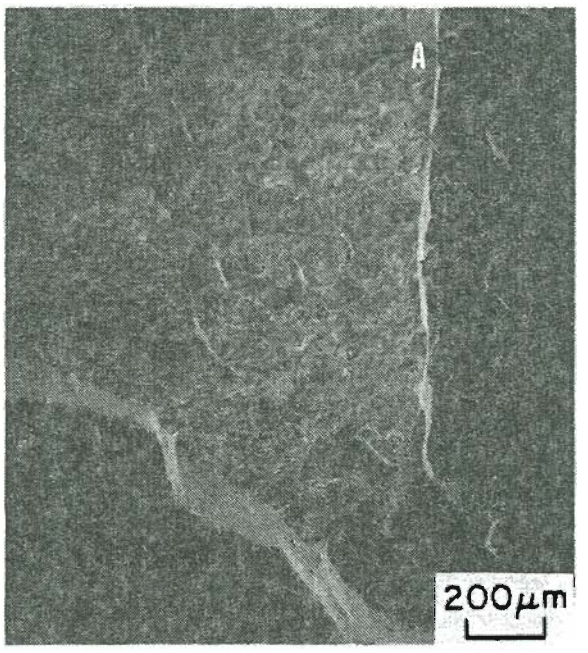

Group IV

Fig.#92 Increasing 'step fracture' mode with increasing Sb conte
50X -40F

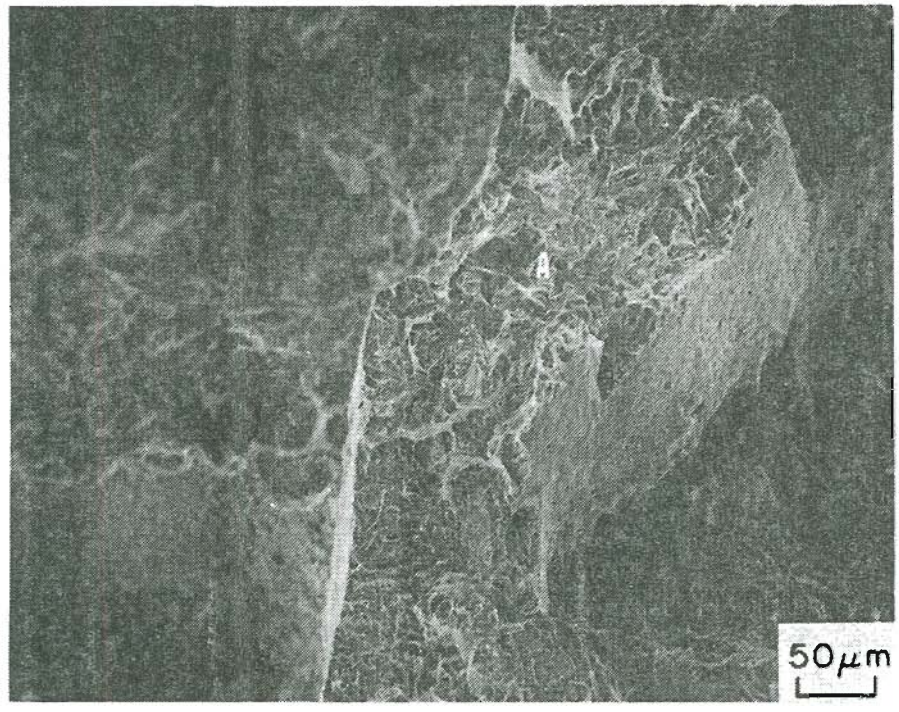

Fig.#93 'Step fracture' mode with intergranular fracture site at A. Group III, -40F. 200X

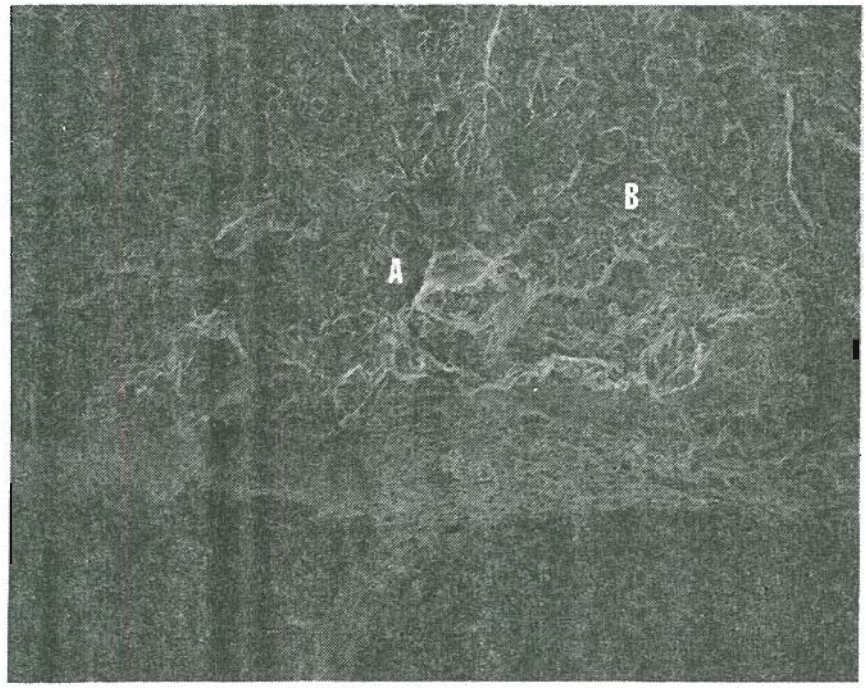

Fig.#94 'Step fracture' mode with large shear steps and intergranular fracture site at A. Group IV, -40F. 200X

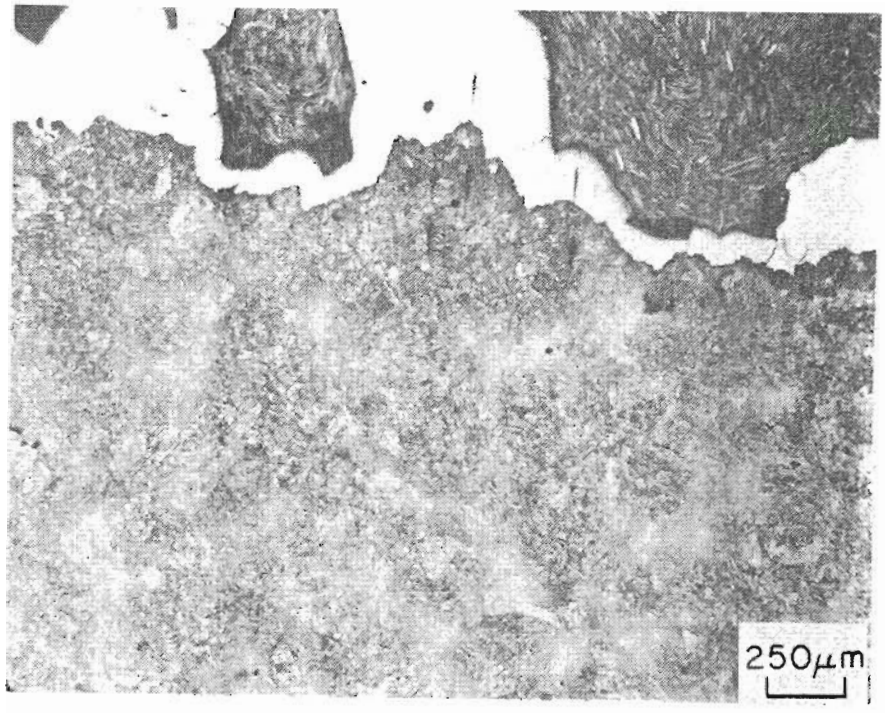

Vilella's 40X

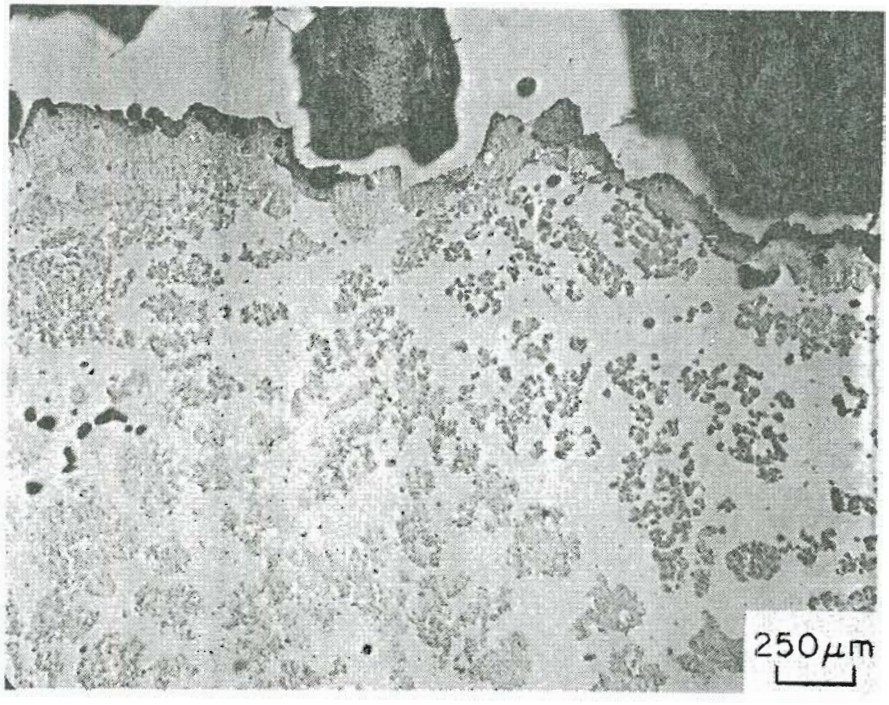

Group I, -40F.

Fig.#95 Cu deposit along fracture surface prevented correlation of fracture mode VS solidification pattern.

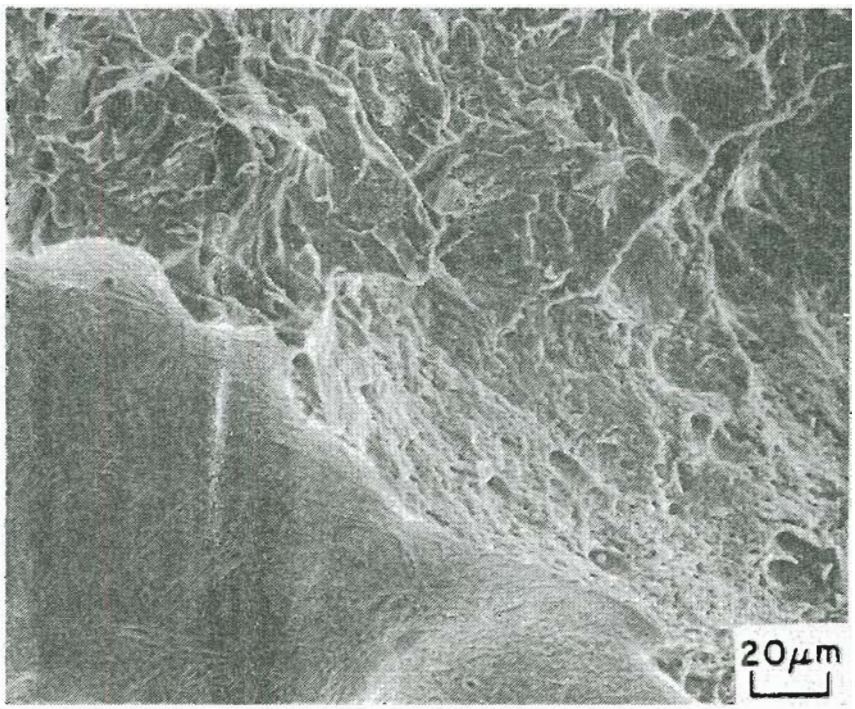

Fig.#96 Group I -40F 500X

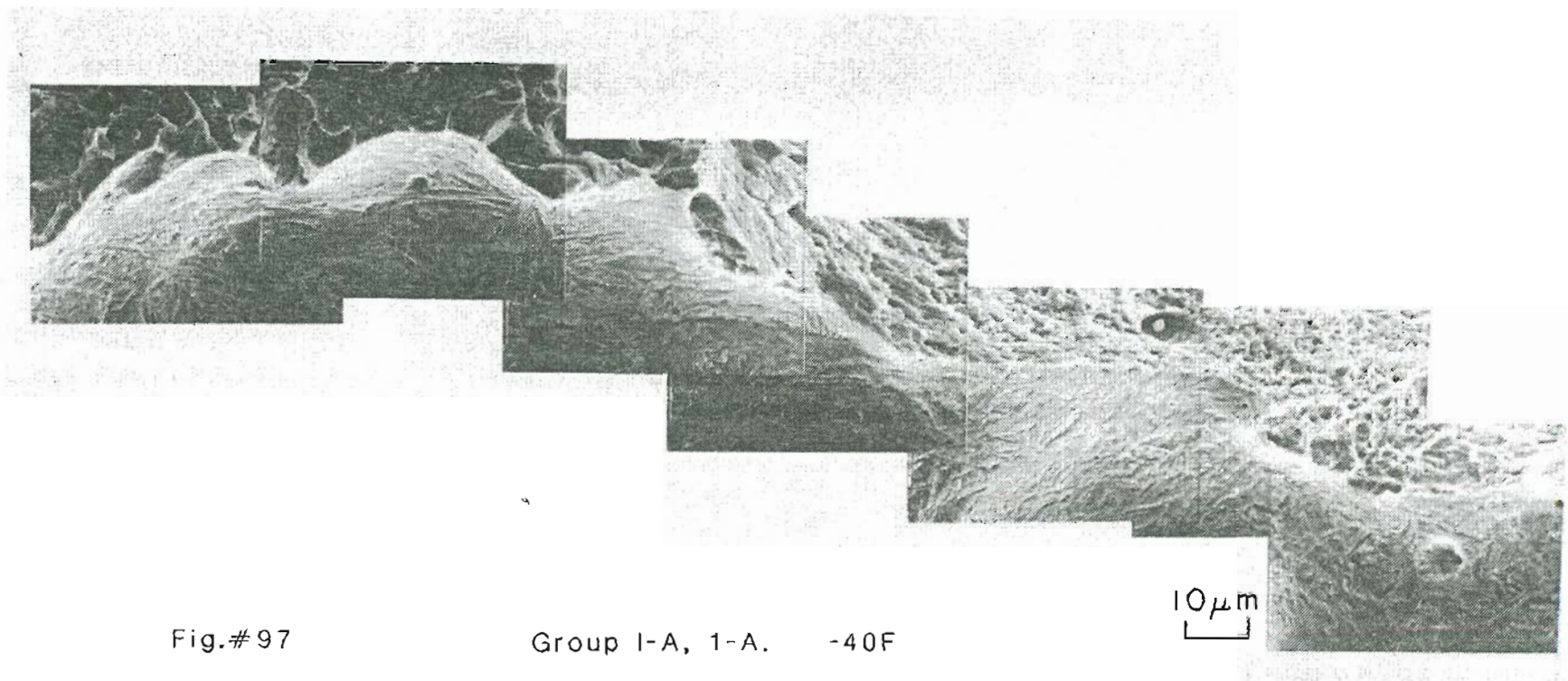

Fig.#97 Group I-A, 1-A. -40F

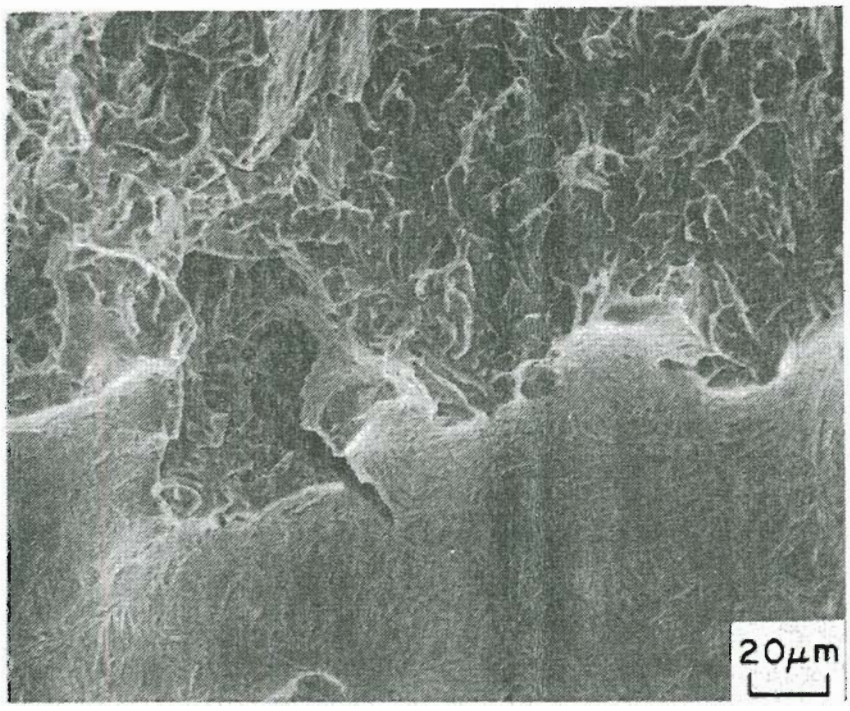

Fig.#98 Group II-B, 1-A. -40F 500X

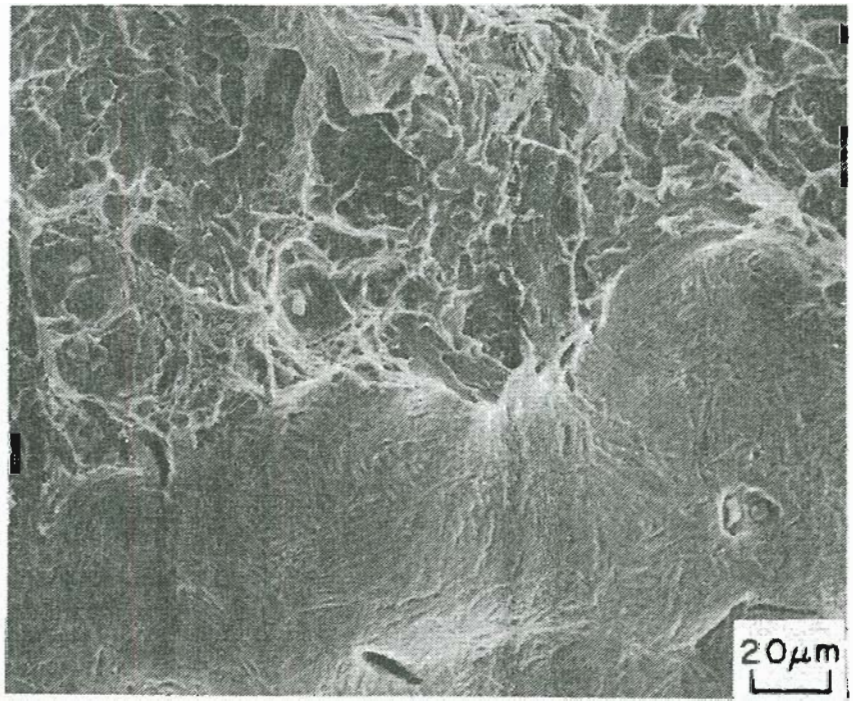

Fig.#99 Group II-B, 1-B. -40F 500X

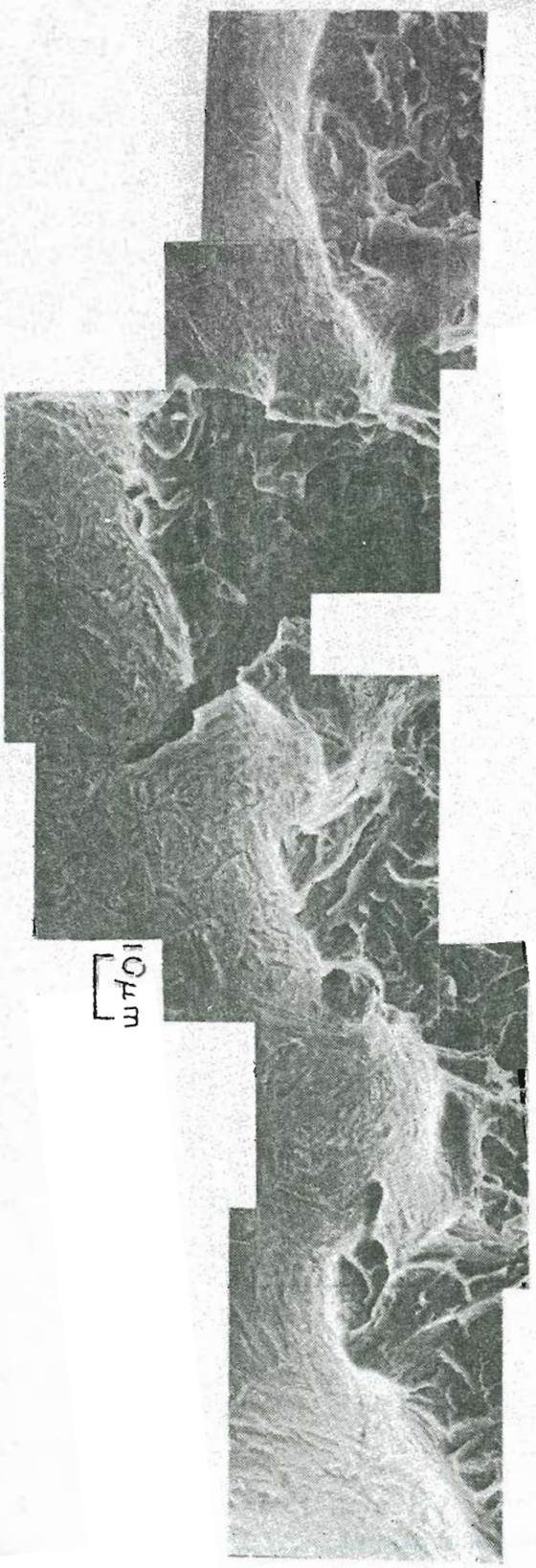

Fig.# 100 Group II-B, 1-A. -40F

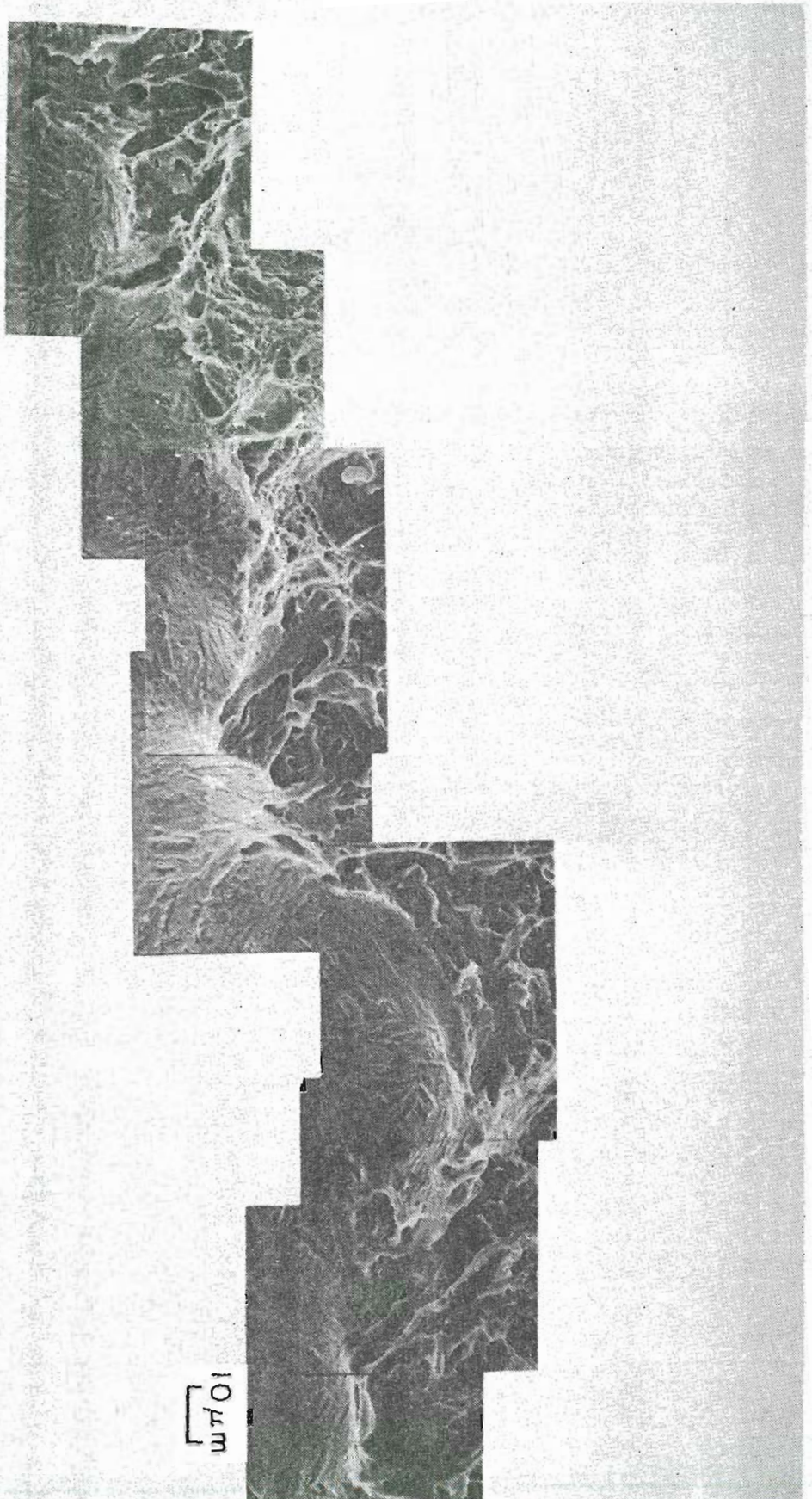

Fig. #101 Group II-B, 1-B. -40F

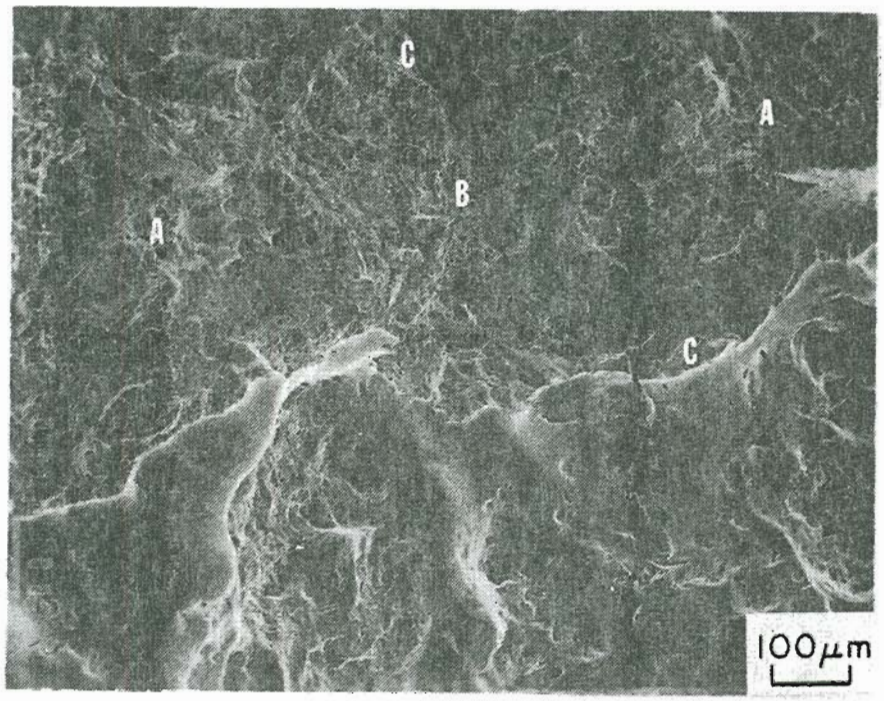

Fig.#102 Note ductile dimple zones at regions "A", cleavage zone at "B", with intergranular sites at "C". Group III-C, 2-A. -40F 100X

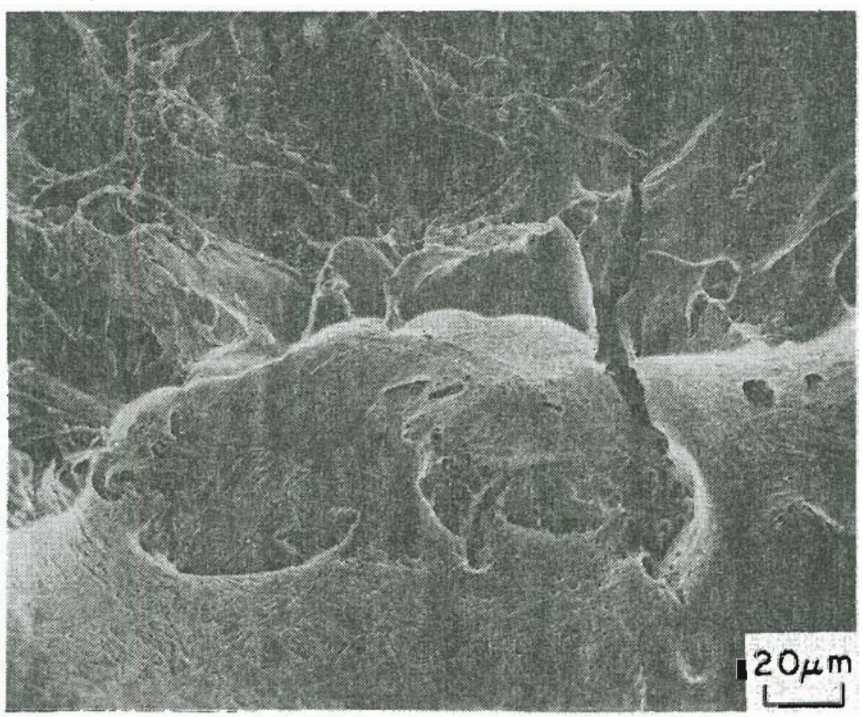

Fig.#103 Intergranular site at "C". Group III-C, 2-A. -40F 500X

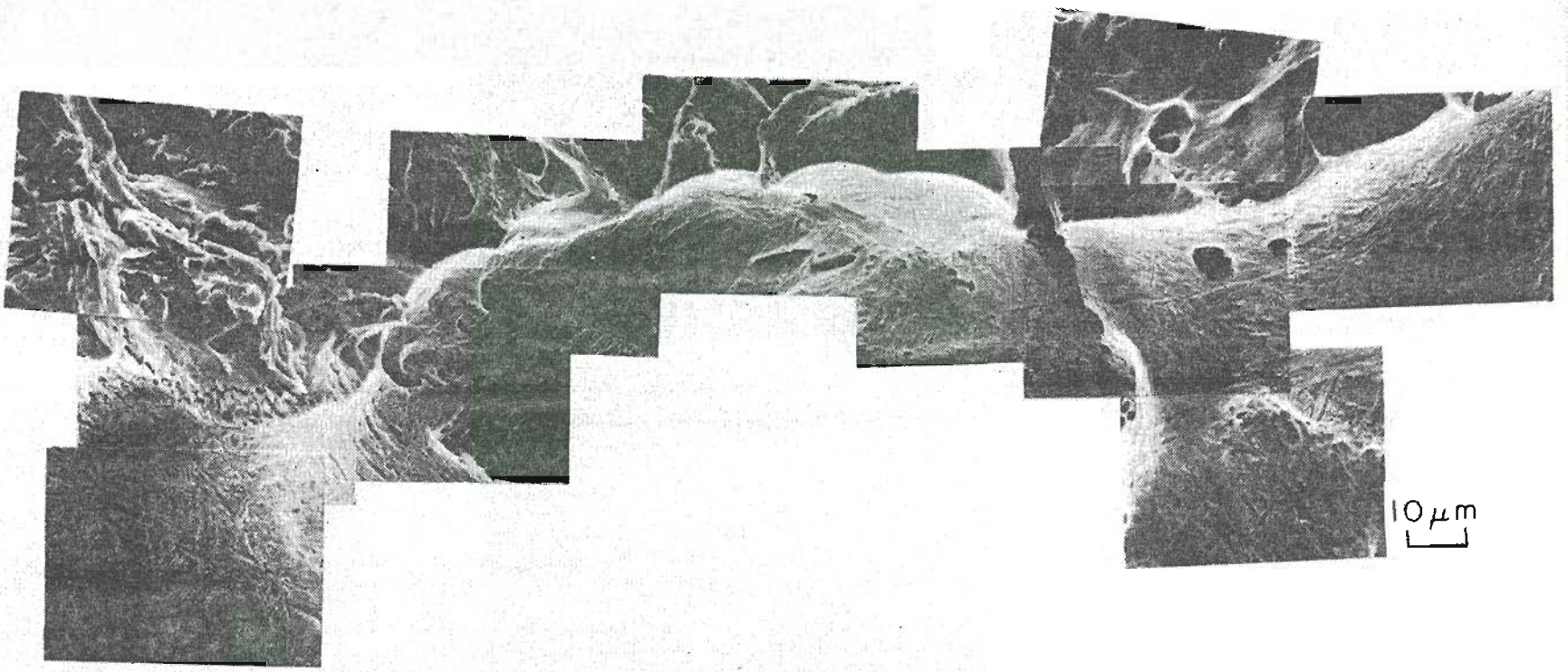

Group III-C, 2-A. -40F Intergranular fracture site "C".

Fig.# 104

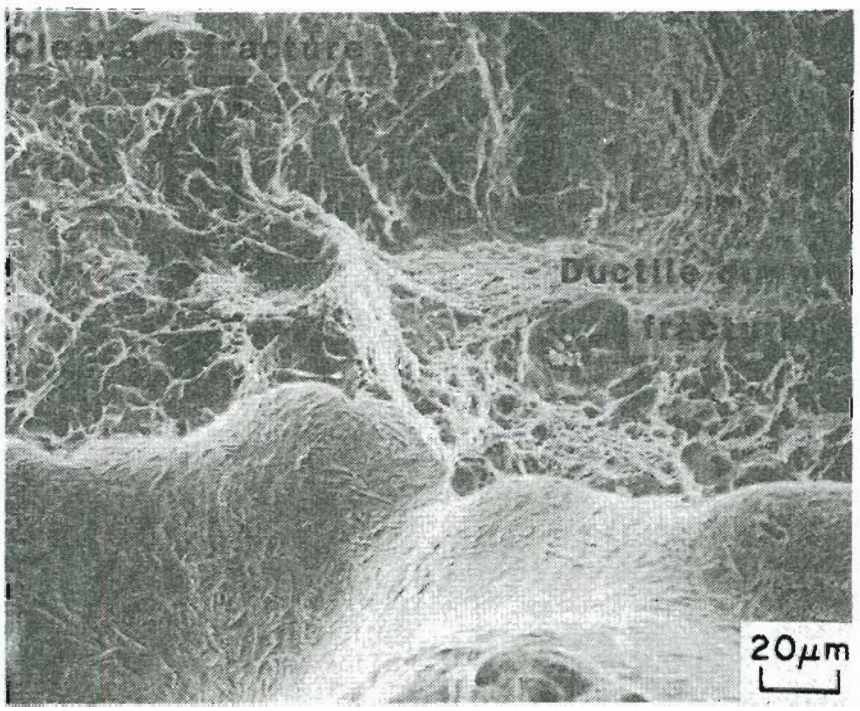

Fig.#105 Cleavage to ductile dimple transition.

Group III-2, B-b. -40F 500X

Fig.#106 Group III-2, B-b. -40F Same site as Fig.#105

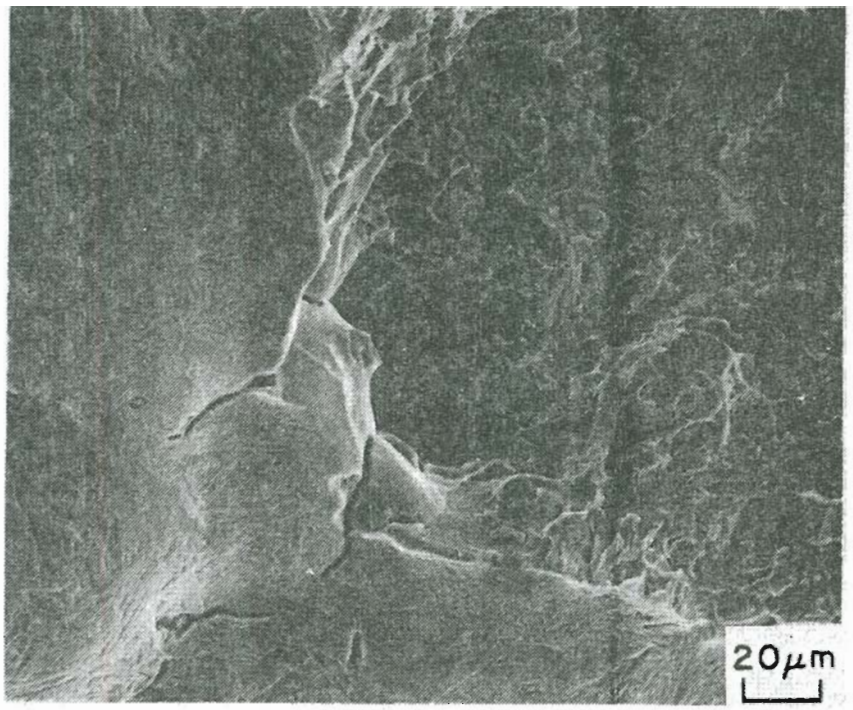

Fig.#107 Example of etch rate change in cleavage to intergranular fracture transition.
Group IV-2, C. -40F 500X

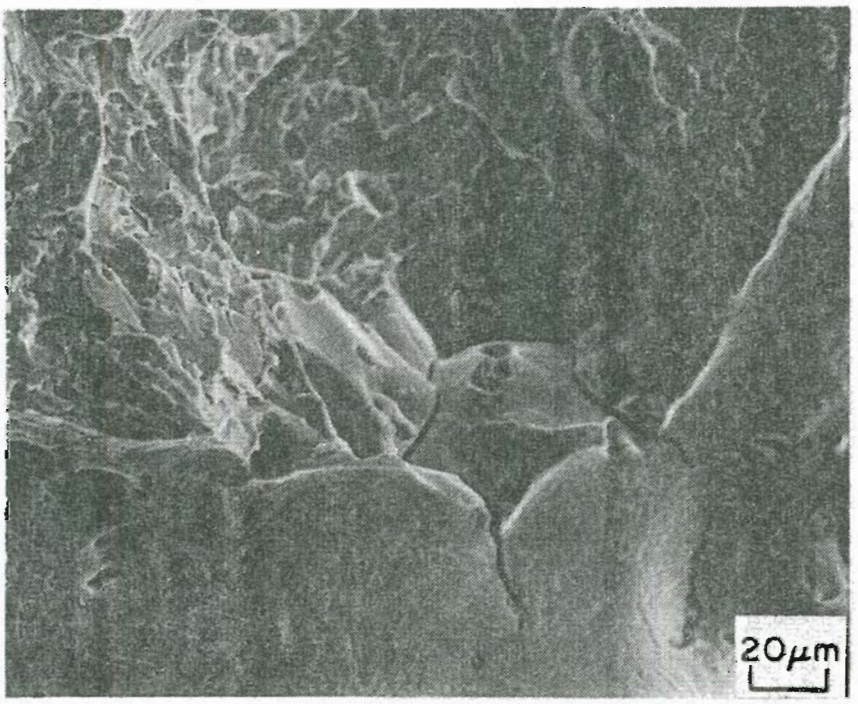

Fig.#108 Example of etch rate change in cleavage to intergranular fracture transition.
Group IV-2, E. -40F 500X

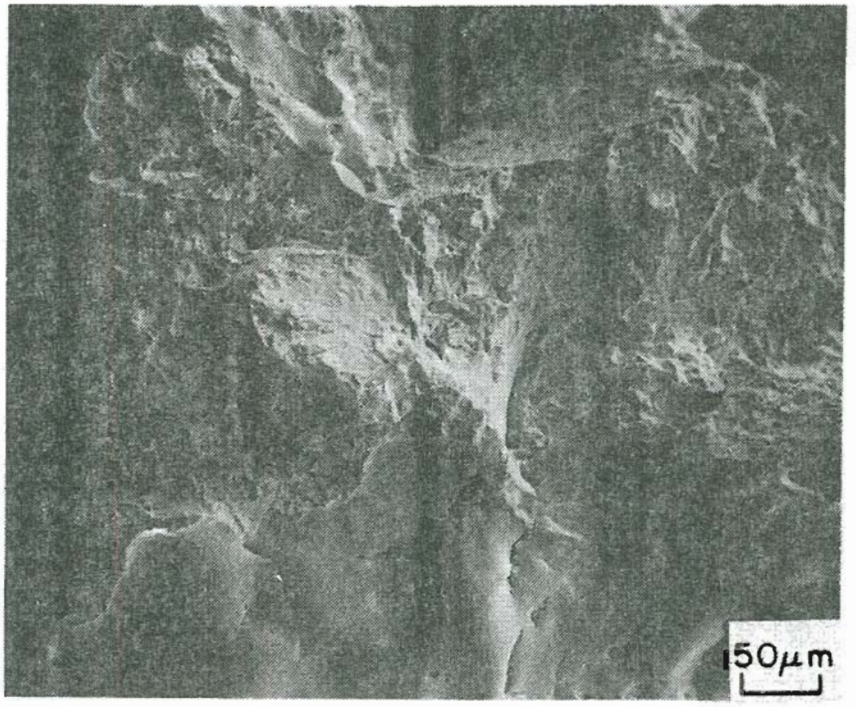

Fig.#109 Group IV-D, 4-B. -40F 200X

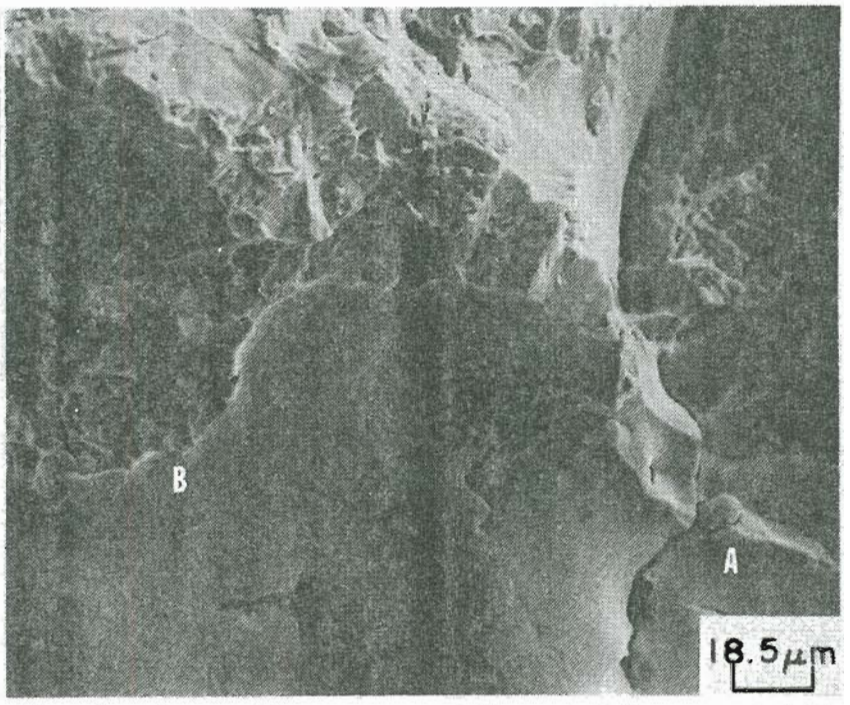

Fig.#110 Note areas "A" and "B". 540X
Group IV-D, 4-B. -40F

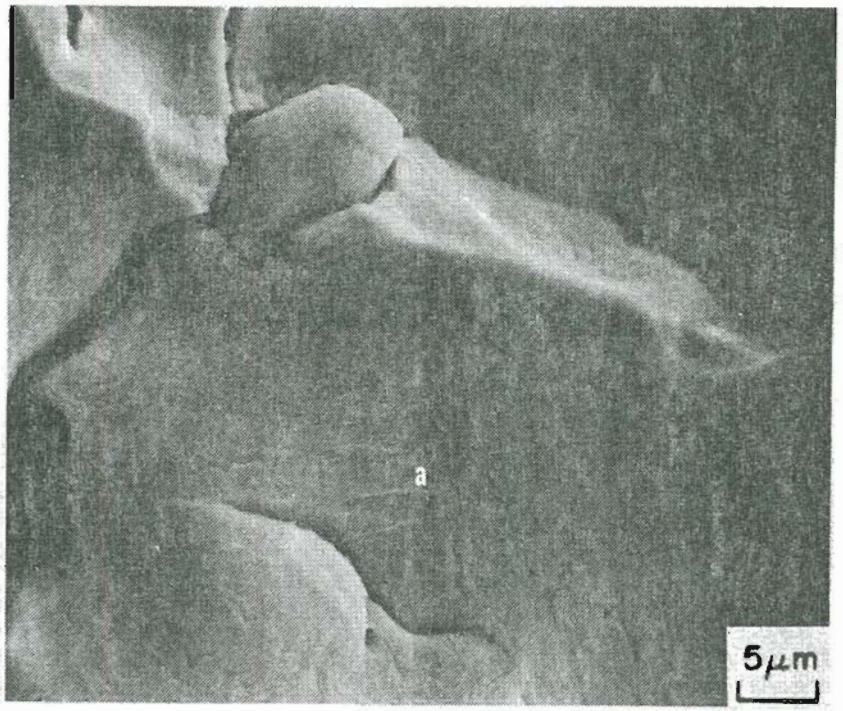

Fig.#111 Intergranular fracture site "A".
Group IV-D, 4-B, A. -40F 2000X

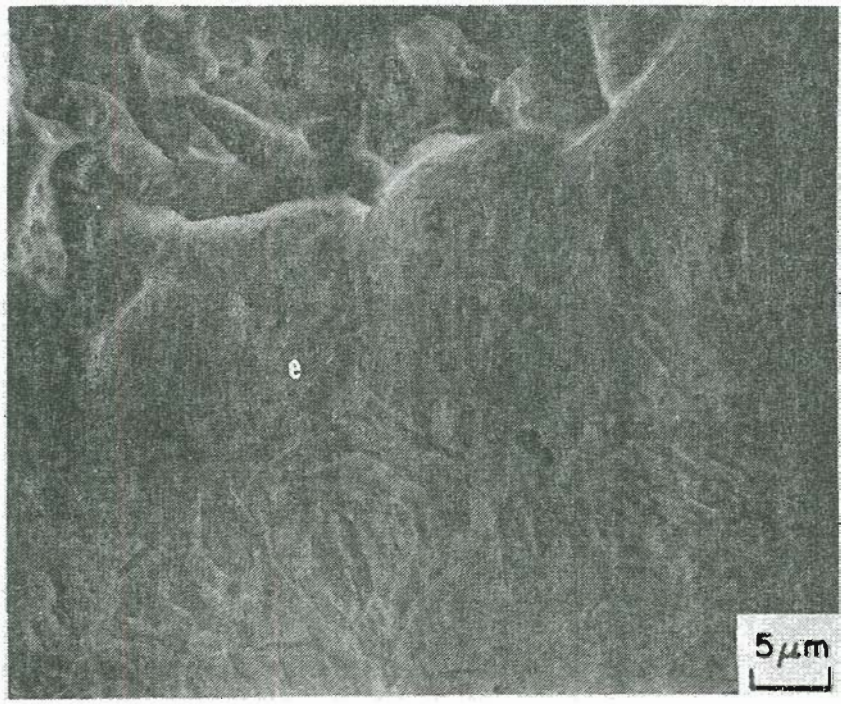

Fig.#112 Cleavage fracture site "B".
Group IV-D, 4-B, B. -40F 2000X

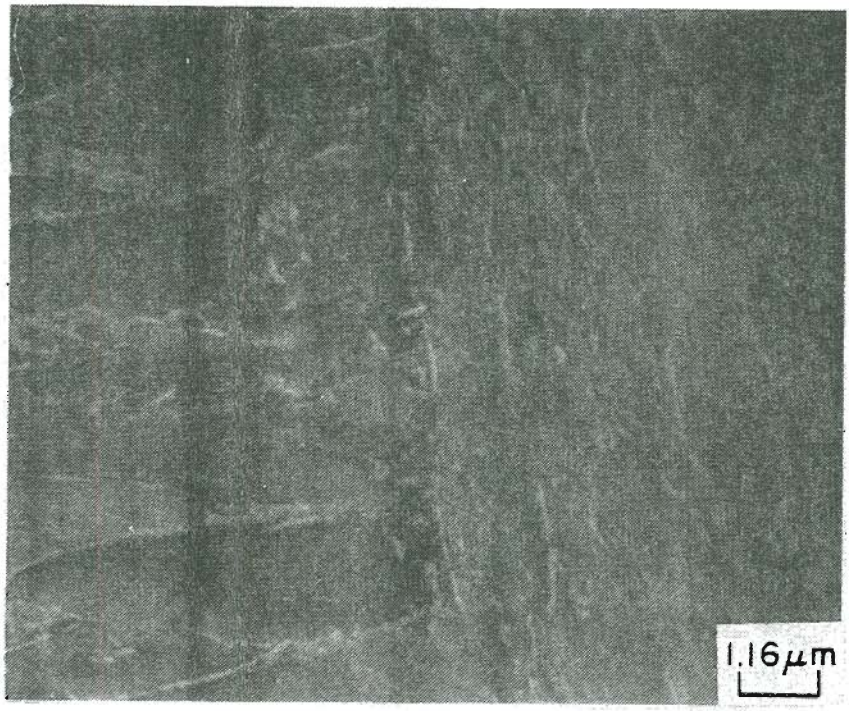

Fig.#113 Intergranular fracture site "A-a". 8600X
Compare to Fig.#114 Group IV-D, 4-B, A-a. -40F

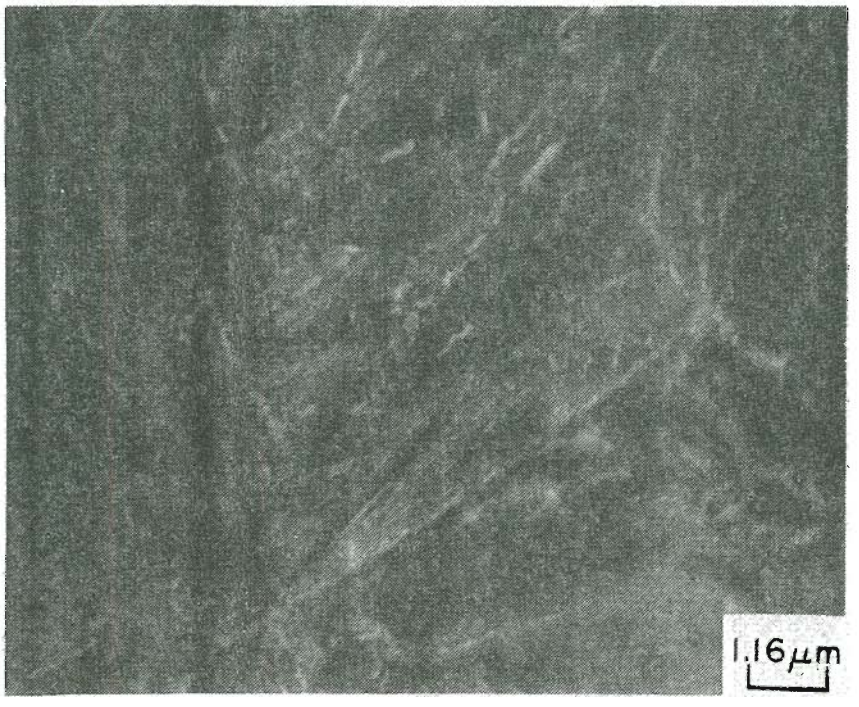

Fig.#114 Cleavage fracture site "B-e". 8600X
Note difference in carbide size and etch rate characterics between the two regions. Group IV-D, 4-B, B-e. -40F

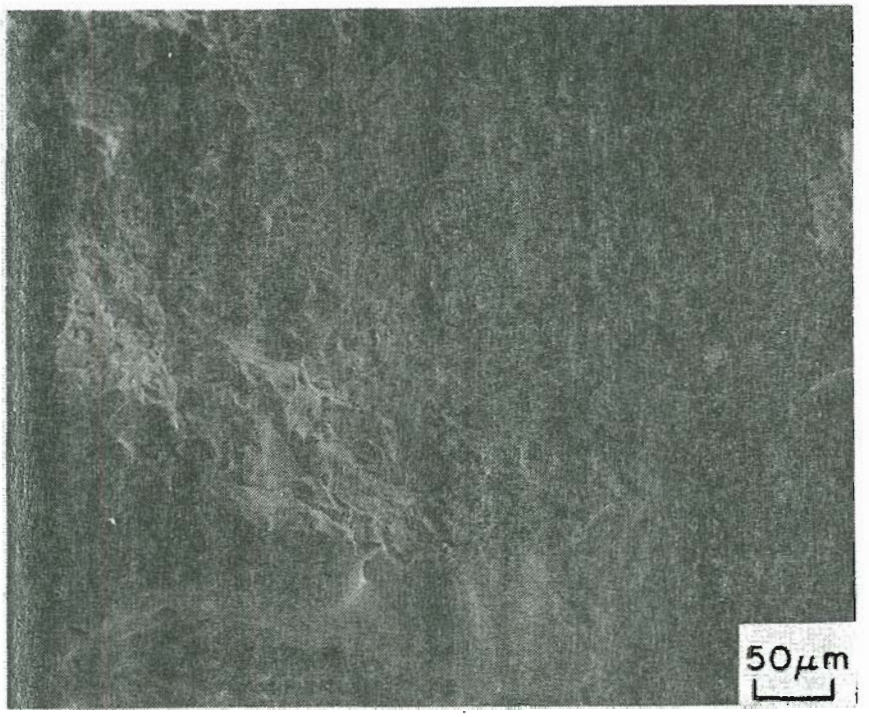

Fig.#115 Group IV-D, 4-A. -40F 200X

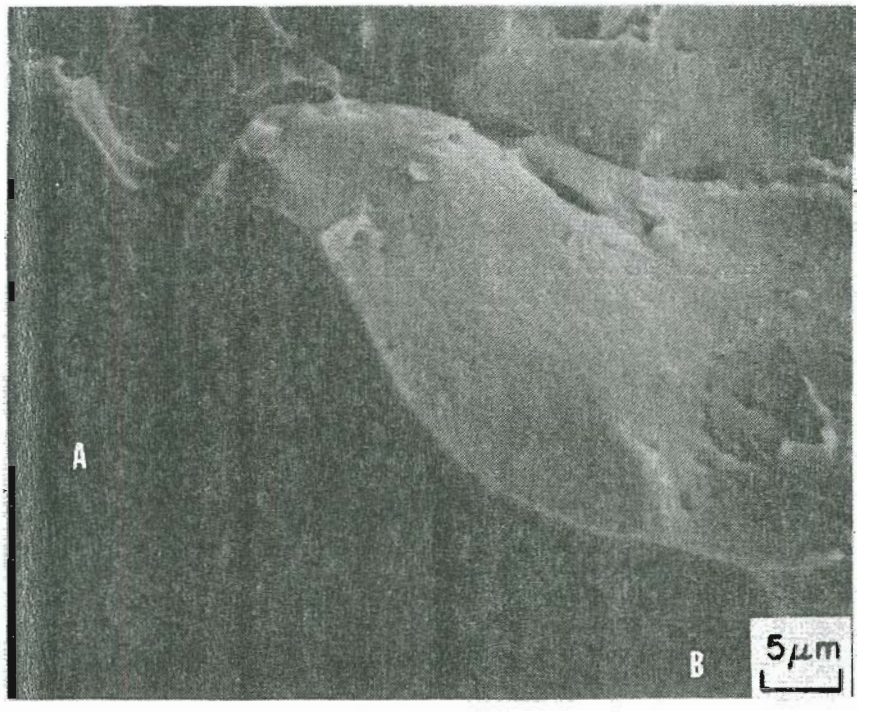

Fig.#116 Note areas "A" and "B". 2000X
Group IV-D, 4-A. -40F

Group IV-D, 4-A, A. -40F Cleavage fracture region. Compare to Fig.#118 Fig.#117

Group IV-D, 4-A, B. -40F Intergranular fracture region. Fig.#118

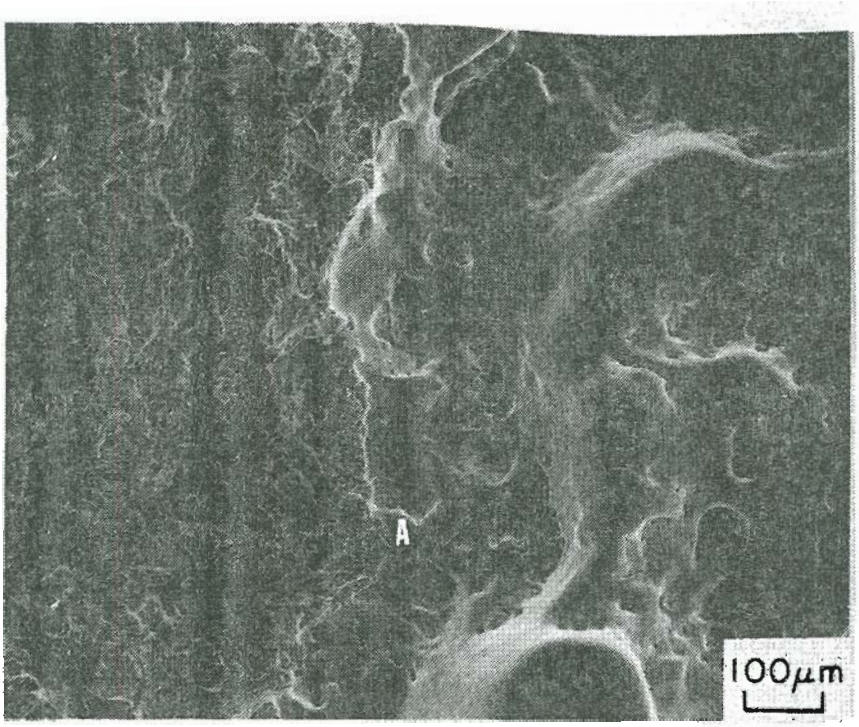

Fig.#119 Random intergranular fracture at region "A".
Group IV-D, 4-B. -40F 100X

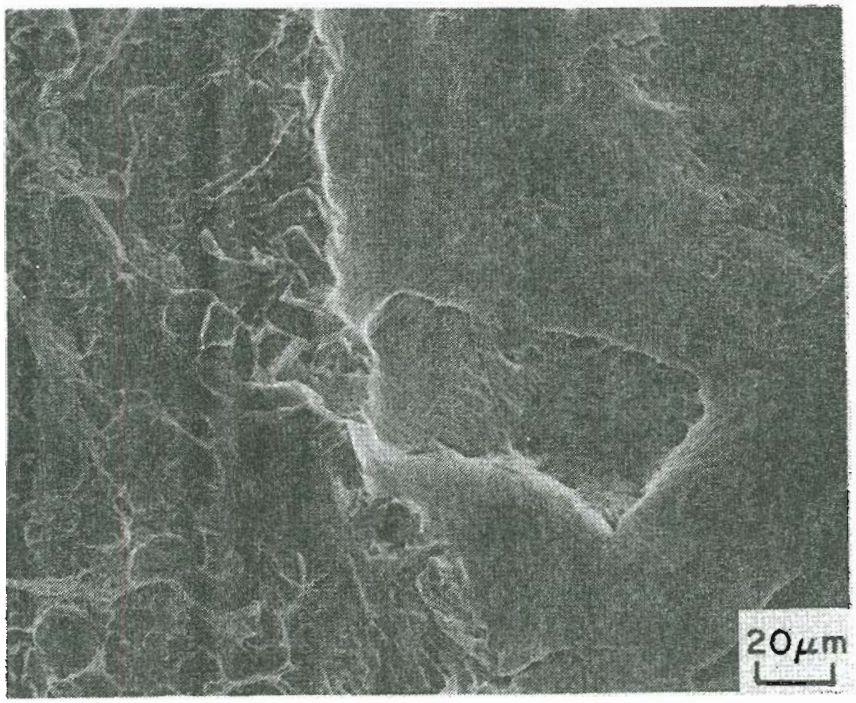

Fig.#120 Region "A". Random intergranular fracture.
Group IV-D, 4-B, A. -40F 500X

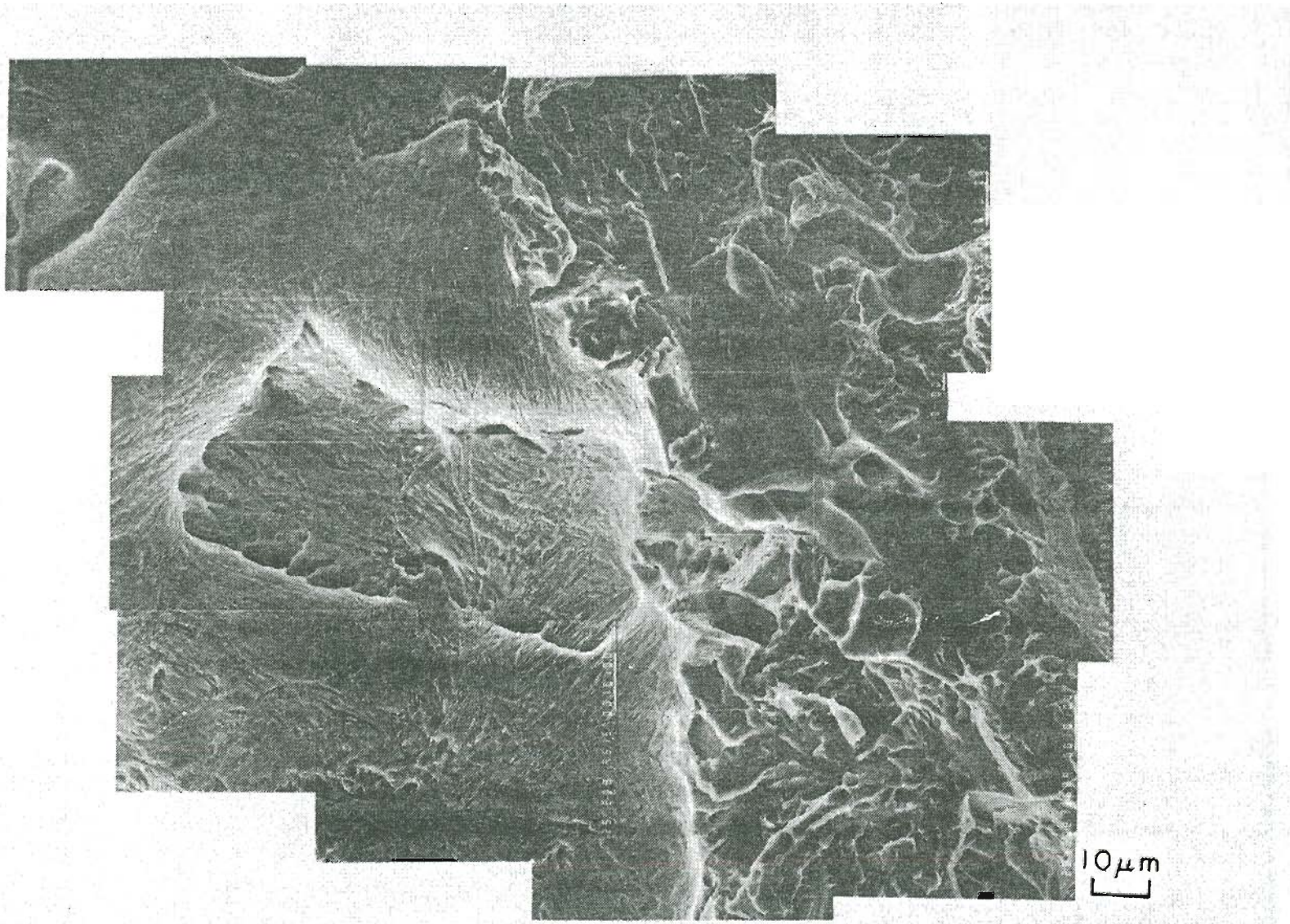

Group IV-D, 4-B, A. -40F Region "A". Random intergranular fracture. Fig.#121

Fig. 122.

Hypothetical Ternary Diagram with the Location of Fe-X Isopleth

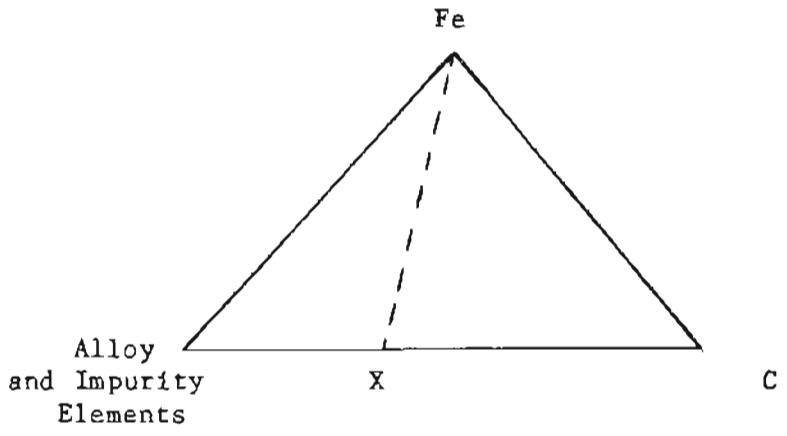

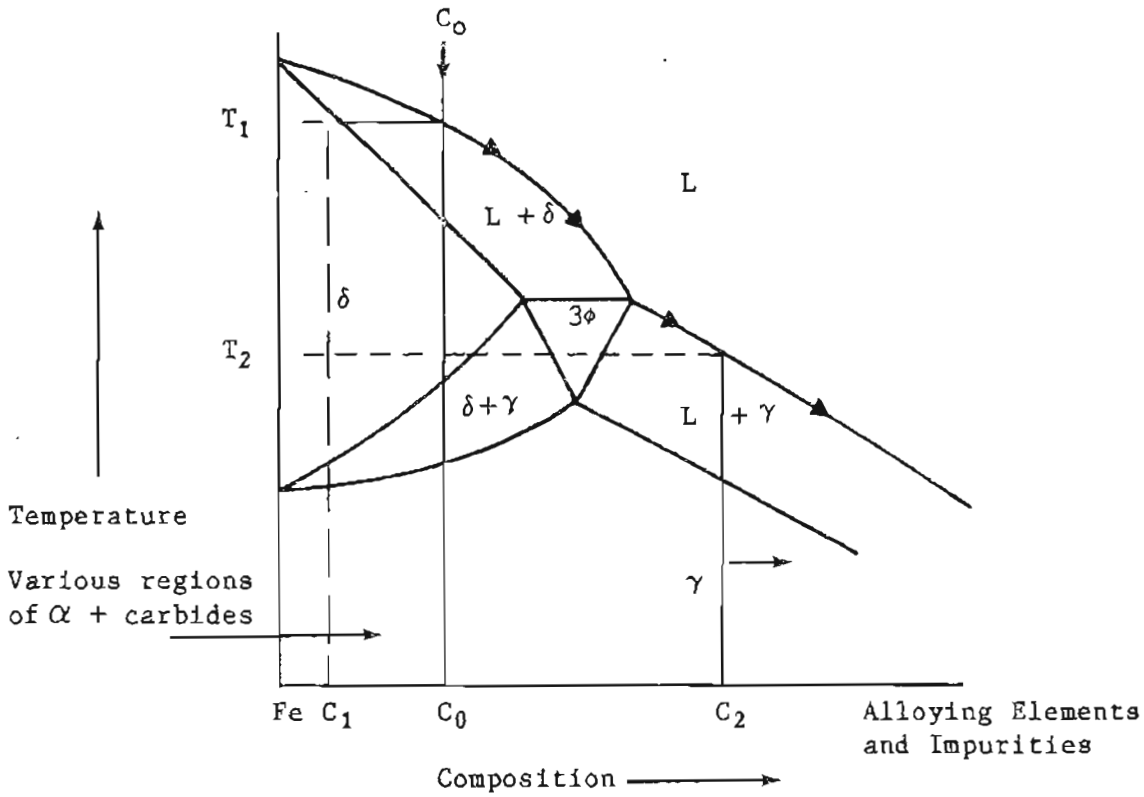

Assume Ternary Characteristics for this Multi-Component System

Fig. #123. Fe-X Isopleth shown in Fig. #122. Arrows indicate the composition of the Liquid as Non-Equilibrium Solidification Progresses

SECTION #X

APPENDIX #I

RAW DATA AND SAMPLE CALCULATIONS

TABLE #AI

RAW DATA

Sb CONCENTRATION OF AOD AND NON-AOD
PROCESSED LOW ALLOYS AS A FUNCTION OF TIME

		Week #1	Week #2	Week #3	Week #4	Week #5	Week #6
AOD	Concentration	.001 .0025 .0023	.0021 .0031 .0017	.0058 .0037	.0022 .0016	.0016 .0017 .0016	.002 .00176 .00152
	Mean	.00193	.0023	.00475	.0019	.001633	.00176
	Std. Deviation	.0008	.000721	.00148	.00042	.000057	.00024
	+ 1	.00274	.00302	.00623	.00232	.00169	.002
	- 1	.00111	.00157	.00326	.00147	.00157	.00152
NON-AOD	Concentration	.0034 .0014 .0014	.0018 .0019 .0023	.0046 .0034	.0022 .00056	.0024 .0015	.00185 .00081 .0018
	Mean	.00206	.0020	.0040	.00138	.00195	.00148
	Std. Deviation	.00115	.000264	.00084	.00115	.00063	.000586
	+ 1	.00322	.00226	.00484	.00253	.00258	.00207
	- 1	.00091	.00173	.00315	.00022	.00131	.00090

TABLE #AII

RAW DATA

COMPOSITIONAL VARIATIONS OF ELEMENTS IN STAINED AND UNSTAINED FERRITE
(Concentrations in Wt %)

	SF				USF			
Group #	Si	Cr	Ni	Mo	Si	Cr	Ni	Mo
	0.52	0.89	0.82	0.15	0.58	0.98	0.94	0.11
I	0.51	0.89	0.83	0.13	0.54	0.96	0.97	0.06
	0.95	0.90	0.86	0.30	0.82	0.92	0.87	0.08
	0.58	0.92	0.78	0.12	0.51	0.94	0.84	0.10
Mean	.64	0.90	0.822	0.175	0.612	0.95	0.930	0.087
SD	.208	0.141	0.0033	0.084	0.141	0.258	0.061	0.022
	0.76	0.87	0.81	0.18	0.68	0.94	0.96	0.15
	0.74	0.84	0.76	0.23	0.77	0.93	0.95	0.19
II	0.67	0.94	0.93	0.18	0.46	0.90	0.74	0.06
	0.70	0.94	0.86	0.19	0.51	0.92	0.82	0.10
	0.73	0.95	0.92	0.09	0.43	0.91	0.92	0.11
Mean	0.72	0.908	0.856	0.174	0.57	0.92	0.88	0.122
SS	0.035	0.049	0.072	0.051	0.147	0.015	0.096	0.049

TABLE #AII (cont'd)

Group #	SF				USF			
	Si	Cr	Ni	Mo	Si	Cr	Ni	Mo
III	0.68	0.91	0.81	0.24	0.54	0.91	0.68	0.14
	0.73	0.87	0.91	0.22	0.57	0.88	0.76	0.18
	0.57	0.93	0.74	0.15	0.66	0.90	0.74	----
	0.59	0.87	0.83	0.07	0.58	0.97	0.82	----
	0.57	0.96	0.80	----	0.70	0.89	0.86	----
Mean	0.628	0.908	0.818	0.17	0.61	0.91	0.772	0.16
SD	0.0729	0.038	0.061	0.077	0.067	0.035	0.070	0.028
IV	0.72	0.87	0.83	0.43	0.73	0.89	0.88	0.12
	0.79	0.88	0.66	0.11	0.69	0.85	0.92	0.10
	0.85	0.94	0.97	0.53	0.80	0.85	0.71	0.23
	0.66	0.91	0.75	0.33	0.82	0.86	0.75	0.15
	0.80	0.86	0.71	0.12	0.82	0.82	0.74	0.20
	0.63	0.81	0.83	0.27	0.64	0.85	0.80	0.12
	0.75	0.84	0.89	0.31	0.65	0.84	0.79	0.28
	0.70	0.89	0.77	0.22	0.72	0.86	0.78	0.24
	0.48	0.85	0.76	0.15	0.73	0.81	0.80	0.16
	1.00	0.90	0.84	0.13	0.59	0.84	0.73	0.14
	0.91	0.85	0.73	0.23	0.88	0.88	0.73	----
	0.89	0.92	0.88	----	0.70	0.89	0.75	----
	0.98	0.87	0.87	----	----	----	----	----
Mean	0.781	0.876	0.806	0.257	0.717	0.854	0.781	0.174
SD	0.147	0.035	0.085	0.135	0.074	0.025	0.063	0.060

TABLE #AIII

RAW DATA

COOLING RATE CALCULATIONS

$$\frac{d}{b} = (GR)^{-n} \qquad \text{(equation \#1)}$$

where: N = 1/3 - 1/2 for secondary dendrite spacings

= 1/2 for primary dendrite spacings

d = dendrite arm spacing (in m)

b = material constant

GR = average cooling rate during solidification (in °C/min.)

1) b was estimated from Flemings work [18] with commercial steels containing 0.1 - 0.9 wt % C

2) N was assumed to be 0.33.

From Flemings:

d	GR	$b = \frac{d}{GR^{-N}}$
70 μm	500° C/min	451
200 μm	20° C/min	491
400 μm	3° C/min	574

b assumed to be 500.

$$GR = \sqrt[N]{\frac{b}{d}}$$

where $b = 500$

$n = 0.33$

Group Number	Average d (in μm)	GR Average Cooling Rate (in °F/min)
I	200	61 (16° C/min)
II	200	61 (16° C/min)
III	200	61 (16° C/min)
IV	200	61 (16° C/min)

a) Calculated freezing temperature based on composition (provided by ESCO Corp.: 2748°F).

b) Superheat: 150°F (pouring temperature of 2900°F).

c) Cooling time from pouring test bars to final solidification: 2.5 min.

Estimated cooling rate:

$$\frac{2900°F - 2748°F}{2.5 \text{ min}} = 60.8 \text{ °F/min.}$$

TABLE #AIV

RAW DATA

MICROHARDNESS VARIATIONS OF SELECTED REGIONS VS Sb CONTENT

Knoop Hardness (50 gm load)

Sb Concentration	Region				
	SF	USF	RR	DA	IDA
0.003 Wt %	175 185 213	195 227 232		205 235 245	325 350 360 363
Mean	190.3	218		228.3	349.5
SD	± 20.52	± 20.07		± 20.8	± 17.25
0.007 Wt %	132 153 163 177 195	185 205 220 252 264		275 280 283 285	340 403 405 425 447
Mean	164	225.2		280.75	404.0
SD	± 23.85	± 32.69		± 4.34	± 39.96

TABLE #AIV (continued)

Sb Concentration		Region			
	SF	USF	RF	DA	IDA
0.012 Wt %	185 203 220 225	244 255 270 275		285 290 295 320 327	365 370 385 420 435 440 465
Mean	208.25	261.0		303.4	411.4
SD	± 18.3	± 14.16		± 18.84	± 38.48
0.016 Wt %	158 165 177 187 190 195 201 209	235 243 245 257 275	237 244 247 250 273	270 275 280 283 290	383 395 415 425 435 467
Mean	185.25	251	250.2	279.6	420
SD	± 17.53	± 15.55	± 13.62	± 7.63	± 29.92

TABLE #AV

THE SEGREGATION INDEX OF VARIOUS ELEMENTS VS Sb CONTENT
(Concentration values in Wt %)

Group #	Element	Mean Concentration		Mean Segregation Ratio
		DA	IDA	
I	Si	0.646	0.74	0.191
	Cr	0.866	0.956	0.094
	Ni	0.793	0.893	0.108
	Mo	0.100	0.150	0.333
II	Si	0.576	0.736	0.325
	Cr	0.900	1.066	0.173
	Ni	0.766	1.010	0.263
	Mo	0.120	0.263	0.430
III	Si	0.623	0.816	0.392
	Cr	0.900	1.156	0.268
	Ni	0.790	1.023	0.252
	Mo	0.290	0.393	0.310
IV	Si	0.810	1.003	0.392
	Cr	0.830	1.013	0.191
	Ni	0.720	1.026	0.331
	Mo	0.246	0.370	0.372

$$\text{Mean Segregation Ratio} = \frac{\text{IDA-DA}}{\text{Mean Bulk Composition}} \qquad \text{(equation \#5)}$$

TABLE #AVI

RAW DATA

CVN IMPACT ENERGY CALCULATIONS

Test Temp. °F	Group #1			Group #2			Group #3			Group #4		
	ft-lb	Ave	Z	ft-lb	Ave	Z	ft-lb	Ave	Z	ft-lb	Ave	Z
-140	6,9	7.5	-0.88	5,5	5	-0.74	9,12	10.5	-0.87	8,12	10	-0.82
-100	10,12	11	-0.68	12,13	12.5	-0.51	12,13	12.5	-0.71	14,14	14	-0.59
- 60	18,21	19.5	-0.29	25,24	27	-0.18	21,22	21.5	-0.41	25,26	25.5	-0.19
- 40	34,44	39	-0.03	35,44	39.5	0	26,29	27.5	-0.21	28,34	31	0.04
- 20	32,45	38.5	0.23	41,42	41.5	0.188	32,39	35.5	0	35,39	37	0.28
20	45,47	46	0.64	43,47	45	0.51	58,59	58.5	0.41	44,47	45.5	0.65
60	59,62	60.5	0.86	52,59	55.5	0.74	53,53	53	0.71	52,53	52.5	0.85
100	51,58	54.5	0.95	53,54	53.5	0.87	52,54	53	0.87	48,54	51	0.94
140	60,61	60.5	0.98	58,60	59	0.93	56,58	57	0.94	48,51	49.5	0.97
180	57,61	59	0.99	55,58	56.5	0.97	58,61	59.5	0.97	50,52	51	0.99
212	58,59	58.5	0.99	52,54	53	0.98	56,57	56.5	0.98	47,50	48.5	0.99

T = Test Temp.
T_o = -37.5
C = 74.5

T = Test Temp.
T_o = -40.0
C = 105

T = Test Temp.
T_o = -20
C = 90

T = Test Temp.
T_o = -44
C = 81

$$Z = \tanh\left[\frac{T - T_o}{C}\right] \qquad \text{(equation 2)}$$

TABLE #AVII

RAW DATA

EFFECTS OF VARIOUS HEAT TREATMENTS
ON CVN IMPACT PROPERTIES VS Sb CONTENT
(Impact Energy Values in Ft-Lbs)

Group #		Heat Treatment A	Bx	By
I		34	44	37
		44	45	41
			41	43
			45	42
			45	43
			40	49
	Mean	39.0	43.33	40.83
	SD	7.07	2.25	2.40
IV		28	42	40
		34	40	45
			40	36
			45	47
			46	
	Mean	31	42.6	42.0
	SD	4.24	2.79	4.96

TABLE #AVIII

RAW DATA

BRINELL HARDNESS DATA VS Sb
CONTENT; FULLY HEAT TREATED CONDITION

Group #	Brinell Hardness (3000 Kg load)	Mean	Std Deviation
I	278, 278, 278, 278	278	0
II	293, 293, 293, 293	293	0
III	277, 293, 293, 285	287	7.65
III	285, 285, 302, 293	291.25	8.09

SECTION XI

APPENDIX II

MECHANISMS CONTROLLING CARBIDE SIZE

MECHANISMS CONTROLLING CARBIDE SIZE

Diffusion controlled particle coarsening is a function of the following parameters:

1) The change in free energy due to a decrease in precipitate matrix interfacial area is the driving force of the coarsening process.
2) The cube root of the aging time is directly proportional to carbide size.
3) The diffusion of solute atoms in the matrix is directly proportional to the activation energy of coarsening.

The size of a particle with time for diffusion controlled coarsening can be expressed as:

$$r^3 - r_o^3 = \left(\frac{8\gamma D C_e V_m^2}{9 RT}\right) t = K^* t$$

(equation #3A)

where: r is the mean radius of a particle at any point in time.

r_o is the mean radius of a particle at the beginning of coarsening.

γ is the interfacial free energy of the ferritic matrix.

C_e is the concentration of solute atoms in equilibrium with a particle of infinite radius.

V_m is the molar volume of cementite

T is the absolute temperature

K* is the coarsening rate constant

t is time

The above equation can be rearranged to:

$$K^* = \left(\frac{8 \gamma D_{eff} C_e V_m^2}{9 RT} \right) \qquad \text{(equation \#3B)}$$

where D_{eff} is the effective diffusion coefficient

$$D_{eff} = \left(\frac{C_{Fe} V_{Fe}^2}{C_c V_i^2} \right) D_{Fe} \qquad \text{(equation \#3C)}$$

where C_{Fe} is the concentration of iron in ferrite.

V_{FE} is the atomic volume of iron in ferrite.

C_c is the concentration of carbon in ferrite.

V_c is the difference in volume between one molecule of Fe_3C and three atoms of iron in ferrite.

D_{Fe} is the self diffusion coefficient of iron in α iron.

Combining the two equations gives:

$$K^* = \left(\frac{8 \gamma V_m^2 C_c C_{Fe} V_{Fe}^2}{9 RT C_c V_c^2} \right) D_{Fe}$$

(equation #3D)

Impurity concentrations influence the diffusion coefficient. Sb has been noted to decrease the diffusion coefficient in α iron.[25] From the above equation it can be seen that among other variables, the C content in the ferrite and the diffusion coefficient control carbide size.

XII VITAE

Biographical Note

The author was born May 19, 1949 in Portland, Oregon. He attended grammar schools in Eugene, Coos Bay and Coquille, Oregon and graduated from Coquille High School in 1967. He then entered Oregon State University where he received his Bachelor of Science degree in June of 1972.

In March of 1973 the author began work at Northwest Testing Laboratory in Portland, Oregon. In June of 1974, the author accepted a position at ESCO Corporation in Portland, Oregon. While still employed at ESCO Corporation, the author began study at the Oregon Graduate Center in Beaverton, Oregon. In October of 1983, the author accepted a position at Precision Castparts Corporation in Portland, Oregon.